

# **TiCN hard coatings: tribological performance and deposition process analysis**



**Marisa Rebelo de Figueiredo**

**Leoben, March 2011**

being a thesis in partial fulfilment of the requirements for the degree of a  
**Doctor of Montanistic Sciences (Dr. mont.)**  
at the University of Leoben



This thesis was supported by the Christian Doppler Research Association in the framework of the Christian Doppler Laboratory for Advanced Hard Coatings at the Department of Physical Metallurgy and Materials Testing at the University of Leoben, Austria, in cooperation with Plansee Composite Materials GmbH in Lechbruck, Germany, and OC Oerlikon Balzers AG in Balzers, Principality of Liechtenstein.

### **Affidavit**

I declare in lieu of oath, that I wrote this thesis and performed the associated research myself, using only literature cited in this volume.

Leoben, March 2011

A handwritten signature in blue ink on a light yellow background. The signature reads "Marisa Rebelo de Figueiredo" in a cursive script.



To my family



# Acknowledgement

I would like to start by thanking Christian Mitterer for giving me the chance to work in the thin films world, despite my academic background. I can never thank you enough!

I also would like to show my gratitude to Christian Weiß for accepting to work in this cooperation between the two Departments and for his support during the thesis.

Reinhard Kaindl from the Institute of Mineralogy and Petrography at the University of Innsbruck, Christopher Muratore and Andrey Voevodin from the Wright-Patterson Air Force Base (Ohio, USA), Kathryn Wahl from the Naval Research Laboratory (Washington, D.C., USA) and Richard Chromik from the McGill University (Montreal, Canada), were essential for the success of this thesis. Thanks for sharing your knowledge with me!

To our project partners Plansee and Oerlikon Balzers, in particular to Peter Polcik, Michael O'Sullivan and Conrad Polzer as well as Markus Lechthaler and Helmut Rudigier, I am very grateful for your support.

Jörg Neidhardt, thanks for your patience and guidance! You have taught me a lot.

A special thanks to my colleagues and friends, Claudia Walter, Jörg Paulitsch, David Holec, Martin Pfeiler, Anna Hofer, Nazanin Fateh and Gert Gassner! Muito obrigada pelo vosso apoio.

I would like to show my gratefulness to all the people that were part of the thin films group from 2005 until today. In one way or another you have all helped me through this learning process. A special thanks goes to Christian Tritremmel, Viktoria Edlmayr, Hilde Stopar and Regina Kranz.

I want to dedicate this work to my family! To my parents Maria de Lourdes and José Luis, my sister Daniela and my brother-in-law Alexandre, and my niece Madalena that unfortunately I do not see as often as I would like to. But also to my German family that accepted me with open arms 10 years ago. Thanks for your love and support!

O agradecimento mais importante é dirigido ao meu marido Robert que me conseguiu motivar para não desistir nos momentos críticos. Não tenho palavras ... Obrigada pela tua perseverança e amor.

Obrigada a todos!





A neutron walks into a bar and asks, "How much for a drink?"  
The bartender says, "For you? No charge."  
(The Big Bang Theory)



# Contents

<b>1</b>	<b>Introduction</b>	<b>3</b>
1.1	System: why TiCN? . . . . .	3
1.2	Vapor deposition techniques . . . . .	4
1.2.1	Magnetron sputtering . . . . .	5
1.2.2	Cathodic arc evaporation . . . . .	6
1.2.3	Thin film growth . . . . .	7
1.3	Mass and energy balance of deposition processes . . . . .	9
1.4	Tribology . . . . .	10
1.4.1	Friction . . . . .	10
1.4.2	Wear . . . . .	10
1.4.3	Lubrication . . . . .	12
1.5	Coating characterization . . . . .	13
1.5.1	Raman spectroscopy . . . . .	13
1.5.2	In situ tribometry . . . . .	14
<b>2</b>	<b>Summary</b>	<b>21</b>
<b>3</b>	<b>Publications</b>	<b>23</b>
3.1	List of included publications . . . . .	23
3.2	List of related publications . . . . .	23
3.3	My contribution to included publications . . . . .	24
	<b>Publication I</b>	<b>25</b>
	<b>Publication II</b>	<b>43</b>
	<b>Publication III</b>	<b>59</b>
	<b>Publication IV</b>	<b>71</b>



# 1 Introduction

## 1.1 System: why TiCN?

The development of hard coatings a few decades ago was motivated by the need of protecting engineering parts involved in tribological contacts that range from cutting tools to spectacle frames and watch cases. With the deposition of a hard coating on their surface, the lifetime and decorative appearance of such parts could be enhanced significantly and the benefits outweighed the additional production costs. Nowadays, the main driving force for further developments, in particular in the field of cutting applications, is the improvement of cutting performance, i.e. higher cutting speed and longer lifetime.

The coatings used for improving the wear resistance are mainly transition metal carbides, nitrides, and carbonitrides as they have attracted large technological interest due to their special properties. These properties comprise high hardness ( $H$ ) and Young's modulus ( $E$ ) which are among the key features in protecting the softer substrate material. Examples include the widely used TiAlN and CrAlN, which present values of  $H > 35$  GPa and  $E > 350$  GPa [1, 2]. Even higher hardness values could be obtained within the class of the so-called superhard coatings like nanocomposite Ti-B-N coatings, showing values of  $H \sim 50$  GPa and  $E \sim 500$  GPa [3]. Another property is the high melting point characteristic of refractory nitrides and carbides like TiN and TiC, with temperature values of 2950 °C and 3067 °C, respectively [4]. A high thermal stability is also necessary since many of the applied coatings are metastable, e.g. the already mentioned Ti-B-N coatings [5]. Elevated temperatures can be present in the tribological contact of many cutting applications. Since the surrounding atmosphere in such applications normally contains oxygen, a high oxidation resistance of the used coating material is of high importance as well. Coatings that can fulfill this demand are, e.g., (Ti,Al)N [6] and nanocomposite TiN-Si<sub>3</sub>N<sub>4</sub> coatings [7]. Other aggressive environments demand a high corrosion resistance. TiC<sub>1-x</sub>N<sub>x</sub> coatings have been found to be able to withstand H<sub>3</sub>PO<sub>4</sub> and sea water [8].

However, in the last years, the increasing awareness about the use of environmental hazardous lubricants led to the implementation of restrictive regulations concerning their use and, therefore, created new challenges for coating and lubrication developers. The present trend is the minimization of lubricant use giving dry sliding the main role in tribological contacts. As a consequence, the improvement of coatings presenting self-lubricant properties was intensified in the last years. Examples of coatings exhibiting these properties at low and moderate temperatures are diamond-like carbon (DLC) based coatings, MoS<sub>2</sub>, TiC<sub>1-x</sub>N<sub>x</sub> and most recently CN<sub>x</sub> coatings, whereas boron carbide (B<sub>4</sub>C) can also be used at high temperatures [9].

Ti(C,N) coatings, which were studied within this work, have been used by the industry since the 1980's. The TiC<sub>1-x</sub>N<sub>x</sub> coatings can be produced in a rather broad composition range, where  $x$  ranges from 0 to 1. The synthesized TiC<sub>1-x</sub>N<sub>x</sub> is a solid solution of TiN and

TiC, and has a face-centered cubic structure. The commonly good adhesion and toughness of TiN compensates for the brittleness of TiC, while the latter provides for hardness.  $\text{TiC}_{1-x}\text{N}_x$  coatings can exhibit high hardness values up to  $\sim 40$  GPa, depending on the nitrogen to carbon ratio. Another feature of this system, and maybe one of the most important properties, is the good tribological performance in dry sliding with low friction at room temperature and ambient atmosphere [10–15].

The  $\text{TiC}_{1-x}\text{N}_x$  coatings are mostly synthesized using physical vapor deposition techniques, namely magnetron sputtering [12, 14], reactive arc evaporation [11, 16–18] and pulsed laser deposition [19] as well as conventional moderate temperature chemical vapor deposition techniques [20–22]. They can be produced as single layer [13, 14], multi-layer [23, 24] or with a graded composition [10, 11, 20]. In fact, the majority of the commercial coatings available do not consist of a single layer of  $\text{TiC}_{1-x}\text{N}_x$  with a fixed composition, but show a gradient of the carbon composition from the interface to the coating surface that has been optimized with respect to the intended application. In the machining technology sector, titanium carbonitrides are used in interrupted cutting applications like milling, but also in punching/forming applications with high mechanical loads, tapping thread forming and plastic injection molding [25].  $\text{TiC}_{1-x}\text{N}_x$  coatings are also used as interlayer for other coatings like  $\kappa\text{-Al}_2\text{O}_3$  [26] or multilayer composite ceramic metal-DLC coatings [27].

Until now the tribology of the  $\text{TiC}_{1-x}\text{N}_x$  coatings is poorly understood due to the complexity of the system and tribo-mechanisms active. It is believed that the presence of carbon provides for the low-friction behavior at room temperature and ambient air conditions [12, 13] together with the presence of moisture, similar to other carbon containing coatings like DLC, in particular tetrahedral amorphous carbon [28].

The aim of this dissertation is therefore to investigate the friction and wear mechanisms present during sliding. The chemical composition of  $\text{TiC}_{1-x}\text{N}_x$  coatings was varied and ball-on-disk tests were performed on the films changing different parameters. These include temperature, load, velocity and, most importantly, the surrounding atmosphere in order to obtain evidence that the presence of moisture is necessary for the appearance of the low-friction effect. *In situ* analysis is also used to acquire detailed information about possible tribolayers formed.

Although the reduction of the use of lubricants during industrial applications is one aim in environmental conscious manufacturing, the quantification of the resources needed for the synthesis of the  $\text{TiC}_{1-x}\text{N}_x$  and other coatings is also an important aspect. Therefore, a mass and energy balance of a cathodic arc-evaporation process commonly used to deposit  $\text{TiC}_{1-x}\text{N}_x$  coatings was done providing useful data for further optimization of the process to reduce production costs and improve its efficiency.

## 1.2 Vapor deposition techniques

Physical vapor deposition processes involve atomization or vaporization of material from a solid source, its transport from the source to the substrate and deposition onto a substrate to form a coating. These processes, that take place in a reduced pressure environment, are often classified as evaporation and sputtering [29]. Within this work, direct current magnetron sputtering and cathodic arc evaporation were used and therefore a brief description of both techniques is presented, followed by a short section dedicated to thin film growth.

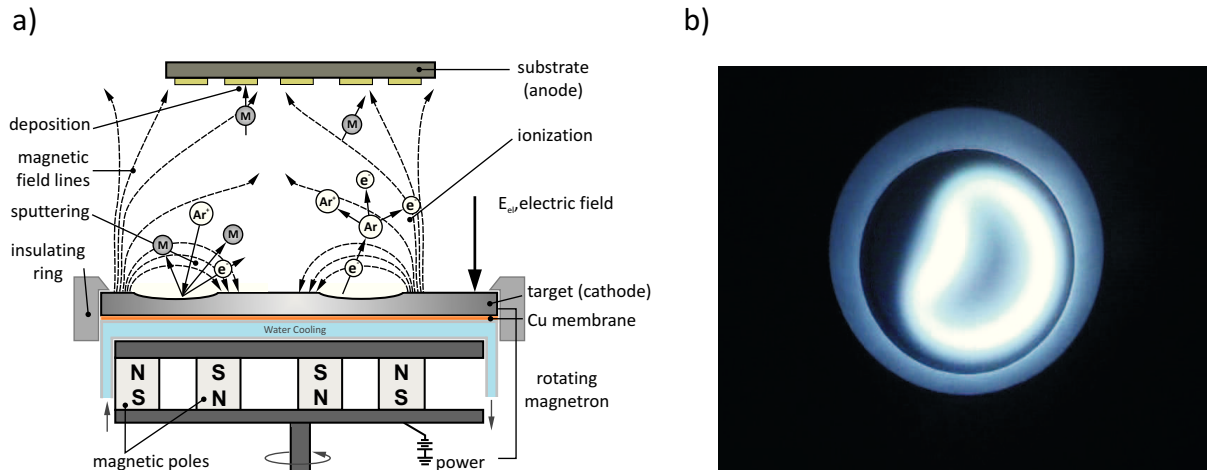


Figure 1.1: a) Schematic of a direct current unbalanced magnetron sputtering system modified after [32–35]; b) unbalanced magnetron configuration used in Oerlikon Balzers INNOVA.

### 1.2.1 Magnetron sputtering

Sputtering occurs in a vacuum atmosphere and is a process which involves the physical evaporation of atoms from a surface by momentum transfer from bombarding highly energetic atomic-sized particles. The bombarding energetic particles, which are usually ions of a heavy inert gas, impinge on the surface of the target, which is the source of the material, ejecting material primarily in atomic form. The substrates are positioned facing the mostly metallic target, so they intercept the flux of ejected atoms [30, 31]. To provide ion bombardment, the chamber will be backfilled with an inert gas, e.g. Ar, to a pressure varying from  $10^{-3}$  to  $10^{-1}$  mbar and an electric discharge is ignited to ionize the gas in the region adjacent to the target. Such a low pressure electric discharge is called a glow discharge and the ionized gas is called plasma. The target is negatively biased so that its surface is bombarded by positive ions with energies in the range from 100 to 1000 eV from the plasma. The sputtered material, which consists mainly of neutral atoms, has energies varying from 10 to 40 eV.

The coatings usually present low roughness making them useful for applications where optical or magnetic properties and electrical conductivity are necessary, but only low deposition rates can be achieved. To overcome this limitation, magnetic fields are applied (see Figure 1.1a) allowing the concentration and densification of the plasma in the space immediately above the target. As a result of trapping the electrons near the target surface by these so-called magnetrons, the ion bombardment and, hence, the sputtering rates are enhanced providing for a more efficient target utilization [36, 37]. Depending on the magnetic field lines looping between two magnets, magnetrons can have balanced or unbalanced configurations. If all field lines loop between two magnets, a conventional balanced magnetron is present. On the other hand, if the magnetic field lines are partially open towards the substrate, like in Figure 1.1a, the plasma is allowed to expand away from the target area. This configuration is entitled unbalanced magnetron [38, 39]. An important modification to the sputter coating technology mentioned above is by employing reactive gases to introduce one or more of the coating components in the gaseous form, like N, O or C. This modification is called reactive

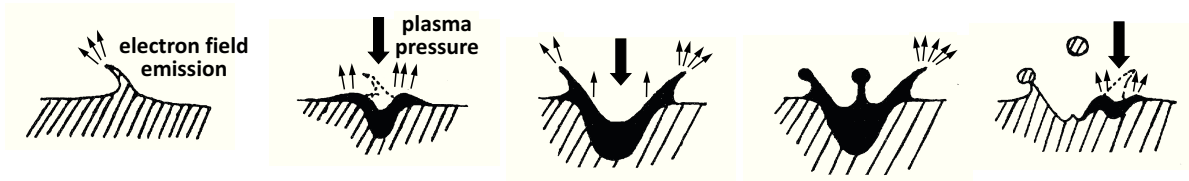


Figure 1.2: Sketch illustrating macroparticle generation [43].

sputtering [30].

Figure 1.1 shows a schematic of the system used to synthesize the  $\text{TiC}_{1-x}\text{N}_x$  coating analyzed in Publication IV. A  $\text{Ti}_2\text{CN}$  compound target was utilized and a rotating direct current unbalanced magnetron system with a “bean”-like form was applied (see Figure 1.1b) for a better target utilization. With this configuration, a stoichiometric high quality surface  $\text{TiC}_{1-x}\text{N}_x$  coating was deposited for the *in situ* tribological investigations. Further details are described in Publication IV.

### 1.2.2 Cathodic arc evaporation

In contrast to magnetron sputtering, the cathodic arc evaporation technique employs a vacuum arc, which is a high-current, low-voltage electrical discharge between two electrodes situated in a vacuum ambient, as means to generate vapor emission from a target (cathode). The arc is self-sustained by the evaporated material providing for the conducting medium. Arc discharges are characterized by high currents in the range from 30 A to some kA and low voltages in the range from 20 to 100 V. The arc is commonly initiated by a short contact between the cathode and a metal trigger finger. The current is concentrated in a luminous area of a few  $\mu\text{m}^2$  on the cathode and is denominated cathode spot or arc spot (see Figure 1 in Publication I). The processes taking place in the arc spot are a challenge to study and to quantify due to the extreme conditions (flash nature events) present in the spot. Therefore, there is still a controversy regarding the events occurring at the spot and the magnitude of the various physical values. Nevertheless, there is a general concord about some of the properties, namely: the arc spot has an extremely high current density varying from  $10^6$  to  $10^{12}$   $\text{A}/\text{m}^2$  and moves at a velocity of approximately 100 m/s over the surface of the cathode; the ignition and explosion of the spot takes 1-10 ns and its residence time is of the order of 100 ns [36, 40, 41]. The main advantage of cathodic arc evaporation for the synthesis of materials lies in the high percentage of ions in the emitted flux (10–100 %) and the high kinetic energy of these ions (10–150 eV). This leads to enhanced adhesion, increased film packing density and enables high deposition rates. Especially in the case of refractory cathode materials, multiply charged ions can occur. In general, it is possible to deposit stoichiometric coatings of good quality over a wide range of processing conditions [40, 42].

However, besides ions and neutrals, macroparticles or microdroplets are also produced. Such macroparticles are non-vaporised particles ejected from the cathode with a size that varies from 0.1 to 10  $\mu\text{m}$  [41, 43]. Figure 1.2 illustrates the formation of macroparticles. After the ignition of the arc spot on an asperity, the cathode material melts and part of it evaporates. Macroparticles are formed when a layer of liquid cathode material yields to



plasma pressure and are preferentially ejected with a 5 to 30° angle relative to the cathode surface. The just ejected macroparticles may rapidly cool down and freeze at the crater rim, forming microprotusions that can serve as field-enhancing objects for the ignition of the next emission spot [43]. The incorporation of macroparticles into the growing films is disadvantageous since it causes growth defects and increases roughness, making the coatings improper for applications where optical properties and electrical conductivity are important [41, 43]. To avoid the production and subsequent condensation of the macroparticles on the substrate, strategies have been developed. One strategy is to steer the cathode spot using magnet configurations not unlike those employed in magnetron sputtering. These magnet systems are placed on the back of the cathode and can increase the speed of motion of the cathode spot [36, 40]. Another strategy is the use of the filtered arc technique, where filters guide the plasma away from the path of the macroparticles and effectively allow the placement of the cathode out of sight from the substrate [41].

Reactive deposition is also possible with cathodic arc evaporation and is in fact widely used. The most typical compound coatings are oxides, nitrides, and carbides, and are employed in wear resistant or decorative applications [40]. Publication II and III present the results of investigations performed on  $\text{TiC}_{1-x}\text{N}_x$  coatings, with a graded and homogeneous composition, respectively, which were synthesized by cathodic arc evaporation. The Ti targets were evaporated in an  $\text{Ar}/\text{C}_2\text{H}_2/\text{N}_2$  atmosphere resulting in the synthesis of  $\text{TiC}_{1-x}\text{N}_x$  on the substrates.

### 1.2.3 Thin film growth

After the exposure of the substrate surface to the incident vapor of the target material, atoms or ions are either reflected immediately, re-evaporate after some residence time, or condense on the surface. If the particles do not immediately react with the surface, the so-called adatoms will have some degree of mobility on the surface before they condense. An impinging flux of film species must first be thermally accommodated with the substrate. Atoms will condense on the surface at a cooling rate of  $\sim 10^{13} \text{ K}\cdot\text{s}^{-1}$  [44] by losing energy, finding preferential nucleation sites, like lattice defects, atomic steps, point defects or grain boundaries and bonding to other atoms. At high impingement rates, metastable and stable clusters are formed and can continue growing by binding of diffusing adatoms or by direct capture of atoms. Once a metastable cluster reaches a critical size of two or three atoms, if supersaturation is high, neighbor crystals might come into contact starting the coalescence stage [31, 45, 46]. Many observations of subsequent film formation have pointed to three basic growth modes: island or Volmer-Weber, which occurs when the smallest stable clusters nucleate on the substrate and grow in three dimensions to form islands; layer-by-layer or Frank-Van der Merve growth takes place when the binding energy between film atoms is equal to or less than that between the film atoms and the substrate; and Stransky-Krastanov, a combination of the two, where first one or more monolayers are formed and then, when it becomes energetically favourable, three dimensional islands form [36, 46].

Film growth depends on both nucleation and growth kinetics where selection processes occur determining the coating structure. To relate the observed structure to the deposition parameters, structure zone diagrams (SZDs) were developed. A SZD is an over simplistic representation of expected film microstructure trends versus deposition parameters and it is based on experimental data obtained out of various physical vapor deposition techniques





to describe the energy and material balances of complex systems. From a historical point of view, it was a potent tool in the 1920s to describe the thermal balances of production plants of glass and cement and to optimize the energy input, since resources were scarce. In the 1930s, steel and iron played a major role for the Nazi Germany and their efficient use was highlighted with Sankey diagrams. Since the 1990s, these diagrams have become common for presenting data in life cycle assessments of products [55].

Sankey diagrams have been shown in a variety of manners and used for many different problems. Therefore, the definite Sankey diagram does not exist. Its versatility is probably the reason for the diagram's success. To build a Sankey diagram there are no rules, except those of visual perception and intuition. Despite this, a few aspects have been assumed implicitly by users: diagrams concern quantity sizes that are related to a period of time or to a functional unit; the quantity sizes are extensive sizes, i.e., quantities that are proportional to the material quantity; inventories are not taken into account, i.e. there is no stock formation, and energy or mass balance is maintained [55, 56].

## 1.4 Tribology

Tribology is defined as the science and technology of interacting surfaces in relative motion and it embraces the study of friction, wear and lubrication [57]. These three fields will be briefly explained in the sections below.

### 1.4.1 Friction

Friction may be defined as the resistance to motion encountered by one body when moving tangentially over another with which it is in contact. Thus friction is not a material property but a system response in the form of a reaction force, which acts in the direction opposite to the motion and is denominated friction force. Friction is characterized by three basic laws: the friction force  $F$  is proportional to the normal force  $w$  :  $F = \mu w$ , where  $\mu$  is the coefficient of friction (COF); the friction force is independent of the apparent area of contact, thus large and small objects have the same COFs; the friction force is independent of the sliding velocity. Usually, the first two laws are well obeyed although the third one is only valid once sliding is already established [29, 57–59]. In 1981, Suh and Sin developed a theory named “genesis of friction” [60]. According to this theory the friction force, and consequently the COF, is influenced by the sliding distance and the environment because of the changing contributions of three components of friction, i.e. due to the adhesion of flat portions of the sliding surface, due to plowing by wear particles and hard asperities and due to the deformation of surface asperities. These three mechanisms are present during the six stages that friction experiences in the running-in period before reaching steady-state, as Figure 1.5 illustrates. Further details can be found in the References [29, 60].

### 1.4.2 Wear

Wear, as well as friction, is the result of the same tribological contact process between two moving surfaces and is defined as the removal of material from the solid surfaces during sliding. However, their interrelationship is not yet completely understood. For design and

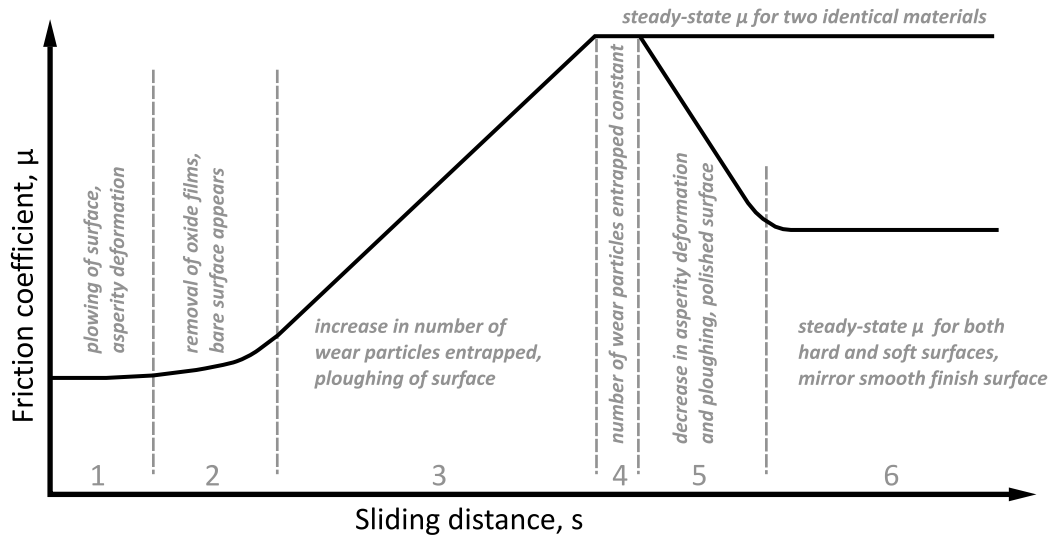


Figure 1.5: The six stages of friction versus sliding distance for steel counterparts, modified after [60].

material purposes it is necessary to have some universal quantitative parameter of wear. Therefore, Holm (1946) and Archard (1953) formulated the concept of the wear rate  $K$ , which is the worn-off volume  $V$  divided by the applied normal force  $w$  times the sliding distance  $s$ , and it is usually given with the dimensions  $[\text{m}^3 / \text{N}\cdot\text{m}]$ :

$$K = \frac{V}{w \cdot s}$$

There is no general agreement about the classification of the wear mechanisms, but the most common wear classification was reviewed by Blau in 1989 [61] and consists of four basic wear mechanisms: adhesion, abrasion, surface fatigue and chemical wear [29, 62]. The complete tribological process in a contact in relative motion is very complex as it involves friction and wear, and deformation mechanisms at different scale levels and of different types. Therefore, to achieve a general understanding of the complete tribological process taking place for coatings and understand its interactions, Holmberg and Matthews proposed to analyse separately the tribological changes of five types: macromechanical friction and wear mechanisms, micromechanical tribological mechanisms, tribochemical mechanisms, nanophysical contact mechanisms and mechanisms of material transfer [63].

Within this work, the velocity accommodation mode concept, developed by Berthier et al. [64, 65], was employed to classify the micromechanical tribological mechanisms present in the contact between the  $\text{Al}_2\text{O}_3$  counterpart and  $\text{TiC}_{1-x}\text{N}_x$  coating. Velocity accommodation is defined as the manner in which the difference in velocity between two bodies in relative motion is accommodated across the interface and is schematically represented in Figure 1.6. The place for velocity accommodation can either be in one of the solids ( $S_1$  and  $S_5$ ), in the intermediate material ( $S_2$  or  $S_4$ ) or at the interface between both ( $S_3$ ). Four basic modes are defined to describe how the velocity is accommodated: elasticity, fracture, shear and rolling. Thus, velocity can be accommodated through 20 different mechanisms (5 sites and 4 modes per site). The accommodation sites and modes depend on the material properties,

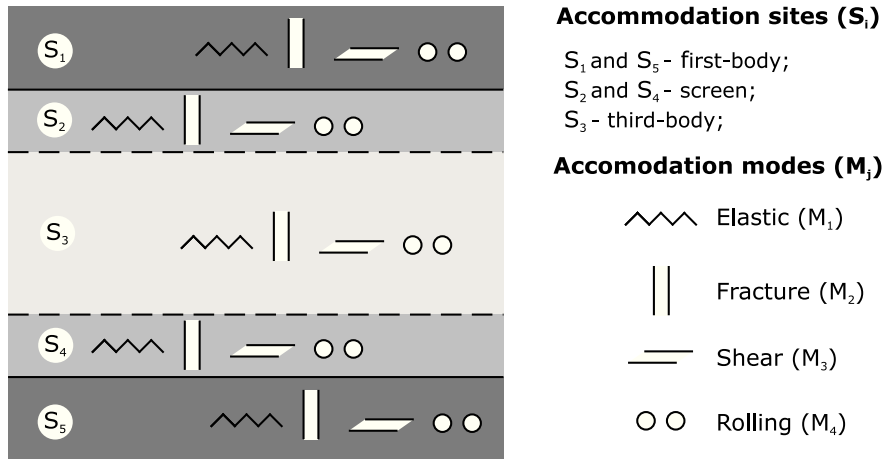


Figure 1.6: The mechanisms of velocity accommodation of two surfaces in relative motion, modified after [64].

environment and loads. Hence, the same contact can theoretically accommodate velocity differences through one or any combination of the 20 mechanisms (S<sub>i</sub>M<sub>j</sub>). Further details can be found in Reference [64].

With this approach the friction and the wear mechanisms are defined in terms well-known from materials science and mechanical engineering. Further, the properties can be derived from known parameters like strength, fracture toughness, Young’s modulus of elasticity or rolling resistance. On the other hand, when the whole contact system is split up into very small parts, it becomes difficult to find a way to handle the interactions of the different parts with each other and until today there are no satisfactory analytical models to describe many of the different mechanisms in velocity accommodation [29, 64]. Visualisation techniques like *in situ* tribometry [66] are used to identify both velocity accommodation sites and modes. This technique will be explained in section 1.5.2 and was applied in Publication IV.

### 1.4.3 Lubrication

The most common way of reducing friction and wear is to introduce a lubricant, traditionally a liquid or a grease, between two moving surfaces. However, when the service conditions become very severe, i.e. very high pressures, reactive environments, high vacuum, very high or cryogenic temperatures, the use of solid lubricants comes into play [29, 67]. When present at the sliding surface, solid lubricants, similar to its liquid pairs, shear easily to provide low friction and prevent wear damage between the sliding surfaces. The current direction in modern tribology is to limit or reduce the use of liquid lubricants due to the above mentioned limitations but also due to environmental concerns, forwarding the increasing use of solid materials. Nowadays, most solid lubricants are produced as thin film solids on sliding surfaces deposited by physical or chemical vapor deposition techniques. In the majority of the cases, a transfer film is formed on the sliding surfaces achieving low-friction and long wear lives in most solid lubricated surfaces [68, 69]. Donnet presented a classification (see Table 1.1) of the commonly used solid lubricant coatings based on the chemistry, crystal structure, lubricity and hardness [67].

Table 1.1: General overview of the classification of solid lubricant coatings, modified after [67].

	Classification	Examples
Soft coatings ( $H < 10$ GPa)	Lamellar	MoS <sub>2</sub> , WSe <sub>2</sub> , Graphite, (CF <sub>x</sub> ) <sub>n</sub>
	Non-lamellar	CaF <sub>2</sub> , BaF <sub>2</sub> , PbO–SiO <sub>2</sub>
	Polymers	PFTE, Polyimide
	Soft metals	Au, Ag, Pb, Sn, In
Hard coatings ( $H > 10$ GPa)	Diamond-like	a-C, a-C:H, a-C:H:Si, a-C:H:Metal
	Oxides	TiO <sub>2-x</sub> , VO <sub>x</sub> , B <sub>2</sub> O <sub>3</sub> , CdO
	Carbides	WC, SiC, B <sub>4</sub> C
	Nitrides <sup>1</sup>	TiN, c-BN
	Borides <sup>1</sup>	TiB <sub>2</sub>

<sup>1</sup>No information on the shearing mode of TiN and TiB<sub>2</sub> is given in the reference.

Even though widely used, also solid lubricants present limitations: in their majority they are poor thermal conductors; their frictional behavior depends on the surrounding atmosphere; their lifetime is finite; oxidation- and aging-related degradation may occur; exposure to high temperatures and oxidative environments may provoke the generation of non-lubricious by-products [69].

In the last years, researchers have developed coatings that are designed to adapt to changing conditions of tribological applications. These are called “adaptive” or “chameleon” solid lubricant coatings [70]. As a novel approach, researchers have recently bound solid lubricant films with smart surface engineering strategies, such as micro-structuring and/or -patterning, thus achieving higher levels of performance and durability under severe tribological conditions [68].

## 1.5 Coating characterization

The TiC<sub>1-x</sub>N<sub>x</sub> coatings investigated in this work were characterized concerning their chemical composition as well as mechanical and tribological properties. However, in this chapter only selected techniques that were used and which are not that common in coating characterization will be explained.

### 1.5.1 Raman spectroscopy

Raman spectroscopy is a non-destructive technique primarily used for structural characterization. This technique is based on the Raman effect, first discovered by Raman and Krishnan in 1928, which occurs from the interaction of light with a molecule or a crystal [71]. As a monochromatic light beam impinges the sample, the electric field of the incident radiation distorts the electron clouds that make up the chemical bonds. The majority of the incident beam is re-radiated at the same frequency and is known as Rayleigh scattering. However, a small portion of the photons transfers a part of their energy to the sample exciting vibrational modes of the crystal lattice (Stokes scattering) or gains energy due to the

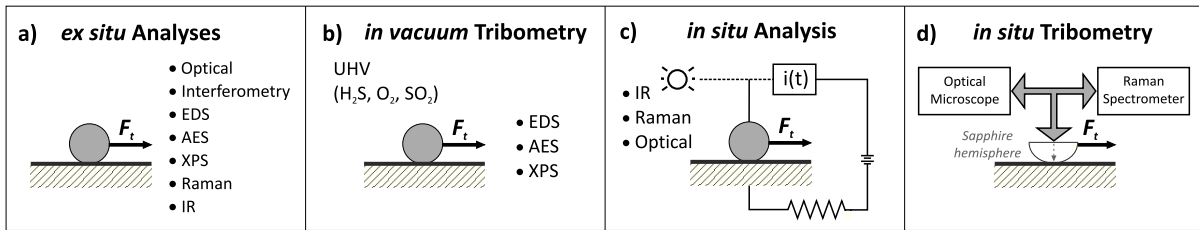


Figure 1.7: Four analytical approaches to investigate the formation of third bodies in tribological contacts (modified after [76]).

annihilation of vibrational modes (anti-Stokes scattering). Although Stokes and anti-Stokes peaks are symmetrically positioned relative to the Rayleigh line, their intensities may differ. The Raman spectra are usually represented relative to the Rayleigh line and the so-called Raman shift is given as wave number ( $\text{cm}^{-1}$ ). Raman spectroscopy in general is sensitive to grain-size effects, defects and disorder in the structure and to changes in stoichiometry. It is widely used to provide information on chemical structures and physical forms as well as to identify substances from the characteristic spectral patterns that serve as “fingerprints” [71–74]. In a further approach, a standard Raman spectrometer can be combined with a movable microscope stage which allows for raster scanning of the whole surface of interest and not only one point. This technique is called Raman mapping and can be used to extract the chemical information from each spectrum creating a map of the chemical components distribution in a sample with a lateral resolution of a few micrometers. By selecting the wave number range of a peak that is typical for the investigated compound, its intensity in dependence on the position can be depicted. The Raman maps can contain up to a few thousand of points [75].

Raman spectroscopy was performed on the  $\text{TiC}_{1-x}\text{N}_x$  coating and counterpart wear scars after tribological tests performed in different atmospheres (see Publication II, III and IV). The obtained spectra provided information whether transfer films were formed or not and revealed details about the chemical nature of these third bodies. Raman maps, as shown in Figure 6 of Publication II, were recorded to gain additional information regarding the spatial distribution of the transfer films within the tribological contact. These measurements were done subsequent to the tribological tests, i.e. *ex situ* analysis which is in contrast to the *in situ* methods described in the following section.

### 1.5.2 In situ tribometry

Understanding the mechanisms within a sliding contact is a complicated task due to the buried nature of the interface. These mechanisms include, for example, the formation of a transfer film or third body at the interface separating the counterparts, changes of the thickness of the transfer film, composition of films or loss of material as debris [66]. In Reference [76] Singer et al. reviewed four possible analytical approaches to investigate these effects in the tribological contact (see Figure 1.7).

Traditionally, the contacting bodies need to be separated before analysis. This *ex situ* approach, in combination with modern surface analytical techniques (Figure 1.7a) provides useful information on the mechanisms active within the contact, i.e. how transfer films form,



what is their chemistry and structure or how they participate in the sliding process (see Reference [77] as an example). However, exposing the contacting surfaces to ambient air might cause significant changes, e.g. due to oxidation or contamination, and lead to wrong conclusions.

To minimize contamination, the chemistry of the interface can be assessed using the so-called *in vacuum* tribometry. Contamination can then be hindered by performing friction tests and then separating and analyzing surfaces in a chamber with a well-controlled environment (Figure 1.7b). For example, Singer et al. [78] studied the tribological behavior of SiC sliding against Mo in SO<sub>2</sub>, O<sub>2</sub> and H<sub>2</sub>S atmospheres in an ultrahigh vacuum chamber performing Auger electron and X-ray photoelectron spectroscopy on the wear scars in the coating and counterpart. As can be seen by this example, the *in vacuum* approach also allows for studying tribological contact conditions in non-ambient atmospheres. The shortcoming of this approach is that no real time information during sliding can be obtained.

Therefore, the even more powerful *in situ* analysis approach has been established (Figure 1.7c), where the sliding can be probed directly, either on the counterpart or on the coating wear track, applying various analytical methods:

- ⇒ Wahl et al. monitored the appearance of third bodies between the sliding pair MoS<sub>2</sub> / steel by measuring changes in the **electrical contact resistance** of the steel counterpart [66].
- ⇒ Bair et al. measured the flash temperatures by **infra-red emissions** between the asperities of a read/write head slider bearing in hard magnetic recording disks [79].
- ⇒ Jullien et al. tested a carbon based composite for lubricated clutch applications in continuous slipping. During slipping the contact was analyzed by **optical microscopy** with a side visualization configuration [80].
- ⇒ Muratore et al. monitored changes at high temperatures in the surface chemistry observed on a MoS<sub>2</sub> coating wear track during testing against a steel counterpart using **micro Raman spectroscopy** [81]. This allowed for the identification of chemical species that are only active during the test. Another example is the work carried out by Cheng et al., where **ultraviolet Raman spectroscopy** was used to analyze the chemical changes experienced by some lubricants in the interface between a chrome steel ball and a sapphire flat, when subjected to different loading conditions [82]. The ultraviolet laser beam was focused on the lubricated contact through the sapphire flat.

When a real time spectroscopic technique is combined with optical microscopy (Figure 1.7d), the so-called *in situ* tribometry approach is possible. The set-up consists of a crystalline, transparent Al<sub>2</sub>O<sub>3</sub> (sapphire) hemisphere which is used as counterpart for the sliding test and is also connected to an optical microscope. The optical microscope can either be used to visually observe the sliding contact, or to perform micro Raman spectroscopy to identify the composition of third bodies. By the direct observation and digital video recording of the contact during testing, the velocity accommodation modes (described in section 1.4.2) present during sliding can be identified as well as the appearance and change in thickness of third bodies. Using image frame captures taken directly from the digital video recordings

of the test, the transfer film thickness can be measured by monitoring the movement of optical interference fringes, i.e. Newton's rings, for a ball-on-flat geometry during the friction testing. For white light conditions, each time the fringes move inward by one whole fringe (e.g. ring order  $n + 1$  moves to where  $n$  was originally located) the transfer film increases in thickness, whereas when fringes move outward it corresponds to a decrease [83, 84]. This *in situ* spectroscopic approach allows therefore for the correlation between third body processes with the friction and wear behavior. An example of this approach can be found in Reference [85] where the tribological contact conditions between annealed boron carbide and Mo-S-Pb and sapphire were studied. As a final remark it should be pointed out that combinations between the described four approaches (see Figure 1.7) are possible and in fact are used nowadays to reveal more details about the tribological contact conditions.

Within this work, *in situ* Raman spectroscopy was performed on the  $\text{TiC}_{1-x}\text{N}_x$  coating wear track during a tribological test against an  $\text{Al}_2\text{O}_3$  counterpart, where spectra were recorded at intervals of approximately 500 sliding cycles. The spectra together with the COF curves revealed that the appearance of C-H bonds coincides with the beginning of the low friction regime. *In situ* tribometry was also used within the frame of this work. The sliding contact between the  $\text{TiC}_{1-x}\text{N}_x$  coating and the sapphire hemisphere counterpart was monitored by optical microscopy and digital video recordings, allowing for the identification of velocity accommodation modes present and the quantification of the third body thickness during testing. A more detailed explanation can be found in Publication IV.

## References

- [1] S. PalDey and S. C. Deevi, *Mater. Sci. Eng. A*, 2003, **342**, 58–79.
- [2] J. Lin, B. Mishra, J. J. Moore, and W. D. Sproul, *Surf. Coat. Technol.*, 2006, **201**, 4329–4334.
- [3] C. Mitterer, P. Losbichler, F. Hofer, P. Warbichler, P. N. Gibson, and W. Gissler, *Vacuum*, 1998, **50**, 313–318.
- [4] *CRC Handbook of Chemistry and Physics, 85th ed.* Ed. D. R. Lide, CRC Press, Boca Raton, 2004.
- [5] P. H. Mayrhofer and M. Stoiber, *Surf. Coat. Technol.*, 2007, **201**, 6148–6153.
- [6] J. G. Han, J. S. Yoon, H. J. Kim, and K. Song, *Surf. Coat. Technol.*, 1996, **86–87**, 82–87.
- [7] S. Veprek and S. Reiprich, *Thin Solid Films*, 1995, **268**, 64–71.
- [8] A. Forn, J. A. Picas, G. G. Fuentes, and E. Elizalde, *Int. J. Refract. Met. Hard Mater.*, 2001, **19**, 507–513.
- [9] P. H. Mayrhofer, C. Mitterer, L. Hultman, and H. Clemens, *Prog. Mater Sci.*, 2006, **51**, 1032–1114.
- [10] S. J. Bull, D. G. Bhat, and M. H. Staia, *Surf. Coat. Technol.*, 2003, **163–164**, 499–506.
- [11] L. Karlsson, L. Hultman, M. P. Johansson, J. E. Sundgren, and H. Ljungcrantz, *Surf. Coat. Technol.*, 2000, **126**, 1–14.

- [12] T. Polcar, R. Novak, and P. Siroky, *Wear*, 2006, **260**, 40–49.
- [13] E. Vancoille, J. P. Celis, and J. R. Roos, *Wear*, 1993, **165**, 41–49.
- [14] J. Deng and M. Braun, *Surf. Coat. Technol.*, 1994, **70**, 49–56.
- [15] S. W. Huang, M. W. Ng, M. Samandi, and M. Brandt, *Wear*, 2002, **252**, 566–579.
- [16] E. Damond, P. Jacquot, and J. Pagny, *Mater. Sci. Eng. A*, 1991, **140**, 838–841.
- [17] W. Precht, E. Lunarska, A. Czyzniewski, M. Pancielejko, and W. Walkowiak, *Vacuum*, 1996, **47**, 867–869.
- [18] O. Knotek, F. Löffler, and G. Krämer, *Vacuum*, 1992, **43**, 645–648.
- [19] J. M. Lackner, W. Waldhauser, and R. Ebner, *Surf. Coat. Technol.*, 2004, **188–189**, 519–524.
- [20] K. Narasimhan, S. P. Boppana, and D. G. Bhat, *Wear*, 1995, **188**, 123–129.
- [21] S. Kudapa, K. Narasimhan, P. Boppana, and W. C. Russell, *Surf. Coat. Technol.*, 1999, **120–121**, 259–264.
- [22] H. G. Prengel, W. R. Pfouts, and A. T. Santhanam, *Surf. Coat. Technol.*, 1998, **102**, 183–190.
- [23] C. Wei, J. Fin Lin, T.-H. Jiang, and C.-F. Ai, *Thin Solid Films*, 2001, **381**, 94–103.
- [24] E. Bemporad, C. Pecchio, S. De Rossi, and F. Carassiti, *Surf. Coat. Technol.*, 2001, **146–147**, 363–370.
- [25] Oerlikon Balzers Balinit B,  
[http://www.oerlikon.com/ecomaXL/index.php?site=BALZERS\\_EN\\_balinit\\_b](http://www.oerlikon.com/ecomaXL/index.php?site=BALZERS_EN_balinit_b), 2010.
- [26] D. Hochauer, C. Mitterer, M. Penoy, C. Michotte, H. P. Martinz, and M. Kathrein, *Surf. Coat. Technol.*, 2010, **204**, 3713–3722.
- [27] A. A. Voevodin, J. M. Schneider, C. Rebholz, and A. Matthews, *Tribol. Int.*, 1996, **29**, 559–570.
- [28] H. Ronkainen, J. Koskinen, J. Likonen, S. Varjus, and J. Vihersalo, *Diamond Relat. Mater.*, 1994, **3**, 1329–1336.
- [29] K. Holmberg and A. Matthews, *Coatings Tribology - Properties, Techniques and Applications in Surface Engineering*, Elsevier, Amsterdam, 2009.
- [30] J. A. Thornton, *Deposition Technologies for Films and Coatings - Developments and Applications*, ed. R. Bunshah, Noyes Publications, New Jersey, 1982.
- [31] D. M. Mattox, *Handbook of Physical Vapor Deposition (PVD) Processing, 2nd edition*, Elsevier, Oxford, 2010.
- [32] P. H. Mayrhofer, Ph.D. Thesis, Montanuniversität Leoben, 2001.
- [33] W. D. Sproul, *Surf. Coat. Technol.*, 1991, **49**, 284–289.
- [34] D. Smith, *Thin-Film Deposition: principle and practice*, McGraw-Hill, New York, 1995.
- [35] M. Moser, Ph.D. Thesis, Montanuniversität Leoben, 2008.
- [36] M. Ohring, *The Materials Science of Thin Films - Deposition and Structure, 2nd edition*, Academic Press, San Diego, 2002.

- [37] J. E. Mahan, *Physical Vapor Deposition of Thin Films*, Wiley-Interscience, New York, 2000.
- [38] B. Window, *Surf. Coat. Technol.*, 1996, **81**, 92–98.
- [39] M. Zongxin, L. Guoqing, C. Deliang, H. Kaiyu, and L. Cui, *Surf. Coat. Technol.*, 2005, **193**, 46–49.
- [40] P. Johnson, *in: Thin Film Processes II*, ed. J. Vossen and W. Kern, Academic Press, San Diego, 1991.
- [41] U. Helmersson, M. Lattemann, J. Bohlmark, A. P. Ehiasarian, and J. T. Gudmundsson, *Thin Solid Films*, 2006, **513**, 1–24.
- [42] R. L. Boxman, P. J. Martin, and D. M. Sanders, *Handbook of Vacuum Arc Science and Technology*, Noyes Publications, New Jersey, 1995.
- [43] A. Anders, *Cathodic Arcs - from Fractal Spots to Energetic Condensation*, Springer Science + Business Media, LLC, New York, 2008.
- [44] T. W. Barbee Jr, W. H. Holmes, D. L. Keith, M. K. Pyzyna, and G. Ilonca, *Thin Solid Films*, 1977, **45**, 591–599.
- [45] H. Jehn, *in: Advanced Techniques for Surface Engineering*, ed. W. Gissler and H. Jehn, Kluwer Academic Publisher, Dordrecht, 1992.
- [46] J. Greene, *in: Handbook of Deposition Technologies for Films and Coatings*, ed. R. Bunshah, Noyes Publications, Park Ridge, 1994.
- [47] A. Anders, *Thin Solid Films*, 2010, **518**, 4087–4090.
- [48] B. A. Movchan and A. Demchishin, *Phys. Metals Metallogr.*, 1969, **28**, 653.
- [49] P. B. Barna and M. Adamik, *Thin Solid Films*, 1998, **317**, 27–33.
- [50] J. A. Thornton, *J. Vac. Sci. Technol.*, 1974, **11**, 666–670.
- [51] R. Messier, A. P. Giri, and R. A. Roy, *J. Vac. Sci. Technol. A*, 1984, **2**, 500–503.
- [52] I. Petrov, F. Adibi, J. E. Greene, L. Hultman, and J. E. Sundgren, *Appl. Phys. Lett.*, 1993, **63**, 36–38.
- [53] I. Petrov, P. Barna, L. Hultman, and J. Greene, *J. Vac. Sci. Technol. A*, 2003, **21**, 117–128.
- [54] H. R. Sankey, *Minutes of Proceedings of the Institution of Civil Engineers*, 1896, **125**, 182–242.
- [55] M. Schmidt, *J. Ind. Ecol.*, 2008, **12**, 82–94.
- [56] M. Schmidt, *J. Ind. Ecol.*, 2008, **12**, 173–185.
- [57] I. Hutchings, *Tribology - Friction and Wear of Engineering Materials*, Edward Arnold, London, 1992.
- [58] B. Bunshah, *Principles and Applications of Tribology*, John Wiley & Sons, New York, 1999.
- [59] E. Rabinowicz, *Friction and Wear of Materials, 2nd edition*, Wiley-Interscience, New York, 1995.

- [60] N. P. Suh and H. C. Sin, *Wear*, 1981, **69**, 91–114.
- [61] P. J. Blau, *Friction and Wear Transitions of Materials: Break-in, Run-in, and Wear-in*, Noyes Publications, New Jersey, 1989.
- [62] F. Bowden and D. Tabor, *The Friction and Lubrication of Solids*, Clarendon Press, Oxford, 1954.
- [63] K. Holmberg, A. Matthews, and H. Ronkainen, *Tribol. Int.*, 1998, **31**, 107–120.
- [64] Y. Berthier, M. Godet, and M. Brendle, *Tribol. Trans.*, 1989, **32**, 490–496.
- [65] Y. Berthier, L. Vincent, and M. Godet, *Eur. J. Mech. A. Solids*, 1992, **11**, 35–47.
- [66] K. J. Wahl, M. Belin, and I. L. Singer, *Wear*, 1998, **214**, 212–220.
- [67] C. Donnet, *Condensed Matter News*, 1995, **4**, 9–24.
- [68] C. Donnet and A. Erdemir, in: *Materials Surface Processing by Directed Energy Techniques*, ed. Y. Pauleau, Elsevier, Oxford, 2006.
- [69] A. Erdemir, in: *Modern Tribology Handbook, Vol. 2*, ed. B. Bhushan, CRC Press, Boca Raton, 2001.
- [70] C. Muratore and A. A. Voevodin, *Annual Review of Materials Research*, 2009, **39**, 297–324.
- [71] E. Smith and G. Dent, *Modern Raman Spectroscopy - A Practical Approach*, John Wiley & Sons Ltd, Chichester, 2005.
- [72] R. McCreery, *Raman Spectroscopy for Chemical Analysis*, Wiley-Interscience, New York, 2000.
- [73] C. R. Brundle, C. A. Evans, and S. Wilson, *Encyclopedia of Materials Characterization*, Butterworth-Heinemann, Boston, 1992.
- [74] *Surface and Thin Film Analysis - A Compendium of Principles, Instrumentation, and Applications*, ed. H. Bubert and H. Jenett, WILEY-VCH, Dortmund, 2002.
- [75] O. Hollricher, *Confocal Raman Microscopy*, ed. T. Dieing, O. Hollricher, and J. Toporski, Springer, Heidelberg, 2011.
- [76] I. L. Singer, S. D. Dvorak, K. J. Wahl, and T. W. Scharf, *J. Vac. Sci. Technol. A*, 2003, **21**, 232–240.
- [77] I. L. Singer, *Applications of Surface Science*, 1984, **18**, 28–62.
- [78] I. L. Singer, T. Le Mogne, C. Donnet, and J. M. Martin, *J. Vac. Sci. Technol. A*, 1996, **14**, 38–45.
- [79] S. Bair, I. Green, and B. Bhushan, *J. Tribol.*, 1991, **113**, 547–554.
- [80] A. Jullien, M. H. Meurisse, and Y. Berthier, *Wear*, 1996, **194**, 116–125.
- [81] C. Muratore, J. E. Bultman, S. M. Aouadi, and A. A. Voevodin, *Wear*, 2011, **270**, 140–145.
- [82] U. C. Cheng and P. C. Stair, *Tribol. Lett.*, 1998, **4**, 163–170.
- [83] K. J. Wahl, R. R. Chromik, and G. Y. Lee, *Wear*, 2008, **264**, 731–736.

- [84] R. R. Chromik, C. C. Baker, A. A. Voevodin, and K. J. Wahl, *Wear*, 2007, **262**, 1239–1252.
- [85] I. L. Singer, S. D. Dvorak, and K. J. Wahl, NordTrib2000, 9th Nordic Conference on Tribology, 2000, pp. 31–41.

## 2 Summary

The aim of this dissertation was to develop a detailed understanding about the tribological phenomena behind the low friction and moderate wear behavior present in ambient air for the well-known Ti-C-N system. In this way, it can serve as a model for other material systems with low to medium contents of incorporated carbon. In addition, prior to the tribological investigations, a detailed analysis of the resources needed to deposit  $\text{TiC}_{1-x}\text{N}_x$  in a commercial deposition plant was performed.

In order to analyze the energy and mass fluxes involved during the synthesis of a  $\text{TiC}_{1-x}\text{N}_x$  coating on drills by cathodic arc evaporation, an evaluation concept was developed. The deposition cycle with a total duration of 3 h 26.5 min was divided in six sequential steps: vacuum pumping, plasma heating, plasma etching,  $\text{TiC}_{1-x}\text{N}_x$  deposition, cooling and venting. Regarding the mass balance performed on the gas fluxes, it was possible to observe that the main gas contribution in the deposition process comes from the Ar (68 % from total) used during the  $\text{TiC}_{1-x}\text{N}_x$  deposition step, although it was not incorporated in the coating. In fact, the majority of the gases inserted into the chamber were pumped out (99 % from total). Only a fraction of 12 and 5 % of the C and N atoms, respectively, which were inserted via the gases  $\text{C}_2\text{H}_2$  and  $\text{N}_2$ , were incorporated into the  $\text{TiC}_{1-x}\text{N}_x$  coating on the drills. Further, the mass balance of the solid fluxes indicated that a fraction of 9 % of the total Ti evaporated from four targets used was incorporated into the coating on the drills. For the energy balance, the total energy flux of 29.34 kW during the complete arc process was divided into three main components: Pumping (27 %), Heating and Etching (53 %), and Arc evaporation (20 %). The component Heating and Etching needs the biggest share of the total consumption, where the radiation heaters consume a fraction of almost 3/4.

The tribological investigations on the  $\text{TiC}_{1-x}\text{N}_x$  coatings were performed in a ball-on-disk configuration against  $\text{Al}_2\text{O}_3$  counterparts. A variation of the testing atmosphere (ambient air, Ar,  $\text{N}_2$  and dry air) confirmed that the low-friction effect of  $\text{TiC}_{1-x}\text{N}_x$  is tightly connected to the presence of atmospheric moisture, since it was only observed for ambient air. These tests also revealed that the steady-state low friction behavior is not affected by changes in the carbon composition of the  $\text{TiC}_{1-x}\text{N}_x$  coatings or by changes in load and sliding velocity. Only the extension of the running-in period with high friction was influenced by these variations. Tribological tests performed in ambient air varying the testing temperature from room temperature to 200 °C, showed that the coefficient of friction has an almost linear dependency on the testing temperature leading to the notion that water adsorption at the surface of the wear scar is the key step for the low friction mechanism. Further, tribological tests executed with different levels of relative humidity in the surrounding atmosphere allowed the revelation of its minimum level required to trigger the low friction behavior. The on-set point for the low-friction regime, with a coefficient of friction as low as 0.2, takes place at atmospheres with relative humidity levels between 15 and 25 %.

*Ex situ* Raman analysis performed on the coating and the  $\text{Al}_2\text{O}_3$  counterpart wear scars

after the tests in different atmospheres at room temperature generated valuable information about the constitution of possible formed tribolayers. The presentation of the chemical constitution of the wear scars by means of Raman maps evidenced the presence of bands typical of amorphous carbon for all the conditions. On the other hand, only in moist atmosphere compounds containing C–H bonds were detected leading to the notion that its presence provides for the low-friction behavior. These results confirmed the common tenor within the literature about the tribological properties of carbon containing coatings like DLC that the adsorption of water saturates dangling bonds and by that separates the two counterparts via a low shear.

In order to obtain more information about the formation of the tribolayer, in particular how and when it happens, *in situ* optical and spectroscopic techniques were used to investigate the early stages of the tribological process with a focus on the transition from the running-in period to the steady-state regime. These real-time techniques allowed for the correlation of the composition and thickness of the tribolayer in the contact area to the coefficient of friction measured. From the direct observation of the tribological contact, it was possible to observe that the transfer film is formed by abrasion of the coating and shearing of the removed material during the high friction component of the running-in period. Further, the appearance and thickening of this transfer film marks the beginning of the steady-state low-friction regime. The velocity accommodation mode present during this regime of the friction trace is interfacial sliding between the transfer film and the coating. *In situ* Raman analyzes performed on the coating wear track during an entire test revealed that the appearance of C–H bonds coincides with the beginning of the steady-state low-friction regime and the build-up of the transfer film.

In summary, the investigations on the Ti-C-N system have enabled to establish a model for the understanding of the tribology of coatings with low to medium contents of incorporated carbon that can be used in dry-sliding conditions to reduce the usage of lubricants harmful to the environment. The quantification of resources needed for the deposition of this self-lubricating system by cathodic arc evaporation can serve as an instrument for further optimization of the process in terms of energy and resource efficiency. The reduction in usage of hazardous materials and improvement of the efficiency of manufacturing processes are key aspects in the globalized market and conservation of the natural environment.



# 3 Publications

## 3.1 List of included publications

- I. Analysis of energy and mass fluxes during deposition of TiCN hard coatings by cathodic arc evaporation,  
*M. Rebelo de Figueiredo, R. Franz, C. Weiss, C. Mitterer,*  
manuscript in final preparation.
  
- II. Formation mechanisms of low-friction tribo-layers on arc-evaporated  $\text{TiC}_{1-x}\text{N}_x$  hard coatings,  
*M. Rebelo de Figueiredo, J. Neidhardt, R. Kaindl, A. Reiter, R. Tessadri, C. Mitterer,*  
*Wear* **265(3–4)**, 525–532 (2008).
  
- III. Low-friction mechanisms active for carbon containing coatings: Ti-C-N as a model system,  
*M. Rebelo de Figueiredo, J. Neidhardt, R. Franz and C. Mitterer,*  
in: Berg- und Hüttenmännische Monatshefte : BHM **153(7)** 263–267 (2008).
  
- IV. In situ studies of  $\text{TiC}_{1-x}\text{N}_x$  hard coating tribology,  
*M. Rebelo de Figueiredo, C. Muratore, R. Franz, R.R. Chromik, K.J. Wahl, A.A. Voevodin, M. O’Sullivan, M. Lechthaler, C. Mitterer,*  
*Tribology Letters* **40(3)** 365–373 (2010).

## 3.2 List of related publications

- VI. Abrasive and adhesive wear behavior of arc-evaporated  $\text{Al}_{1-x}\text{Cr}_x\text{N}$  hard coatings,  
*A.E. Reiter, C. Mitterer, M. Rebelo de Figueiredo, R. Franz,*  
*Tribology Letters* **37(3)** 605–611 (2010).
  
- VII. Structure-property relations in ZrCN coatings for tribological applications,  
*E. Silva, M. Rebelo de Figueiredo, R. Franz, R. Escobar Galindo, C. Palacio, A. Espinosa, S. Calderon V., C. Mitterer, S. Carvalho,*  
*Surface and Coatings Technology* **205** 2134–2141 (2010).

### 3.3 My contribution to included publications

	Conception and planning <sup>1</sup>	Experiments	Analysis and interpretation	Manuscript preparation <sup>1</sup>
Publication I	100	100	100	100
Publication II	100	80	90	100
Publication III	100	90	100	100
Publication IV	80	30	50	70

---

<sup>1</sup>Supervision not included

# Publication I

**Analysis of energy and mass fluxes during deposition  
of TiCN hard coatings by cathodic arc evaporation**

**M. Rebelo de Figueiredo, R. Franz, C. Weiss, C. Mitterer**

manuscript in final preparation



# Analysis of energy and mass fluxes during deposition of TiCN hard coatings by cathodic arc evaporation

M. Rebelo de Figueiredo<sup>1</sup>, R. Franz<sup>1</sup>, C. Weiss<sup>2</sup>, C. Mitterer<sup>1</sup>

*1 Christian Doppler Laboratory for Advanced Hard Coatings at the Department of Physical Metallurgy and Materials Testing, Montanuniversität Leoben, Franz-Josef-Strasse 18, A-8700 Leoben, Austria*

*2 Institute of Process Engineering and Industrial Environmental Protection, Montanuniversität Leoben, Franz-Josef-Strasse 18, A-8700 Leoben, Austria*

Within the present work, an evaluation concept for performing a mass and energy balance of a physical vapor deposition process was developed. The concept is exemplified on the deposition of a TiCN hard coating on drills by cathodic arc evaporation. A quantification of the resources needed for each process step during the deposition of TiCN has been performed and the obtained data for the mass and energy flows are displayed as Sankey diagrams which allow for a direct visualization of the major transfers during the deposition process.

## 1 Introduction

Hard coatings have been introduced to the market with the major goal of reducing the wear of cutting and forming tools during operation. The main driving force for manufacturers of tools and coatings is to enhance the productivity, that is to increase the lifetime of the tool and most importantly its performance, meaning that an increased cutting speed has a high impact in the reduction of manufacturing costs [1].

TiCN has been commercialized in the middle of the 1980-ies and has proven to be a successful protective coating material. Its tribological properties under room temperature and ambient air conditions are highly attractive since the coefficient of friction is rather low ranging from 0.14 to 0.20 [2–4]. TiCN also presents high hardness which, depending on the C content incorporated in the coating, is in the range of 25 to 45 GPa [3, 5]. This coating system is therefore widely used in the tool industry for milling and threading applications [5]. Most of the TiCN coatings commercially available possess an optimized architecture for specific applications, e.g. it is common to synthesize TiCN with a compositional gradient in the C content within the  $\text{TiC}_{1-x}\text{N}_x$  solid solution [6].

One of the physical vapor deposition (PVD) techniques frequently used to deposit TiCN is cathodic arc evaporation (CAE), but only limited information is available regarding details of material and energy usage for such processes. The objective of the present work was therefore to perform a mass and energy balance during a PVD process utilizing CAE for coating synthesis and in this way to quantify the resources needed to deposit a TiCN coating on tools like drills. The coating analyzed here is a TiCN model coating, representing a homogeneous composition which is usually not commercially available. The methodology applied within this work is intended to demonstrate a possible strategy to evaluate PVD processes which can be adapted in the future for analyzing other coating systems and other deposition techniques.

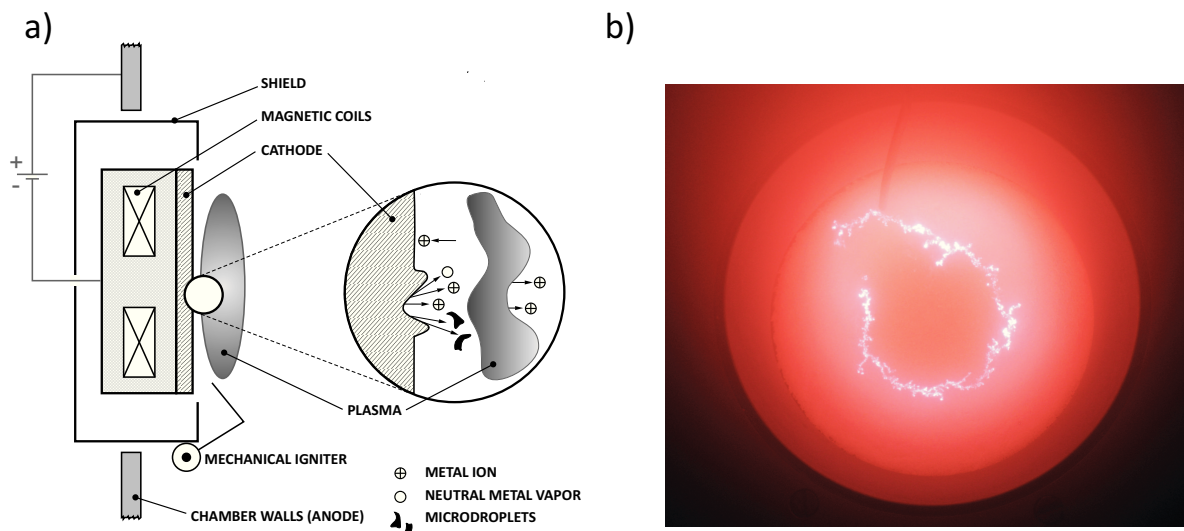


Figure 1: Cathodic arc evaporation: a) basic principle modified after [7]; b) still of a typical arc on a target surface in  $N_2$  atmosphere.

## 2 Cathodic arc evaporation

### 2.1 Basic principle

The technique of cathodic arc evaporation employs a vacuum arc, which is a high current (30 A to some kA), low voltage (20 to 100 V) electrical discharge between two electrodes positioned in a vacuum environment to generate vapor emission from a source material target (cathode) as schematically represented in Figure 1a. The arc is commonly initiated by a short contact between the cathode and a metal trigger finger. The current is concentrated in a small luminous area in the  $\mu m^2$  range and it is named cathode spot or arc spot. This spot has a very high current density ranging from  $10^6$  to  $10^{12}$   $A \cdot m^{-2}$ , it moves over the cathode surface with a velocity of  $100 \text{ m} \cdot s^{-1}$ , the ignition and explosion of the spot takes 1–10 ns and its residence time is of the order of 100 ns [7–9]. A picture of a typical arc on a cathode surface is shown in Figure 1b. The main advantage of arc evaporation lies in the high percentage of ions in the emitted flux (10–100%) and the high kinetic energy of these ions (10–150 eV), enhancing adhesion, increasing film packing density and enabling high deposition rates [10]. However, besides ions and neutrals, macroparticles or microdroplets are also produced. These macroparticles are non-vaporised particles ejected from the cathode with a size that varies from 0.01 to  $10 \mu m$  and their incorporation into growing films causes growth defects. Such features can limit the usage of CAE for depositing films, where optical properties and electrical conductivity are important [9, 11], but are tolerable for the majority of hard coatings used in tooling applications.

Although the cathode material needs to be conductive, there is a wide range of materials that can be deposited by arc evaporation and besides metal coatings, compound films can also be synthesized by reactive deposition using  $N_2$ ,  $O_2$ ,  $C_2H_2$  or  $CH_4$ . The resulting coatings can be poorly conductive or even insulating like oxides (e.g.  $Al_2O_3$ ,  $ZrO_2$ ), nitrides (e.g. TiAlN, CrAlN), carbides (e.g. TiC, WC) and carbonitrides (e.g. TiCN, ZrCN) [7].

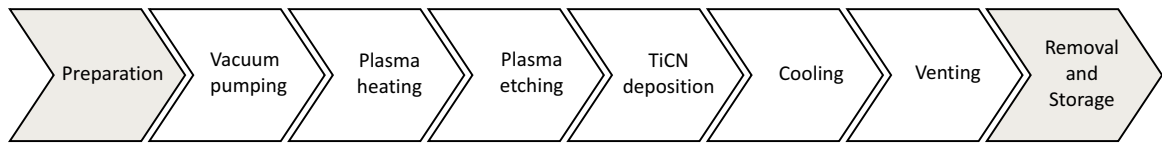


Figure 2: Sequential steps of an arc evaporation process.

## 2.2 Synthesis of TiCN

The TiCN analysed within the current work was prepared by reactive cathodic arc evaporation of Ti targets in an industrial scale arc evaporation plant (Oerlikon Balzers INNOVA) with a chamber volume of 1000 l. The coating was deposited at 450 °C and has a homogeneous composition [4]. The C<sub>2</sub>H<sub>2</sub> and Ar flows were kept constant at 100 sccm and 700 sccm whereas the N<sub>2</sub> flow was backfilled to a total pressure of  $3 \times 10^{-2}$  mbar as controlled by a capacitive gauge. During deposition the arc current of each of the 4 sources used was set to 180 A and a bias voltage of -100 V was applied to the carousel loaded with the drills to be coated.

## 3 Description of the process steps

Figure 2 shows a chronological sequence of the steps present during an industrial arc evaporation deposition process (see schematic in Figure 3) to synthesize TiCN. Details of each step are as follows.

**Preparation:** The drills to be coated with TiCN were cleaned in an ultrasonic bath filled with ethanol and then mounted on the substrate carousel (No. 9 in Figure 3) using appropriate sample holders that allow for a threefold rotation of the drills during deposition and, hence, uniform coating thickness. Subsequently, the carousel was placed inside the deposition chamber with the help of a transporter. The Ti targets were weighed prior to installation in the deposition system. Magnet systems were installed in the 4 arc sources used (No. 1 in Figure 3) to provide a magnetic field, which allows for steering the cathode spot during deposition ensuring an optimal target material utilization. Finally, the door of the chamber was closed after cleaning the sealing with ethanol. The time for the Preparation step is estimated to be 95 minutes. It has to be noted that within this study in total only 3 drills were coated, but for the industrial process 800 drills were considered. The carousel was therefore mainly filled with dummy substrates as replacement for the drills. However, cleaning and mounting of 800 drills takes a significantly higher amount of time even though automated cleaning lines with multi-stage ultrasonic baths are commonly applied during the cleaning step.

**Vacuum pumping:** At the beginning of this step, substrate heating by heat radiation (No. 2 in Figure 3) and carousel rotation were initiated. The main task of this step is, however, to evacuate the chamber. First, roots and rotary vane pump (No. 4 and 5 in Figure 3) reduce the pressure from atmospheric down to  $5 \times 10^{-1}$  mbar. At this point the turbomolecular

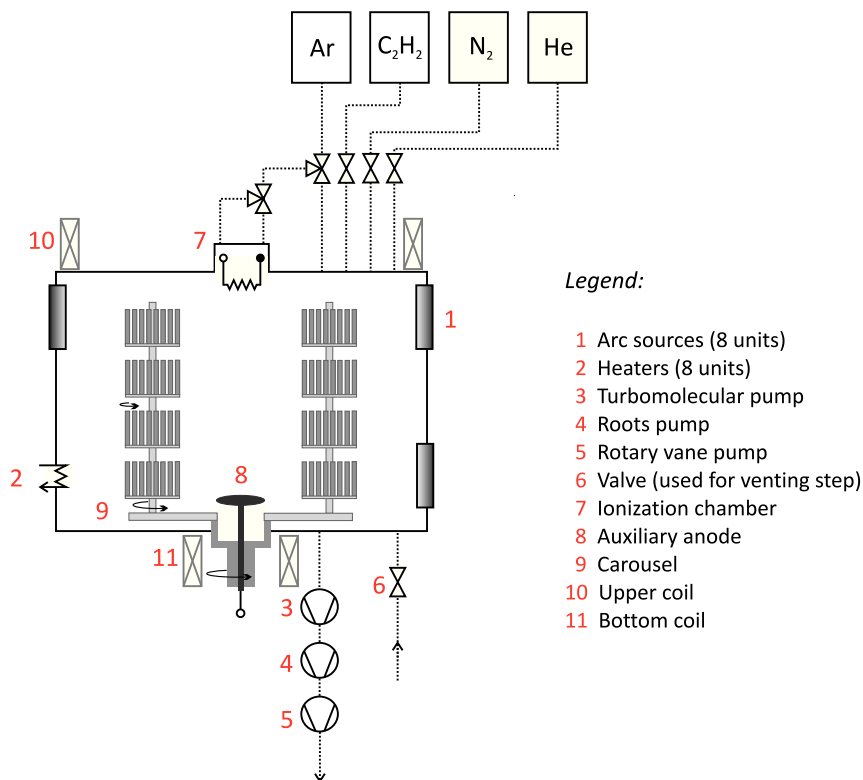


Figure 3: Schematic of the Oerlikon Balzers INNOVA arc evaporation deposition plant.

pump (No. 3 in Figure 3) is activated and the step ends after  $\sim 5$  min when a pressure of  $7.5 \times 10^{-3}$  mbar is reached.

**Plasma heating:** When the pressure was low enough ( $7.5 \times 10^{-3}$  mbar), Ar was inserted in the ionization chamber (No. 7 in Figure 3) and a current was applied to the filament in order to ionize the Ar atoms. The formed plasma was utilized as heating arc while the carousel served as anode. Concentrating the plasma in different regions of the carousel was achieved with the aid of upper and bottom coils (No. 10 and 11 in Figure 3) which provided for additional substrate heating until the aimed temperature of  $500^\circ\text{C}$  was reached. The total duration of this step was 32.5 minutes and at the end, heating arc, filament current, coils and Ar flow were turned off.

**Plasma etching:** Substrate heating by heat radiation was continued during the entire step. After the set of pumps reduced the pressure to  $5 \times 10^{-4}$  mbar, Ar was again inserted into the ionization chamber. Similar to the previous step, a plasma was established by applying a current to the filament. This time, however, the plasma current was directed to the auxiliary anode (No. 8 in Figure 3) forming the etching arc. Upper and bottom coils were used to control the spatial extension of the plasma whereas a negative bias voltage was applied to the substrate carousel to attract ions from the plasma. These ions provided for etching of the drills by sputtering their surface for 31.5 min. At the end of this step, etching arc, filament current, bias voltage, coils and Ar flow were turned off.



**TiCN deposition:** A short pumping step down to  $5 \times 10^{-4}$  mbar preceded the insertion of the gases needed for coating deposition,  $N_2$ ,  $C_2H_2$  and Ar. The latter is used for stabilization of the plasma and assistance in the ignition of new emission centers on the arc cathode allowing also for an efficient material use [9, 11]. A current was applied to the magnet systems on the back of the targets and the ignition of the cathodic arc plasma occurred via a short contact between the cathode (Ti target) and a trigger finger, followed by continuous evaporation of cathode material. A negative bias voltage was applied to the substrates to attract positive ions (Ti, N and C) and the subsequent condensation of ions and atoms from the plasma onto the substrates provided for the film growth where Ti reacted with C and N to form TiCN. The total deposition time was approximately 80 min which corresponded to a coating thickness on the drills of about  $2.5 \mu\text{m}$ . The substrate temperature during deposition was  $450 \text{ }^\circ\text{C}$  and it was controlled by regulating the radiation heaters. At the end of this step, cathodic arc plasma, magnet system current, gases and bias voltage were turned off as well as radiation heating.

**Cooling:** In order to facilitate the energy transfer between the carousel and the water-cooled chamber walls which reduces the cooling time, 50 mbar of He was inserted into the chamber. The final cooling temperature of  $200 \text{ }^\circ\text{C}$  was reached after 47.5 min and at the end of this step, the carousel rotation was turned off and the chamber was evacuated. At this point optional tests regarding the pumping speed and leak rate can be performed, but were not considered within this work.

**Venting:** In the Venting step, the air inlet valve (No. 6 in Figure 3) was opened to establish atmospheric pressure in order to be able to open the chamber door. This step lasted around 5 minutes.

**Removal and Storage:** After opening the chamber, the loaded carousel is removed from the deposition plant and the coated drills are dismounted. The Ti targets are also removed and the deposition chamber is cleaned from residual coating material that delaminated from the chamber walls and unused parts of the carousel.

## 4 Methodology

Within this study, a measurement concept was developed to determine the electrical energy and mass consumption for each CAE operation step, leaving the Preparation and Removal and Storage steps aside since they are not part of the actual deposition process. A full batch was considered, that is, the carousel is loaded with 800 drills. The deposition process cycle has a total duration of 3 h 26.5 min ( $3.442 \text{ h} = 12390 \text{ sec}$ ).

The quantification of the mass (solids and gases) and energy fluxes was performed based on the data recorded during a full deposition cycle. In Figure 4 and Figure 5, these results are presented in the form of Sankey diagrams [12] allowing for a direct visualization of the major transfers or flows within the deposition process.

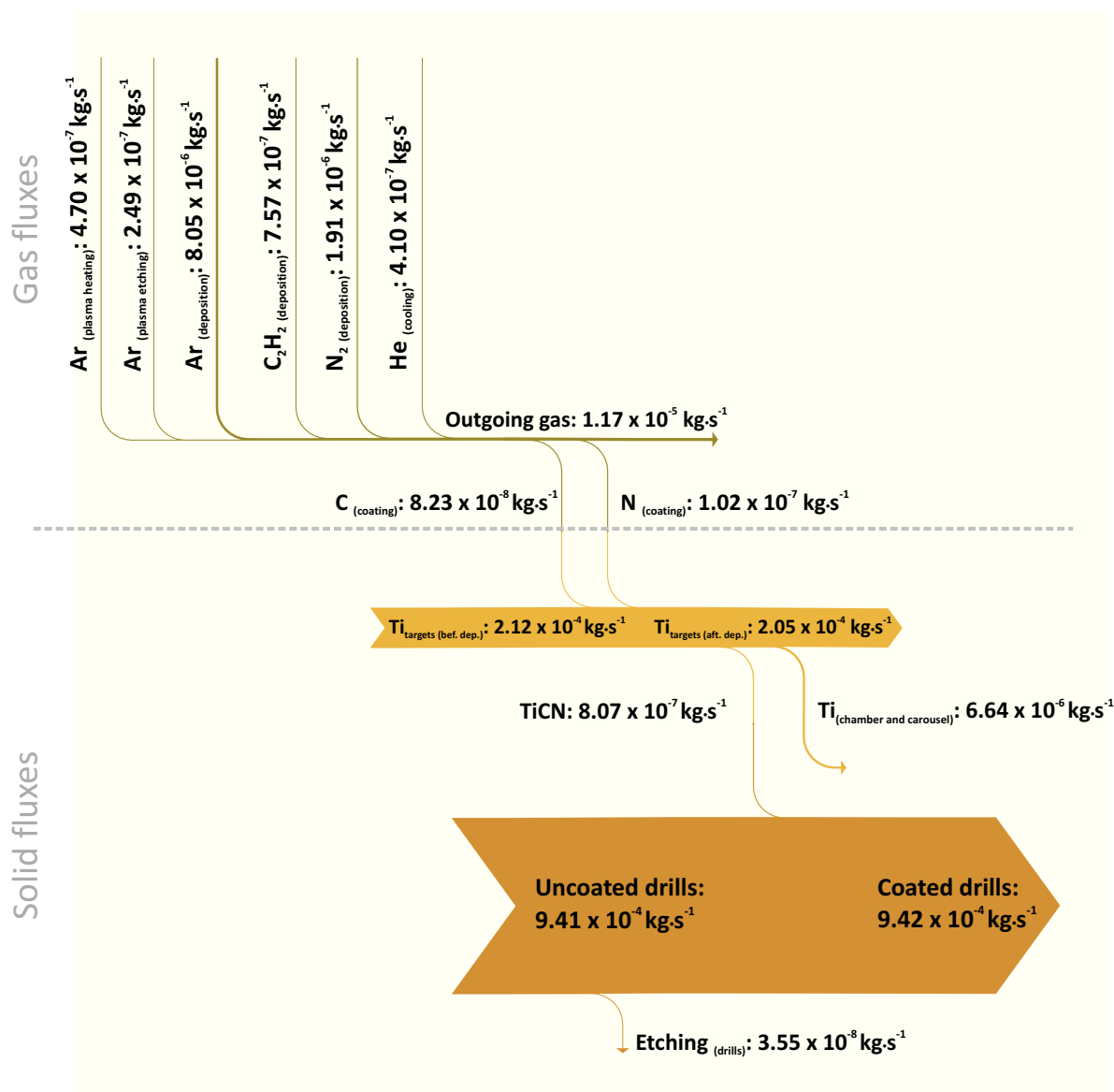


Figure 4: Sankey diagram of the mass fluxes involved in the coating process of 800 drills. Mass fluxes are quantified in kg per sec.

### 4.1 Mass balance

Figure 4 gives an overview of the gaseous and solid materials involved during a complete deposition cycle of TiCN. From the direct observation of the gas fluxes in the Sankey diagram it is possible to observe that the main gas contribution in the deposition process comes from Ar ( $8.05 \times 10^{-6} \text{ kg}\cdot\text{s}^{-1}$ ) although it is not incorporated in the coating. In fact, the majority of the gases in the chamber are going to be pumped out (outgoing gas:  $1.17 \times 10^{-5} \text{ kg}\cdot\text{s}^{-1}$ ). From the C and N atoms inserted via the gases C<sub>2</sub>H<sub>2</sub> and N<sub>2</sub>, a fraction of 12% ( $8.23 \times 10^{-8} \text{ kg}\cdot\text{s}^{-1}$ ) and 5% ( $1.02 \times 10^{-7} \text{ kg}\cdot\text{s}^{-1}$ ), respectively, enter the solid fluxes as they are incorporated into the coating deposited on the drills. These values were calculated based on the chemical composition of the synthesized coating, Ti<sub>47.9</sub>C<sub>25.3</sub>N<sub>26.8</sub>, which was determined

by elastic recoil detection analysis. However, there is a certain amount of C and N that is incorporated into the coating on other parts of the carousel and the chamber walls. Since this amount cannot be quantified, because the chemical composition of the deposits formed there is unknown, this loss in C and N is included in the outgoing gas.

Looking at the solid fluxes section where the Ti targets are considered,  $7.0 \times 10^{-6} \text{ kg}\cdot\text{s}^{-1}$  of Ti was evaporated from the 4 targets used in the deposition process. From the amount of evaporated Ti material, 9% ( $6.2 \times 10^{-7} \text{ kg}\cdot\text{s}^{-1}$ ) is incorporated in the coating deposited on the 800 drills (see Figure 4 and appendix). It is important to point out that the coated area on the drill comprises only the drilling head and not the shank. The total area on the 800 drills that was coated is estimated to be  $1.90 \text{ m}^2$ . The remaining 91% ( $6.64 \times 10^{-6} \text{ kg}\cdot\text{s}^{-1}$ ) of Ti are going to be deposited on other parts of the carousel and the chamber walls, in the form of a deposit of unknown composition. In addition it is impractical to determine whether Ti atoms are pumped out of the chamber or not and the fraction of Ti not incorporated into the coating on the drills is therefore assumed to remain either on unused parts of the carousel or on the chamber walls.

Regarding the bottom section of Figure 4 were the uncoated and coated drills are taken into account, one can observe that the coating on the 800 drills weighs  $8.07 \times 10^{-7} \text{ kg}\cdot\text{s}^{-1}$ , with contributions of Ti from the targets and C and N from the gases. The mass loss during the etching step prior to the TiCN deposition of  $3.55 \times 10^{-8} \text{ kg}\cdot\text{s}^{-1}$  is less than 5% of the coating mass flux.

## 4.2 Energy balance

Figure 5 shows an overview of the energy needed during a complete deposition cycle and the values are therefore presented in kW ( $\text{kJ}\cdot\text{s}^{-1}$ ). The partition of the energy was made dividing the consumption in three main components of the deposition process: Pumping (7.95 kW), Heating and Etching (15.62 kW), and Arc evaporation (5.81 kW). Other general contributions than those considered in the following like the carousel rotation and computer control were not included since they are of minor influence.

In the Pumping component, the energy consumption of the roots, rotary vane and turbomolecular pump are included. All pumps are considered to run at full power during the deposition cycle, which results in an overestimation of their energy consumption. The rotary vane pump, however, is the constituent that has higher energy flux (5.45 kW, see Figure 5). In the Heating and Etching section, the energy fluxes needed by the heaters, heating arc, etching arc, bias during etching, filament and coils are shown, being the heaters the constituent with the highest energy consumption (11.80 kW). The component Heating and Etching in general needs the biggest share of the total energy flux (15.62 kW which corresponds to 53%), as compared to Pumping (27%) and Arc evaporation (20%). Finally, the Arc evaporation constituent contains the arc sources, magnet systems and bias voltage energy required during the deposition of the coating. The arc current applied to the sources in order to evaporate material from the Ti targets consumes the highest amount of energy (5.02 kW, see Figure 5).

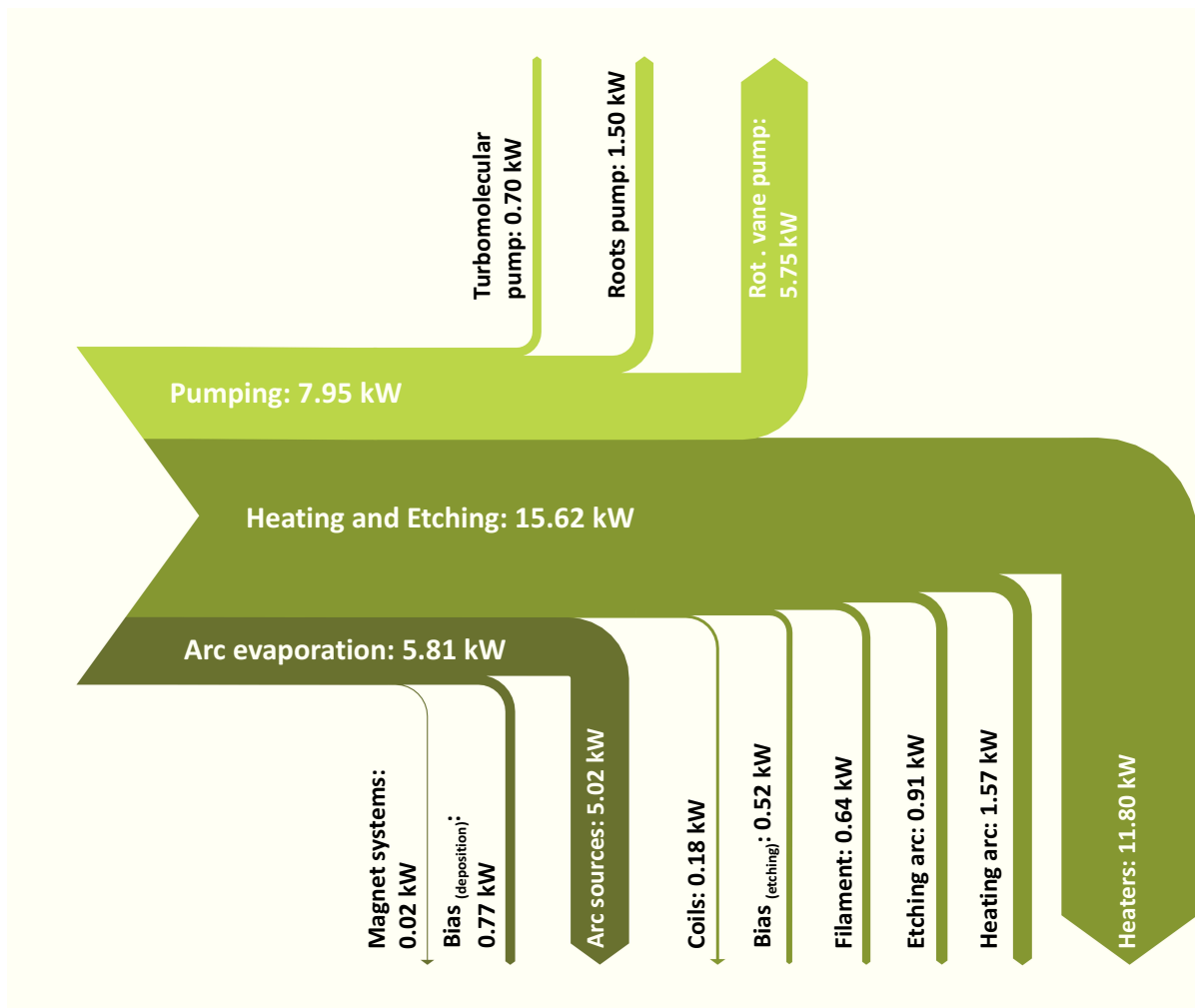


Figure 5: Sankey diagram of the energy fluxes involved in the coating process of 800 drills. Energy fluxes are quantified in kW.

## 5 Conclusion

In this study, a methodology was presented and put in practice to analyze the mass and energy fluxes during a process cycle to deposit a 2.5  $\mu\text{m}$  thick wear-resistant TiCN coating on drills by means of cathodic arc evaporation. The analysis of the mass fluxes present in the arc evaporation process revealed that 9% of the total evaporated material (Ti) of the target and a fraction of 12% C and 5% N of the  $\text{C}_2\text{H}_2$  and  $\text{N}_2$  gases inserted into the chamber is incorporated in the TiCN on the drills. On the other hand, the analysis of the energy fluxes showed that the component that consumes the most is the heating and etching of the drills (53% of the total energy), where the radiation heaters consume a fraction of almost 3/4.

## Acknowledgement

The financial support by the Christian Doppler Research Association within the framework of the Christian Doppler Laboratory for Advanced Hard Coatings with its partners PLANSEE

Composite Materials GmbH (Lechbruck, Germany) and OC Oerlikon Balzers AG (Balzers, Liechtenstein) is highly acknowledged.

## References

- [1] W. Kalss, A. Reiter, V. Derflinger, C. Gey, and J. L. Endrino, *Int. J. Refract. Met. Hard Mater.*, 2006, **24**, 399–404.
- [2] M. Rebelo de Figueiredo, J. Neidhardt, R. Kaindl, A. Reiter, R. Tessadri, and C. Mitterer, *Wear*, 2008, **265**, 525–532.
- [3] M. Rebelo de Figueiredo, C. Muratore, R. Franz, R. Chromik, K. Wahl, A. Voevodin, M. O’Sullivan, M. Lechthaler, and C. Mitterer, *Tribol. Lett.*, 2010, **40**, 365–373.
- [4] M. Rebelo de Figueiredo, J. Neidhardt, R. Franz, and C. Mitterer, *Berg- und Hüttenmännische Monatshefte*, 2008, **153**, 263–267.
- [5] L. Karlsson, L. Hultman, M. P. Johansson, J. E. Sundgren, and H. Ljungcrantz, *Surf. Coat. Technol.*, 2000, **126**, 1–14.
- [6] J. Vetter, *Surf. Coat. Technol.*, 1995, **76-77**, 719–724.
- [7] M. Ohring, *The Materials Science of Thin Films - Deposition and Structure, 2nd edition*, Academic Press, San Diego, 2002.
- [8] J. L. Vossen and W. Kern, *Thin film processes II*, Academic Press, San Diego, 1991.
- [9] U. Helmersson, M. Lattemann, J. Bohlmark, A. P. Ehiasarian, and J. T. Gudmundsson, *Thin Solid Films*, 2006, **513**, 1–24.
- [10] R. L. Boxman, P. J. Martin, and D. M. Sanders, *Handbook of Vacuum Arc Science and Technology*, Noyes Publications, New Jersey, 1995.
- [11] A. Anders, *Cathodic Arcs - from Fractal Spots to Energetic Condensation*, Springer Science + Business Media, LLC, New York, 2008.
- [12] M. Schmidt, *Journal of Industrial Ecology*, 2008, **12**, 173–185.

## Appendix - Methodology

In the following sections, the values marked in **bold** are represented in the mass and energy Sankey diagrams.

### 1 Mass fluxes

#### 1.1 Calculation of the gas fluxes

For the calculation of the mass of gases needed for the process, the following calculations were performed based on the data available. The calculation of the mass of Ar needed for the process step Plasma heating serves as an example.

The step has a duration of 32.5 min, and a flow of 100 sccm of Ar is inserted into the chamber during this time. The flow is multiplied by the duration of the step resulting in a determined normal volume  $V_N$ . The latter is then multiplied by the density  $d$  of Ar, which gives the mass of Ar present in this step.

**Ar<sub>(plasma heating)</sub>**: 100 sccm Ar; Step time = 32.5 min;  $d$  (Ar<sub>1.0133 bar, 0°C</sub>) = 1.784 kg·m<sup>-3</sup>

$$\Rightarrow V_N = 100 \times 10^{-6} \text{ mm}^3 \cdot \text{min}^{-1} \times 32.5 \text{ min} = 0.00325 \text{ m}^3$$

$$\Rightarrow \text{mass Ar}_{(\text{plasma heating})} = V_N \times d \Leftrightarrow$$

$$\Leftrightarrow \text{mass Ar}_{(\text{plasma heating})} = 0.00325 \text{ m}^3 \times 1.784 \text{ kg} \cdot \text{m}^{-3} = 0.00580 \text{ kg}$$

Dividing by the total time that the process takes, 3.442 h = 12390 s,

$$\text{mass flux Ar}_{(\text{plasma heating})} = 0.00580 \text{ kg} / 12390 \text{ s} = \mathbf{4.70 \times 10^{-7} \text{ kg} \cdot \text{s}^{-1}}$$

The same methodology was used to calculate the mass of Ar<sub>(plasma etching)</sub> (55 sccm Ar for 31.5 min), Ar<sub>(deposition)</sub> (700 sccm Ar for 80 min), C<sub>2</sub>H<sub>2</sub> (deposition) (100 sccm C<sub>2</sub>H<sub>2</sub> for 80 min), N<sub>2</sub> (deposition) (236 sccm N<sub>2</sub> for 80 min). For He<sub>(cooling)</sub> the methodology used was slightly different, since information about the pressure  $p$  is provided and not the flow. In this case,

**He<sub>(cooling)</sub>**: pressure:  $p = 50 \text{ mbar}$ ; molar mass,  $M$  (He) = 4.00 g·mol<sup>-1</sup>;  
density:  $d$  (He<sub>1.0133 bar, 0°C</sub>) = 0.1786 kg·m<sup>-3</sup>; final cooling temperature:  $T = 473.15 \text{ K}$ ;  
chamber volume:  $V = 1000 \text{ l}$ ; gas constant:  $R = 8314.47 \text{ J} \cdot \text{mol}^{-1} \cdot \text{K}^{-1}$

$$\Rightarrow p \times V = n(\text{He}) \times R \times T \Leftrightarrow$$

$$\Leftrightarrow n(\text{He}) = (5000 \text{ Pa} \times 1000 \text{ l}) / (8314.47 \text{ l} \cdot \text{Pa} \cdot \text{mol}^{-1} \cdot \text{K}^{-1} \times 473.15 \text{ K}) = 1.271 \text{ mol}$$

$$\begin{aligned} \Rightarrow \text{mass He}_{(\text{cooling})} &= n(\text{He}) \times M(\text{He}) = 1.271 \text{ mol} \times 4.00 \text{ g} \cdot \text{mol}^{-1} \\ &= 5.084 \text{ g} = 5.08 \times 10^{-3} \text{ kg} \end{aligned}$$

$$\text{mass flux He}_{(\text{cooling})} = 5.08 \times 10^{-3} \text{ kg} / 12390 \text{ s} = \mathbf{4.10 \times 10^{-7} \text{ kg} \cdot \text{s}^{-1}}$$

## 1.2 Calculation of the mass of C and N incorporated in the TiCN coating

The composition analysis of the coating performed by elastic recoil detection analysis revealed the following composition:



This has to be transformed to wt.%,

$$\begin{aligned} \text{Atomic mass } M(\text{Ti}) &= 47.867 \text{ amu} \rightarrow 47.9 \times M(\text{Ti}) = 47.9 \times 47.867 \text{ amu} = 2292.8 \text{ amu} \\ \text{Ti} &\Rightarrow 2292.8 \text{ amu} / 2972.03 \text{ amu} = 0.7714 = 77.14 \text{ wt.}\% \end{aligned}$$

$$\begin{aligned} \text{Atomic mass } M(\text{C}) &= 12.01 \text{ amu} \rightarrow 25.3 \times M(\text{C}) = 25.3 \times 12.01 \text{ amu} = 303.85 \text{ amu} \\ \text{C} &\Rightarrow 303.85 \text{ amu} / 2972.03 \text{ amu} = 0.1022 = 10.22 \text{ wt.}\% \end{aligned}$$

$$\begin{aligned} \text{Atomic mass } M(\text{N}) &= 14.01 \text{ amu} \rightarrow 26.8 \times M(\text{N}) = 26.8 \times 14.01 \text{ amu} = 375.38 \text{ amu} \\ \text{N} &\Rightarrow 375.38 \text{ amu} / 2972.03 \text{ amu} = 0.1263 = 12.63 \text{ wt.}\% \end{aligned}$$

$$\Rightarrow \text{Total mass} = 2292.8 \text{ amu} + 303.85 \text{ amu} + 375.38 \text{ amu} = 2972.03 \text{ amu}$$

To go further with the calculation, information about the mass of the deposited TiCN coating is needed. Therefore, 3 drills were weighed before and after deposition, having in account the loss of material during etching (presented later on). The 3 values obtained were averaged. Giving that the mass of TiCN coating on one drill weighs 12.51 mg, by extrapolation for 800 drills we have:

$$\Rightarrow \text{mass TiCN}_{(800 \text{ drills})} = 12.51 \times 10^{-6} \text{ kg} \times 800 = 10.01 \text{ g} = 1.00 \times 10^{-2} \text{ kg}$$

$$\text{mass flux TiCN}_{(800 \text{ drills})} = 1.00 \times 10^{-2} \text{ kg} / 12390 \text{ s} = \mathbf{8.07 \times 10^{-7} \text{ kg}\cdot\text{s}^{-1}}$$

The mass of C and N present in the coating is then calculated by multiplying the mass of TiCN on the drills by the weight percentage derived from the chemical composition.

$$\Rightarrow \text{mass Ti}_{(800 \text{ drills})} = 10.01 \text{ g} \times 0.7714 = 7.72 \text{ g} = 7.72 \times 10^{-3} \text{ kg}$$

$$\Rightarrow \text{mass C}_{(800 \text{ drills})} = 10.01 \text{ g} \times 0.1022 = 1.02 \text{ g} = 1.02 \times 10^{-3} \text{ kg}$$

$$\text{mass flux C}_{(800 \text{ drills})} = 1.02 \times 10^{-3} \text{ kg} / 12390 \text{ s} = \mathbf{8.23 \times 10^{-8} \text{ kg}\cdot\text{s}^{-1}}$$

$$\Rightarrow \text{mass N}_{(800 \text{ drills})} = 10.01 \times 0.1263 = 1.26 \text{ g} = 1.26 \times 10^{-3} \text{ kg}$$

$$\text{mass flux N}_{(800 \text{ drills})} = 1.26 \times 10^{-3} \text{ kg} / 12390 \text{ s} = \mathbf{1.02 \times 10^{-7} \text{ kg}\cdot\text{s}^{-1}}$$

### 1.3 Calculation of the mass of Ti evaporated from the targets

The 4 Ti targets used in the deposition process were weighed before and after the deposition,

$$\Rightarrow \text{mass Ti}_{\text{targets (before deposition)}} = (644 + 685 + 643 + 657) \times 10^{-3} \text{ kg} = 2.63 \text{ kg}$$

$$\text{mass flux Ti}_{\text{targets (before deposition)}} = 2.63 \text{ kg} / 12390 \text{ s} = \mathbf{2.12 \times 10^{-4} \text{ kg}\cdot\text{s}^{-1}}$$

$$\Rightarrow \text{mass Ti}_{\text{targets (after deposition)}} = (623 + 662 + 621 + 636) \times 10^{-3} \text{ kg} = 2.54 \text{ kg}$$

$$\text{mass flux Ti}_{\text{targets (after deposition)}} = 2.54 \text{ kg} / 12390 \text{ s} = \mathbf{2.05 \times 10^{-4} \text{ kg}\cdot\text{s}^{-1}}$$

The difference between the weight of the Ti targets before and after deposition is the total mass of evaporated material, which is 0.090 kg. Based on the chemical composition of the coating mentioned above, the mass of Ti present in the TiCN coating on the 800 drills is

$7.72 \times 10^{-3}$  kg. The subtraction of the total mass of evaporated Ti by the mass of Ti incorporated in the coating on the 800 drills gives the mass of Ti lost, that is, the mass of Ti deposited in some form on the carousel and chamber walls.

$$\begin{aligned} \Rightarrow \text{mass Ti}_{(\text{chamber and carousel})} &= \text{mass Ti}_{(\text{total evaporated})} - \text{mass Ti}_{(800 \text{ drills})} \\ &= 0.090 \text{ kg} - 7.72 \times 10^{-3} \text{ kg} = 8.23 \times 10^{-2} \text{ kg} \end{aligned}$$

$$\text{mass flux Ti}_{(\text{chamber and carousel})} = 8.23 \times 10^{-2} \text{ kg} / 12390 \text{ s} = \mathbf{6.64 \times 10^{-6} \text{ kg}\cdot\text{s}^{-1}}$$

## 1.4 Coated and uncoated drills

Before deposition, 6 drills were weighed and their averaged value is:

$$\Rightarrow \text{mass}_{(1 \text{ uncoated drill})} = 14.5832 \text{ g}$$

Extrapolating the value to 800 drills gives:

$$\Rightarrow \text{mass}_{(800 \text{ uncoated drills})} = 14.5832 \text{ g} \times 800 = 11667 \text{ g} = 11.667 \text{ kg}$$

$$\text{mass flux}_{(800 \text{ uncoated drills})} = 11.667 \text{ kg} / 12390 \text{ s} = \mathbf{9.41 \times 10^{-4} \text{ kg}\cdot\text{s}^{-1}}$$

The mass of the 800 coated drills is calculated adding the mass of TiCN coating to the mass of the 800 uncoated drills, that is,

$$\begin{aligned} \Rightarrow \text{mass}_{(800 \text{ coated drills})} &= \text{mass}_{(800 \text{ uncoated drills})} - \text{mass}_{\text{etched material (800 uncoated drills)}} \\ &\quad + \text{mass TiCN}_{(800 \text{ drills})} \\ &= 11.667 \text{ kg} - 4.4 \times 10^{-4} \text{ kg} + 10.01 \times 10^{-3} \text{ kg} \\ &= 11.677 \text{ kg} \end{aligned}$$

$$\text{mass flux}_{(800 \text{ coated drills})} = 11.677 \text{ kg} / 12390 \text{ s} = \mathbf{9.42 \times 10^{-4} \text{ kg}\cdot\text{s}^{-1}}$$

## 1.5 Material loss from the drills by etching

The material loss of the drills was calculated by weighing 3 drills before and after the etching process. The value is an averaged value for the material loss of a drill:

$$\Rightarrow \text{mass}_{\text{etched material (1 drill uncoated)}} = 0.00055 \text{ g}$$

Extrapolating this value to 800 drills, the mass loss is:

$$\Rightarrow \text{mass}_{\text{etched material (800 drills)}} = 0.00055 \text{ g} \times 800 = 0.44 \text{ g} = 4.4 \times 10^{-4} \text{ kg}$$

$$\text{mass flux}_{\text{etched material (800 drills)}} = 4.4 \times 10^{-4} \text{ kg} / 12390 \text{ s} = \mathbf{3.55 \times 10^{-8} \text{ kg}\cdot\text{s}^{-1}}$$



## 2 Energy fluxes

For the energy fluxes, the consumption was divided in three sections: “Pumping”, “Heating and Etching” and “Arc evaporation”.

### 2.1 Pumping

The calculation of the energy consumption for the Pumping section was made in the following mode: the power of each pump, the turbomolecular, roots and rotary vane pump, was multiplied by the duration of each sequential step. In this way, it is assumed that all pumps run at full power during the process resulting in an overestimation of their energy consumption. The calculation made for the Vacuum pumping step will serve as example.

**Vacuum pumping** step: Time = 5 min = 300 s

$$\begin{aligned} \Rightarrow E_{(\text{turbomolecular pump} - \text{vacuum pumping})}: & 700 \text{ W (100\%)} = 700 \text{ J}\cdot\text{s}^{-1} \\ & \rightarrow 700 \text{ J}\cdot\text{s}^{-1} \times 300 \text{ s} = 2.10 \times 10^5 \text{ J} = 210 \text{ kJ} \end{aligned}$$

$$\begin{aligned} \Rightarrow E_{(\text{roots pump} - \text{vacuum pumping})}: & 1.5 \text{ kW (100\%)} = 1500 \text{ J}\cdot\text{s}^{-1} \\ & \rightarrow 1500 \text{ J}\cdot\text{s}^{-1} \times 300 \text{ s} = 4.50 \times 10^5 \text{ J} = 450 \text{ kJ} \end{aligned}$$

$$\begin{aligned} \Rightarrow E_{(\text{rotary vane pump} - \text{vacuum pumping})}: & 5.75 \text{ kW (100\%)} = 5750 \text{ J}\cdot\text{s}^{-1} \\ & \rightarrow 5750 \text{ J}\cdot\text{s}^{-1} \times 300 \text{ s} = 1.72 \times 10^6 \text{ J} = 1720 \text{ kJ} \end{aligned}$$

The total consumption of energy of the “Pumping” section is given by the sum of the energy utilization by each pump for each step, that is, 98528 kJ. Dividing the energy by the total time of the process, 12390 s:

$$\text{Energy flux}_{(\text{Pumping})} = 98528 \text{ kJ} / 12390 \text{ s} = \mathbf{7.95 \text{ kW}}$$

### 2.2 Heating and Etching

#### 2.2.1 Heaters

The calculation of the energy needed for the radiation heaters was done in a similar way as for the pumps. First, it was assumed that all 8 heaters run at full power during the process (except for “Cooling” and “Venting” steps). Each heater has a power of 4 kW and an active time of 149 min (8940 s), therefore:

$$\Rightarrow E_{(\text{heaters})} = 8 \times 4 \text{ kW} \times 8940 \text{ s} = 286080 \text{ kJ}$$

This value is an overestimation of the energy consumption. According to the available data, the 4 heaters in the upper level have an effective working time of 53.1% and the 4 heaters in the lower level of 49.1%. This results in a corrected energy of:

$$\Rightarrow \text{Heaters upper level (286080 kJ / 2)} \rightarrow 143040 \text{ kJ} \times 0.531 = 75954 \text{ kJ}$$

$$\Rightarrow \text{Heaters lower level (286080 kJ / 2)} \rightarrow 143040 \text{ kJ} \times 0.491 = 70233 \text{ kJ}$$

The total consumption is then given by the sum of both contributions, that is:

$$\Rightarrow E_{(\text{heaters})} = E_{(\text{heaters upper level})} + E_{(\text{heaters lower level})} = 75954 \text{ kJ} + 70233 \text{ kJ} = 146187 \text{ kJ}$$

$$\text{Energy flux}_{(\text{heaters})} = 146187 \text{ kJ} / 12390 \text{ s} = \mathbf{11.80 \text{ kW}}$$

### 2.2.2 Heating arc

The calculation of the energy needed for the heating arc was done by multiplying the current and the voltage to obtain the power. A multiplication with the active time gives the energy consumption:

$$\text{Time} = 32.5 \text{ min} = 1950 \text{ s}$$

$$\Rightarrow E_{(\text{heating arc})}: 250 \text{ A} \times 40 \text{ V} = 10000 \text{ W} = 10000 \text{ J}\cdot\text{s}^{-1}$$

$$\rightarrow 10000 \text{ J}\cdot\text{s}^{-1} \times 1950 \text{ s} = 1.95 \times 10^7 \text{ J} = 19500 \text{ kJ}$$

$$\text{Energy flux}_{(\text{heating arc})} = 19500 \text{ kJ} / 12390 \text{ s} = \mathbf{1.57 \text{ kW}}$$

### 2.2.3 Etching arc

The calculation of the energy needed for the etching arc was analogous to the heating arc:

$$\text{Time} = 31.5 \text{ min} = 1890 \text{ s}$$

$$\Rightarrow E_{(\text{etching arc})}: 150 \text{ A} \times 40 \text{ V} = 6000 \text{ W} = 6000 \text{ J}\cdot\text{s}^{-1}$$

$$\rightarrow 6000 \text{ J}\cdot\text{s}^{-1} \times 1890 \text{ s} = 1.13 \times 10^7 \text{ J} = 11300 \text{ kJ}$$

$$\text{Energy flux}_{(\text{etching arc})} = 11300 \text{ kJ} / 12390 \text{ s} = \mathbf{0.91 \text{ kW}}$$

### 2.2.4 Filament

The calculation of the energy needed for the filament was done in a similar as above:

$$\text{Filament}_{(\text{plasma heating})}: 200 \text{ A} \rightarrow 11.3 \text{ V}; \text{ Time} = 27 \text{ min (1260 s)}$$

$$200 \text{ A} \times 11.3 \text{ V} \times 1260 \text{ s} = 3661200 \text{ J} = 3661 \text{ kJ}$$

$$\text{Filament}_{(\text{plasma etching})}: 200 \text{ A} \rightarrow 11.3 \text{ V}; \text{ Time} = 31.5 \text{ min (1890 s)}$$

$$200 \text{ A} \times 11.3 \text{ V} \times 1890 \text{ s} = 4271400 \text{ J} = 4271 \text{ kJ}$$

Since the filament is active in two steps, the total consumption is given by the sum of both contributions, that is:

$$\Rightarrow E_{(\text{filament})} = E_{(\text{filament-heating})} + E_{(\text{filament-etching})} = 3661 \text{ kJ} + 4271 \text{ kJ} = 7932 \text{ kJ}$$

$$\text{Energy flux}_{(\text{filament})} = 7932 \text{ kJ} / 12390 \text{ s} = \mathbf{0.64 \text{ kW}}$$

### 2.2.5 Bias<sub>(plasma etching)</sub>

The calculation of the energy needed for the bias during etching was done in a similar way as above:

$$\begin{aligned} \Rightarrow E_{\text{bias (plasma etching)}} &: 170 \text{ V} \times 20 \text{ A} = 3400 \text{ W} = 3400 \text{ J}\cdot\text{s}^{-1} \\ &\rightarrow 3400 \text{ J}\cdot\text{s}^{-1} \times 1890 \text{ s} = 6.43 \times 10^6 \text{ J} = 6430 \text{ kJ} \end{aligned}$$

$$\text{Energy flux}_{\text{bias (plasma etching)}} = 6430 \text{ kJ} / 12390 \text{ s} = \mathbf{0.52 \text{ kW}}$$

### 2.2.6 Coils

The coils are active during “Plasma heating” and “Plasma etching” steps. In case of “Plasma heating”, the current and the voltage are varied over time resulting in the following energies:

$$\begin{aligned} \text{Coils}_{\text{(plasma heating)}}: \text{ Upper coil} \Rightarrow \text{ a) } &4.4 \text{ A} \rightarrow 6.6 \text{ V}; \text{ Time} = 9 \times 1 \text{ min} \\ &\rightarrow 4.4 \text{ A} \times 6.6 \text{ V} \times 9 \times 60 \text{ s} = 15682 \text{ J} = 16 \text{ kJ} \end{aligned}$$

$$\begin{aligned} \text{b) } &20 \text{ A} \rightarrow 28.8 \text{ V}; \text{ Time} = 5 \times 2 \text{ min} \\ &\rightarrow 20 \text{ A} \times 28.8 \text{ V} \times 10 \times 60 \text{ s} = 345600 \text{ J} = 346 \text{ kJ} \end{aligned}$$

$$\begin{aligned} \text{Bottom coil} \Rightarrow &-6 \text{ A} \rightarrow 5.6 \text{ V}; \text{ Time} = 27 \text{ min} \\ &\rightarrow 6 \text{ A} \times 5.6 \text{ V} \times 27 \times 60 \text{ s} = 54432 \text{ J} = 54 \text{ kJ} \end{aligned}$$

$$\begin{aligned} \text{Coils}_{\text{(plasma etching)}}: \text{ Upper coil} \Rightarrow &20 \text{ A} \rightarrow 28.8 \text{ V}; \text{ Time} = 31.5 \text{ min} \\ &\rightarrow 20 \text{ A} \times 28.8 \text{ V} \times 31.5 \times 60 \text{ s} = 1088640 \text{ J} = 1089 \text{ kJ} \end{aligned}$$

$$\begin{aligned} \text{Bottom coil} \Rightarrow &20 \text{ A} \rightarrow 19 \text{ V}; \text{ Time} = 31.5 \text{ min} \\ &\rightarrow 20 \text{ A} \times 19 \text{ V} \times 31.5 \times 60 \text{ s} = 718200 \text{ J} = 718 \text{ kJ} \end{aligned}$$

The total consumption is then given by the sum of all contributions, that is:

$$\begin{aligned} \Rightarrow E_{\text{(coils)}} &= E_{\text{coils (plasma heating)}} + E_{\text{coils (plasma etching)}} \\ &= [(16 \text{ kJ} + 346 \text{ kJ}) + 54 \text{ kJ}] + [1089 \text{ kJ} + 718 \text{ kJ}] \\ &= 2223 \text{ kJ} \end{aligned}$$

$$\text{Energy flux}_{\text{(coils)}} = 2223 \text{ kJ} / 12390 \text{ s} = \mathbf{0.18 \text{ kW}}$$

## 2.3 Arc evaporation

In this section the energy consumption is also partitioned in three sections: Magnet systems, Bias and Arc sources. The calculation of the energy needed for the “Arc evaporation” section was done in a similar way as for the latter sections and it is shown below:

$$\text{Time} = 80 \text{ min} = 4800 \text{ s}$$

$$\begin{aligned} \Rightarrow E_{(\text{arc sources})}: & 180 \text{ A} \times 18 \text{ V} = 3240 \text{ W per source;} \\ & \underline{\text{For 4 sources:}} 12960 \text{ W} = 12960 \text{ J}\cdot\text{s}^{-1} \\ & \rightarrow 12960 \text{ J}\cdot\text{s}^{-1} \times 4800 \text{ s} = 6.22 \times 10^7 \text{ J} = 6.22 \times 10^4 \text{ kJ} \end{aligned}$$

$$\text{Energy flux}_{(\text{arc sources})} = 6.22 \times 10^4 \text{ kJ} / 12390 \text{ s} = \mathbf{5.02 \text{ kW}}$$

$$\begin{aligned} \Rightarrow E_{(\text{magnet systems})}: & 0.6 \text{ A} \times 18.5 \text{ V} = 11.1 \text{ W per source;} \\ & \underline{\text{For 4 sources:}} 44.4 \text{ W} = 44.4 \text{ J}\cdot\text{s}^{-1} \\ & \rightarrow 44.4 \text{ J}\cdot\text{s}^{-1} \times 4800 \text{ s} = 2.13 \times 10^5 \text{ J} = 213 \text{ kJ} \end{aligned}$$

$$\text{Energy flux}_{(\text{magnet systems})} = 213 \text{ kJ} / 12390 \text{ s} = \mathbf{0.02 \text{ kW}}$$

$$\begin{aligned} \Rightarrow E_{(\text{bias})}: & 100 \text{ V} \times 20 \text{ A} = 2000 \text{ W} = 2000 \text{ J}\cdot\text{s}^{-1} \text{ (for the carousel)} \\ & \rightarrow 2000 \text{ J}\cdot\text{s}^{-1} \times 4800 \text{ s} = 9.6 \times 10^6 \text{ J} = 9600 \text{ kJ} \end{aligned}$$

$$\text{Energy flux}_{(\text{bias})} = 9600 \text{ kJ} / 12390 \text{ s} = \mathbf{0.77 \text{ kW}}$$

# Publication II

Formation mechanisms of low-friction tribo-layers on  
arc-evaporated  $\text{TiC}_{1-x}\text{N}_x$  hard coatings

M. Rebelo de Figueiredo, J. Neidhardt, R. Kaindl, A. Reiter,  
R. Tessadri, C. Mitterer

Wear **265**(3–4), 525–532 (2008)



# Formation mechanisms of low-friction tribo-layers on arc-evaporated $\text{TiC}_{1-x}\text{N}_x$ hard coatings

M. Rebelo de Figueiredo<sup>a</sup>, J. Neidhardt<sup>a</sup>, R. Kaindl<sup>b</sup>, A. Reiter<sup>c</sup>, R. Tessadri<sup>b</sup>, C. Mitterer<sup>a</sup>

<sup>a</sup> Christian Doppler Laboratory for Advanced Hard Coatings at the Department of Physical Metallurgy and Materials Testing, University of Leoben, Franz-Josef-Strasse 18, A-8700 Leoben, Austria

<sup>b</sup> Institute of Mineralogy and Petrography, University of Innsbruck, 6020 Innsbruck, Austria

<sup>c</sup> Oerlikon Balzers AG, 9496 Balzers, Municipality of Liechtenstein, Austria

A detailed correlation of the tribological performance of arc-evaporated  $\text{TiC}_{1-x}\text{N}_x$  coatings with testing temperature, atmosphere as well as variation in load and sliding velocity is presented in this paper. The low-friction behavior in combination with its mechanical integrity are the reasons for the extensive industrial application of  $\text{TiC}_{1-x}\text{N}_x$  over the last decades. Still the tribo-mechanisms behind this performance are not yet completely understood. The present study adds further understanding, as the low-friction behavior degrades at elevated temperatures and dry or inert environments, which is related to the different constitution of the tribo-layer formed as investigated by Raman spectroscopy. Surprisingly, the wear rate of the coatings does not correlate with the coefficient of friction indicating the presence of different wear regimes.

**Keywords:** TiCN coatings; Low-friction mechanisms; Raman micro-spectroscopy; Ball-on-disc sliding; Ambient-dependent wear mechanisms

## 1 Introduction

$\text{TiC}_{1-x}\text{N}_x$  coatings have already been known for some decades and were introduced to the market in the middle 1980's. Within the frame of highly wear resistant coatings,  $\text{TiC}_{1-x}\text{N}_x$  has been proven as a good protective material especially due to its low friction, high hardness and high melting point which makes it useful for wide application in the tool industry [1, 2]. The development of methods based on moderate-temperature (MT) PVD as well as CVD processes has resulted in the production of coatings based on single-layer [3], multi-layer [4, 5] or graded  $\text{TiC}_{1-x}\text{N}_x$  [3, 6]. Studies of composition-structure-property relations of  $\text{TiC}_{1-x}\text{N}_x$  coatings have been carried out and revealed improved performance of third-generation (multilayer and graded) compared to single-layer coatings [7].

The versatility in terms of coating architecture of the system is due to the fact that TiC and TiN are isostructural and, thus, completely miscible via substitution of C for N in the face-centered cubic (fcc) lattice. Thus, the C/N ratio can be freely optimized and the properties tailored for a given application. Here, the commonly good adhesion and toughness of TiN compensates for the brittleness of TiC, while the latter provides for beneficial tribological properties [1]. From literature it is already known that, similar to other carbon-containing coatings [8–10],  $\text{TiC}_{1-x}\text{N}_x$  presents low-friction behavior, which might decrease or even eliminate the need for liquid lubrication [11].

The tribology of coatings in the Ti–C–N system is still only vaguely understood due to the complexity of the system and tribo-mechanisms active. Parallels can, however, be drawn to carbon-based coatings, e.g., diamond-like carbon (DLC). Several researchers already demonstrated that the low-friction behavior is determined, besides the composition of the coating, by the ambient atmosphere namely moisture [8, 12–14] and the material of the counter-body [15]. Fundamental tribological studies, namely by Singer et al., on, e.g., pure carbon films

in ambient air revealed that the observed low-friction and wear behavior might be explained by the moisture-dependent formation of a lubricious transfer layer acting as a third body in the sliding contact [16]. This finding is corroborated among others by Heimberg et al., who related the sliding velocity and, thus, exposure time of the contact to the swiftness of the water adsorption and/or reaction [11]. It was shown by Erdemir's group that the formation of the low-friction transfer film is caused by the complete transformation of the  $sp^3$ -rich DLC into  $sp^2$  graphitic carbon, through an annealing by thermal and strain effects from repeated friction at the asperities [17]. In addition, dangling bonds need to be saturated, e.g., by water molecules present in atmospheric moisture [18]. In order to trigger the aforementioned mechanism under dry conditions, most commercial DLC coatings are hydrogenated [8].

It is believed that similar friction-reducing mechanisms can be active for other ceramic C-containing coatings like  $TiC_{1-x}N_x$  [15, 19, 20]. Researchers like Huang et al. [19] and Takadom et al. [15] performed tribological tests of  $TiC_{1-x}N_x$  films at RT (room temperature) in ambient atmosphere, whereas a load-independent steady-state coefficient of friction (COF) demonstrated the toughness of the presumably graphitic transfer layer. Polcar et al. [20] performed sliding tests using steel (100Cr6) counterparts in ambient atmosphere at temperatures up to 300 °C and observed an increasing COF and wear, while the highest temperature leads already to excessive oxidation.

The main objective of this paper is, therefore, to systematically relate the variety of effects observed in numerous publications to one  $TiC_{1-x}N_x$  coating system under otherwise constant conditions. Thus, unlubricated sliding tests were conducted on Balinit B, which is an adapted commercial coating, using an inert counterpart ( $Al_2O_3$ ) under a variation of load, velocity, temperature and testing atmosphere.

## 2 Experimental

The tested commercial  $TiC_{1-x}N_x$  coating, Balinit B, was prepared by reactive arc-evaporation of Ti targets in an  $Ar/N_2/C_2H_2$  atmosphere in an industrial-scale arc-evaporation (Oerlikon Balzers, RCS 900) plant with a base pressure of less than  $10^{-3}$  Pa. The high-speed steel (HSS, DIN 1.3343, AISI M2) coupons ( $\varnothing$  30mm  $\times$  10 mm) used as substrates were ground and polished to a 3  $\mu m$  finish after quenching and tempering to a hardness of 65 HRC. Prior to deposition the samples were cleaned in an ultrasonic bath using ethanol. The samples were heated in situ to 450 °C and Ar ion etched for approximately 20 min utilizing a secondary gas discharge. In order to improve the adhesion, a TiN interlayer of approximately 1  $\mu m$  thickness was deposited. For the functional  $TiC_{1-x}N_x$  layer the  $C_2H_2$  flow was varied from 15 to 130 sccm, while the Ar flow was kept constant and  $N_2$  flow was backfilled to a 3 Pa total pressure as controlled by a capacitive gauge, forming a graded coating with a thickness of approximately 2.3  $\mu m$ , as determined by ball-cratering. To identify the crystal structure of the coating, X-ray diffraction (XRD) analysis was employed using a Siemens D500 Bragg-Brentano diffractometer and Cu  $K\alpha$  radiation. The average roughness was analyzed by an optical 3D white light profiling system (Wyko NT 1000) at 5 areas evenly distributed on the coating surface ( $5\times$  magnification). Hardness and Young's modulus were determined by microindentation (Fischerscope H100C) using a Vickers diamond indenter. The indents were made in constant depth mode down to 500 nm after the device was calibrated using the built-in procedures for hardness and shape correction on single crystalline sapphire (100).



The tribological tests were performed using ball-on-disc tribometers from CSM Instruments designed for tests at room and high temperature ( $\leq 700$  °C) with sintered polycrystalline  $\text{Al}_2\text{O}_3$  (alumina) balls as counterparts (purity of 99.8% and  $\varnothing$  6 mm), owing to their chemical inertness at high temperatures. RT tests were performed at varying loads (5, 10, 15, 20 N) and sliding velocities (0.10, 0.15, 0.20  $\text{m s}^{-1}$ ) in ambient air. A normal load of 5 N, a sliding speed of 0.10  $\text{m s}^{-1}$  as well as a constant wear track radius of 7 mm were set as standard parameters. A series of tests were conducted at temperatures ranging from RT to 200 °C. In addition, the influence of the surrounding atmosphere was studied using ambient air, dry nitrogen and dry (synthetic) air for tests at RT and 200 °C. An acrylic box that houses the system was filled with the respective gases and purged with each gas for approximately 2 h. The relative humidity for all tests was controlled by a hygrometer (Testo 608-H2) with an error of 2% (absolute). For the ambient air test, the relative humidity (HR) was 30%; for the dry nitrogen and dry air tests  $<1\%$ .

The worn-off volume of the coatings was evaluated by the same optical 3D white light profiling system (Wyko NT 1000) at 5 areas evenly distributed on the circumference of the wear track. From these measurements, the removed volume was determined and the wear coefficient calculated as the ratio between volume and applied load times sliding distance [21].

The Raman spectra were obtained at room temperature with a HORIBA Jobin Yvon LabRam-HR800 Raman microspectrometer excited with the 514.5 nm emission line of a 30mW  $\text{Ar}^+$ -laser. The laser spot on the surface had a diameter of approximately 1  $\mu\text{m}$  and a maximum power of 0.5 mW, which was low enough to prevent sample destruction due to local temperature increase. The emitted light was dispersed by a holographic grating with 300 grooves/mm and the dispersed light was collected by a  $1024 \times 256$  open electrode CCD detector. Spectra were recorded unpolarized in the spectral range 150–3500  $\text{cm}^{-1}$ . Raman mapping was done using a computer-controlled, automated x–y stage. Step width varied between 6 and 7  $\mu\text{m}$ . At each sampling point, two spectra were recorded for 5–8 s and spikes automatically removed. The laterally resolved spectra were fitted with Gauss-Lorentz functions considering a 2nd order polynomial background. The spectral parameters of these fits such as amplitude, intensity or position were then used for grey-scale coded mapping of the corresponding features.

## 3 Results

### 3.1 Coating characterization

The carbide-rich Balinit B coatings exhibit a shiny silver-gray coloration on the surface and are well adherent to the substrates, with a number of 1–2 for the Rockwell C adhesion tests [22]. They were deposited up to a total thickness of  $3.3 \pm 0.1$   $\mu\text{m}$ . The surface with an average roughness ( $R_a$ ) of  $13 \pm 2$  nm and a root mean square roughness ( $R_q$ ) of  $30 \pm 10$  nm is rather smooth in comparison to other arc-evaporated coatings [23]. According to XRD, an fcc crystalline structure ( $Fm-3m$  space group) was obtained with a [111] texture. The obtained microhardness ( $H_{IT}$ ) and Young's modulus ( $E_{IT}$ ) of  $23.8 \pm 2.4$  and  $293 \pm 8$  GPa, respectively, slightly exceed the values commonly observed for TiN [24].

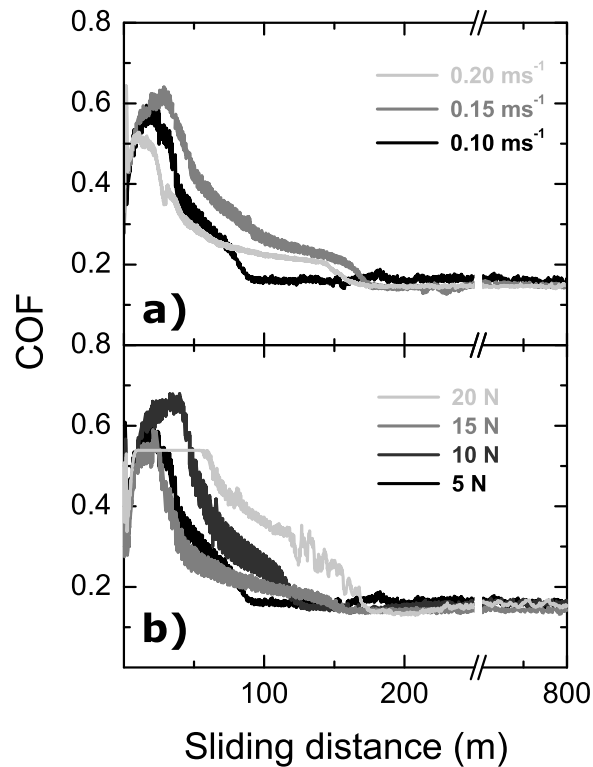


Figure 1: Friction curves for the tribological tests performed with different sliding velocities (0.10, 0.15, 0.20  $\text{ms}^{-1}$ ), therefore different cycle frequencies (2.23, 3.41, 4.55  $\text{s}^{-1}$ , respectively), and different loads (5, 10, 15, 20 N) at room-temperature and in ambient air.

## 3.2 Tribological characterization

### 3.2.1 Velocity and load variation

The development of the COF with sliding distance at different velocities (0.10, 0.15, 0.20  $\text{m s}^{-1}$ ) and at different loads (5, 10, 15, 20 N) is shown in Fig. 1 for tests at room temperature in ambient air with  $\text{HR} = 30\%$ . After a running-in period, during which presumably asperities are leveled, all coatings reach a rather low and stable steady-state COF of  $\sim 0.17$  regardless the load and velocity.

Differences can, however, be observed in the extension of the running-in segment. For the lowest velocity (0.10  $\text{m s}^{-1}$ ), the friction curve exhibits the shortest running-in distance reaching a steady-state COF after  $\sim 90\text{m}$  under the specified conditions (Fig. 1a). At the higher velocities of 0.15 and 0.20  $\text{m s}^{-1}$  its extension almost doubles reaching steady-state after  $\sim 165\text{ m}$ . The calculated wear rates of the coating on the other hand are rather constant with an average of  $4.5 \pm 0.3 \times 10^{-16} \text{ m}^3 \text{ N}^{-1} \text{ m}^{-1}$ . A minor difference can still be resolved for the wear rate of the alumina counterpart, which is increasing slightly from 0.9 to  $1.3 \times 10^{-17} \text{ m}^3 \text{ N}^{-1} \text{ m}^{-1}$  and might be correlated to the higher wear experienced during a longer running-in period.

A similar tendency can be seen for the load series in Fig. 1b. The shortest running-in ( $\sim 90\text{ m}$ ) is observed for the lowest load of 5 N, which is increasing to approximately 125,

150 and 175 m for the test at 10, 15 and 20 N, respectively. Surprisingly, the highest wear rate ( $4.4 \pm 0.2 \times 10^{-16} \text{ m}^3 \text{ N}^{-1} \text{ m}^{-1}$ ) is observed for the lowest load of 5 N, while it decreases to a constant value of  $2.3 \pm 0.3 \times 10^{-16} \text{ m}^3 \text{ N}^{-1} \text{ m}^{-1}$  for 10, 15 and 20 N. The decrease in coating wear coincides with a slight increase in the counterpart wear from  $0.9$  to  $1.4 \times 10^{-17} \text{ m}^3 \text{ N}^{-1} \text{ m}^{-1}$ .

### 3.2.2 Testing temperature variation for ambient air tests

In order to investigate the impact of water adsorption on the evolution of the COF and the respective coating wear, tribological tests in ambient air (HR = 30%) at temperatures increasing from 25 to 200 °C were conducted. Fig. 2 clearly shows an increase in the steady-state COF from 0.17 to 0.7 with temperature, combined with an increase in scattering. At the same time the wear depth increases from 0.2 to 1.5  $\mu\text{m}$ .

### 3.2.3 Variation of testing atmosphere

To verify the impact of ambient moisture and atmosphere on the tribo-mechanisms, tests in dry and ambient air as well as in dry  $\text{N}_2$  and Ar were conducted at 25 and 200 °C, respectively.

**3.2.3.1. At 25 °C.** The friction curves and the wear depths from the tribological tests performed at RT are shown alongside with the resulting wear scars in Fig. 3. As mentioned before, the COF for the test in ambient air swiftly reaches a low steady-state of 0.17. In contrast to that, the COF for the test in both dry environments (synthetic air,  $\text{N}_2$ ) exhibits an increase to 0.7–0.8. Surprisingly, the fourfold increase in COF does not lead to an increase in wear. While the experiments in air (dry and moist) exhibit a comparable wear ( $\sim 4.4 \times 10^{-16} \text{ m}^3 \text{ N}^{-1} \text{ m}^{-1}$ ), a smaller wear scar is noticeable for the tests in dry  $\text{N}_2$  ( $\sim 0.9 \times 10^{-16} \text{ m}^3 \text{ N}^{-1} \text{ m}^{-1}$ ) (Fig. 3). As for the counterparts, the test in ambient air resulted in the lowest wear ( $0.9 \times 10^{-17} \text{ m}^3 \text{ N}^{-1} \text{ m}^{-1}$ ), which doubled for the  $\text{N}_2$  experiment and even quadrupled for dry (synthetic) air. This points towards significantly different wear mechanisms active in the respective atmospheres, which will be discussed later.

**3.2.3.2. At 200 °C.** As mentioned already (see also Fig. 2), no drop in COF to the low-friction regime is observed for the test in ambient air at elevated temperatures. For all atmospheres it is rather constant at 0.6–0.7 (Fig. 3). For  $\text{N}_2$  and dry air, a slight decrease in COF from 0.8 at RT to 0.6 and 0.7 at 200 °C can be seen in Fig. 3. The coating wear at 200 °C is, however, increasing significantly for all atmospheres as compared to the respective RT tests. For ambient air it augments by a factor of 5 ( $2.1 \times 10^{-15} \text{ m}^3 \text{ N}^{-1} \text{ m}^{-1}$ ), for synthetic air by a factor of 7 ( $3.3 \times 10^{-15} \text{ m}^3 \text{ N}^{-1} \text{ m}^{-1}$ ) and for dry  $\text{N}_2$  by a factor of 9 ( $0.9 \times 10^{-15} \text{ m}^3 \text{ N}^{-1} \text{ m}^{-1}$ ), whereas the coating in dry air wears most as compared to ambient air and dry  $\text{N}_2$  (see Fig. 3). A test in Ar atmosphere was also added to clarify whether  $\text{N}_2$  can still be assumed as chemically inert even at 200 °C, which was confirmed by the within the error identical results in terms of COF and wear, as displayed in Figs. 3 and 4. The wear of the alumina counterparts remains roughly constant (ambient air) or is decreasing slightly (dry air,  $\text{N}_2$ ) as compared to RT, with the lowest value of  $1.2 \times 10^{-17} \text{ m}^3 \text{ N}^{-1} \text{ m}^{-1}$  for the ambient air test increasing to 1.4 and  $2.1 \times 10^{-17} \text{ m}^3 \text{ N}^{-1} \text{ m}^{-1}$  for  $\text{N}_2$  and dry air, respectively.

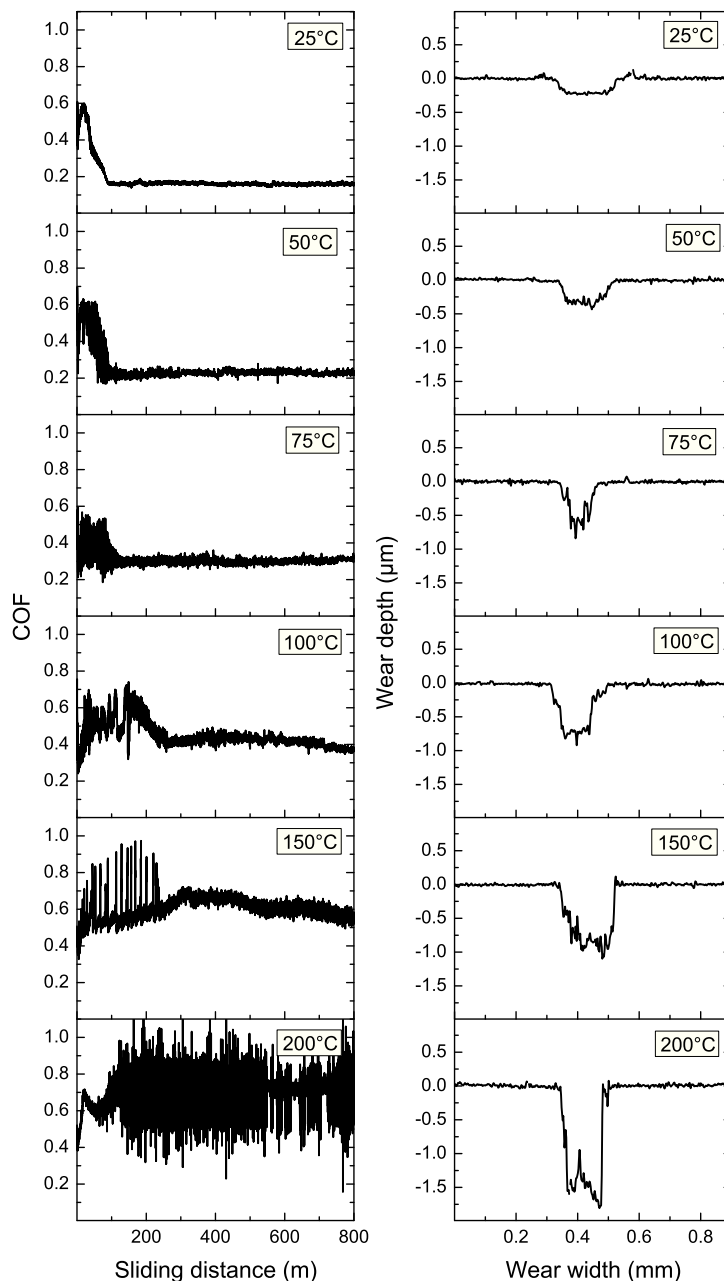


Figure 2: Friction curves and wear depths for the tribological tests with different temperatures in ambient air and using a sliding velocity and load of  $0.10 \text{ ms}^{-1}$  and  $5 \text{ N}$ , respectively.

### 3.2.4 Raman micro-spectroscopy

Raman analysis was performed on the coating and counterpart wear scars in order to identify eventual transfer films and their constitution. The spectra taken from the  $\text{TiC}_{1-x}\text{N}_x$  coating surface and within the wear tracks exhibit two broad and split bands at low wave numbers ( $\sim 300$  and  $\sim 600 \text{ cm}^{-1}$ ) (example shown in Fig. 5a). Identical spectral parameters indicate that no altered material is attached to the coating regardless the testing conditions. Con-

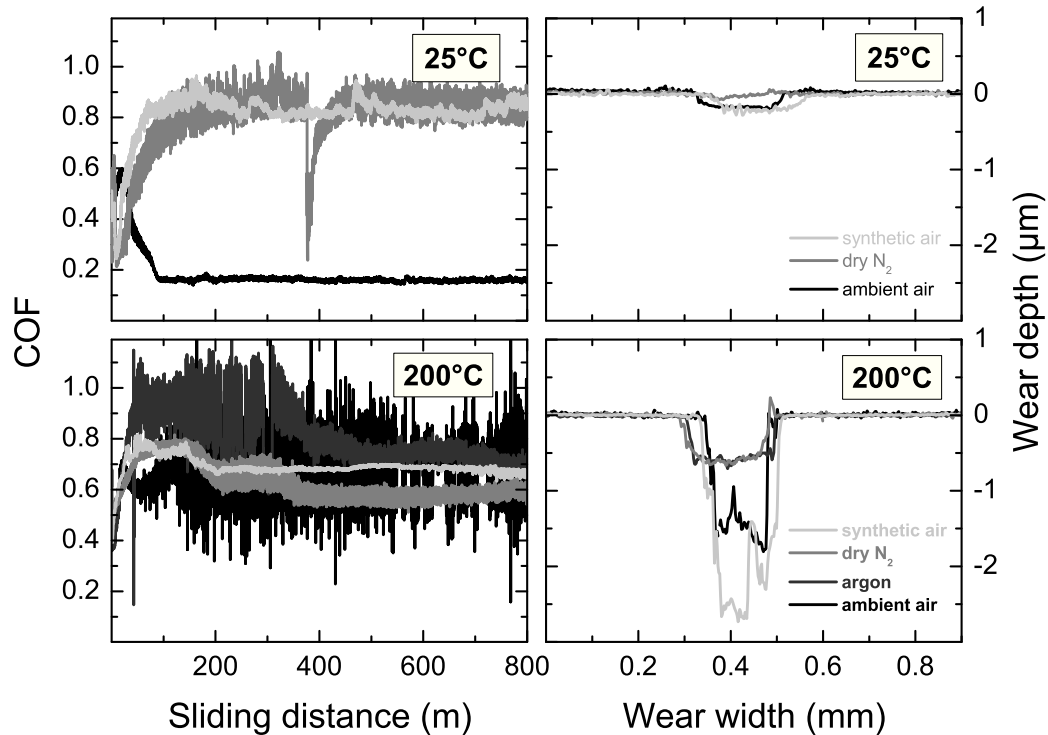


Figure 3: Friction curves for the tests performed at RT in different atmospheres (synthetic air, dry nitrogen and ambient air) under a load of 5 N and a velocity of  $0.10 \text{ ms}^{-1}$  alongside with the curves for the tests performed at  $200^\circ\text{C}$  in different atmospheres (synthetic air, dry nitrogen, argon and ambient air). The spike in the trace of the  $\text{N}_2$  test at  $\sim 375 \text{ m}$  is an experimental artifact.

versely, the optical microscopy images of counterpart wear scars shown in Fig. 6 reveal the existence of transfer layers for all testing atmospheres. This was confirmed by the mappings shown in the next column in Fig. 6 (mapping A). Here, the intense Raman band of  $\text{Al}_2\text{O}_3$  at  $420 \text{ cm}^{-1}$  (Fig. 5b) was mapped, which disappeared inside the wear scar confirming the coverage by transferred material.

In order to draw conclusion about the nature of the transfer films, their respective spectra were processed. For instance, two broad bands around  $430$  and  $600 \text{ cm}^{-1}$  are present for all three tests (Fig. 5b) and can be related to  $\text{TiC}_{1-x}\text{N}_x$  (Fig. 5a), while contributions from  $\text{TiO}_2$  cannot be ruled out. Thus, unaltered as well as modified coating material is present on the counterpart as shown in Fig. 6 (mapping C), while the eventual oxidation might have occurred after the actual test. Furthermore, the presence of amorphous carbon was confirmed by the characteristic D- and G-bands around  $1350$  and  $1580 \text{ cm}^{-1}$  even for the tests in synthetic air and dry nitrogen, where no low friction was observed (see respective mapping B in Fig. 6). However, only for the test in ambient air several intense, relatively sharp bands between  $2800$  and  $3100 \text{ cm}^{-1}$ , accompanied by weaker bands around  $1200$ – $1700 \text{ cm}^{-1}$ , were detected and mapped (Fig. 6: mapping B). Such features are generally assigned to stretching and bending vibrations of functional C–H and C–O groups, offering a potential explanation for the low-friction effect under ambient air.

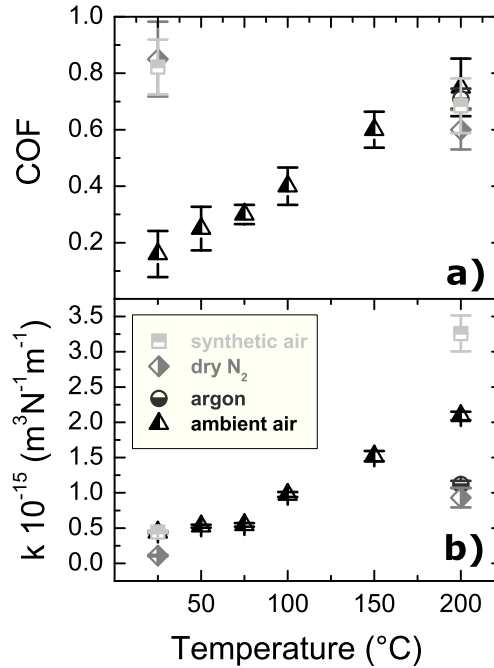


Figure 4: Summary of the steady-state COFs and wear depths obtained at different temperatures (25, 50, 75, 100, 150 and 200 °C) in different test atmospheres (synthetic air, dry nitrogen, argon and ambient air).

## 4 Discussion

### 4.1 Influence of sliding velocity and load

It is widely assumed in literature that the reduction in friction observed in C-containing materials is due to a transformation of the material under the presence of water and/or the subsequent formation of a low-friction tribo-layer [17]. Similar to vapor-phase lubrication [25], such processes strongly depend on the partial gas pressure of the adsorbate (moisture), available areas for adsorption (active sites on the coating) as well as exposure time to the environment (passing frequency of the counterpart).

The fact that the COF was constant over the velocity range studied (Fig. 1) indicates the swiftness of the tribo-layer forming reactions, whereas the highest velocity corresponds to a passing frequency of 13 Hz and a time constant of less than 77 ms. This time constant is by orders of magnitude longer than typical adsorption frequencies of atmospheric moisture for DLC coatings [26] and, thus, no significant impact is expected. However, the almost twofold increase of the running-in period (Fig. 1) with increasing velocity already indicates some kinetic limitation of the initial tribochemical reactions. Further studies will be performed, going to higher velocities (shorter time constants), to elucidate the kinetics of the formation mechanisms.

Once the friction reduction has been established it shows a surprising stability, since even a fourfold increase in load from 5 to 20 N, corresponding to initial contact pressures of 1.4–2.2 GPa, did not affect the low steady-state COF of 0.18 (Fig. 1b). However, the increasing length of the running-in period with load (Fig. 1b) as well as the larger scatter in COF for

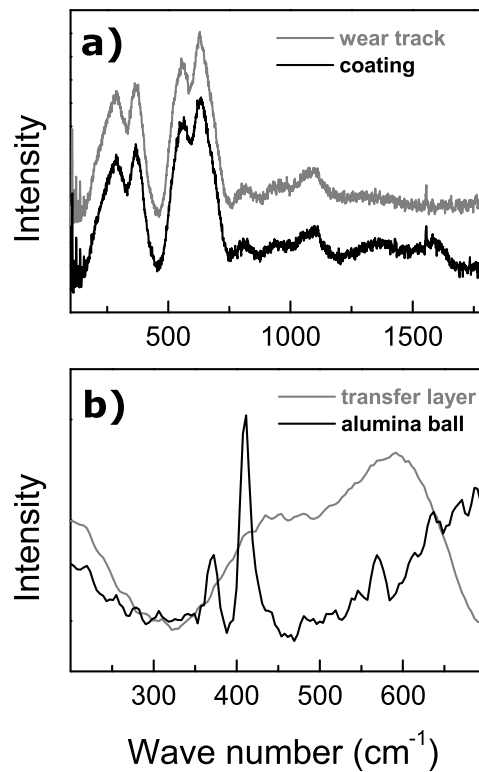


Figure 5: Comparison between baseline-corrected Raman spectra of the coating surface and the respective wear track (a) as well as between the alumina ball and the transfer layer on the counterpart wear scar (b) after the test in dry  $N_2$  at 25 °C.

higher loads during running-in indicates a slightly hampered initial formation process.

## 4.2 Role of atmospheric moisture

As afore mentioned, the formation of the friction-reducing tribo-layer seems to depend, among others, strongly on the presence and adsorption probability of moisture. Increasing the testing temperature, while keeping the other experimental parameters constant, should, thus, decrease the sticking coefficient of water molecules significantly [27] and by that should affect the formation of the tribo-layer. In order to study this effect and to verify the importance of water adsorption for the friction-reducing mechanisms, sliding tests were conducted at temperatures ranging from RT to 200 °C, while the impact of different atmospheres was investigated at RT and maximum temperature. As summarized in Fig. 4a, the steady-state COF shows an almost linear increase with temperature, which coincides with a linear decrease of the water adsorption probability in that range [27]. This corroborates the established notion that moisture plays a vital role for the friction-reducing reactions and the subsequent lubricious tribo-layer formation.

Not surprisingly, the wear coefficient (Fig. 4b) is also increasing linearly with the COF towards higher temperatures. This indicates a constant combination of wear regimes throughout the range of investigated temperatures. This test series does, however, not provide information about the respective contribution of chemical wear, such as oxidation and water

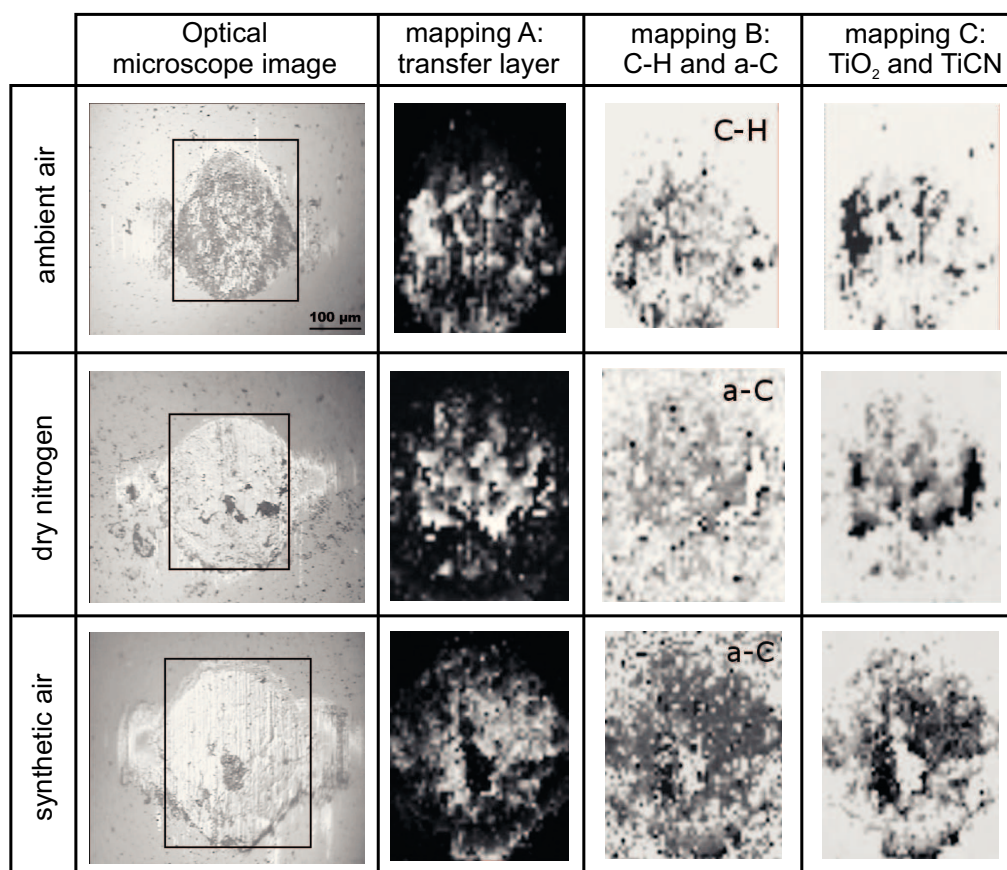


Figure 6: Optical micrographs and Raman mappings of the wear scars on the alumina counterparts after ball-on-disc tests in ambient air, dry nitrogen and synthetic air; mapping A shows the existence of a transfer layer for all three atmospheres; mapping B indicates the presence of C–H bonds exclusively for tests in ambient air as well as amorphous C for dry nitrogen and synthetic air; mapping C shows the distribution of transferred unaltered as well as oxidized coating materials.

modification of  $\text{TiC}_{1-x}\text{N}_x$  surface layers, or mechanical wear by, e.g., abrasion or fatigue. In order to discriminate between these different contributions, tests at different atmospheres were conducted.

### 4.3 Role of ambient gas chemistry

For the tests in Ar, N<sub>2</sub> and synthetic air no moisture is present inhibiting the low-friction effect. This manifests itself in a dramatically increased COF, which is comparable to the moist tests at the highest temperature. Most interestingly, the fourfold increase in COF at RT does not lead to an increase in wear. Even no wear was observable for the tests in inert gas leading to the conclusion that a sole mechanical wear process does not play a significant role at RT. The comparable wear rates for moist and dry air coinciding with significantly different COF indicate different chemical wear processes which are in case of synthetic air predominantly oxidative, while under presence of moisture the water-modified surface layers



are removed and partially transferred to the ball presumably as lubricious tribo-layer. The extent of oxidative wear becomes even more clear for the tests conducted at 200 °C where the wear in dry air exceeds the moist conditions significantly, regardless the rather constant COF. This leads to the notion that even at 200 °C adsorbed water might still saturate dangling bonds and by that is hampering material loss by oxidation. However, mechanical wear also becomes important under these conditions as indicated by the noticeable wear for the inert gas tests.

#### 4.4 Formation and constitution of tribo-layers

The common tenor in the literature concerning the tribology of carbon-based coatings links the low-friction behavior to the formation of 3rd bodies in the contact and the subsequent formation of lubricious tribo-layers. For ceramic  $\text{TiC}_{1-x}\text{N}_x$ , however, transfer layers were found for all testing atmospheres regardless the occurrence of the low-friction effect. These layers exclusively form on the counterpart and contain predominantly  $\text{TiC}_{1-x}\text{N}_x$  as well as  $\text{TiO}_x$ . The latter can either be attributed to in situ tribo-oxidation (air tests) or ex situ oxidation of metallic wear debris ( $\text{N}_2$  test). Most importantly, nanocrystalline amorphous carbon was detected also for the high-friction dry tests while only for the test with atmospheric moisture vibrational bands typical for C–H bonds occurred. The very fine crystalline carbon (high D/G ratio) can be assumed to possess no macroscopic shear systems and, therefore, does not provide for a low-friction effect. The formation of C–H bonds under the influence of atmospheric moisture on the other hand seems to be a prerequisite for the low-friction effect but also coincides with an increase in wear. The reduction in friction might therefore be attributed to the liberation and agglomeration of carbon from the  $\text{TiC}_{1-x}\text{N}_x$  coating by tribochemical processes and the subsequent saturation of dangling bonds by atmospheric moisture providing for low shearing but also for an accelerated wear.

## 5 Conclusions

The present study confirms that the low-friction effect of  $\text{TiC}_{1-x}\text{N}_x$  is tightly connected to the presence of atmospheric moisture, as indicated by its absence for ball-on-disc tests against alumina counterparts conducted in inert gas (Ar),  $\text{N}_2$  as well as dry air (relative humidity, 1%). The coefficient of friction (COF) of the moist test is an almost linear function of testing temperature (25 → 200 °C), leading to the notion that water adsorption to the surface of the wear scar is the key step of the low-friction mechanism. Similar effects are observed for carbon-based coatings (metal-, hydrogenated-) diamond-like carbon (DLC), which is initially surprising, since bonding structure and coordination is significantly different from the ceramic structure of  $\text{TiC}_{1-x}\text{N}_x$ . Thus, a graphite-based lubrication via the liberation and macroscopic clustering of carbon atoms in a  $\text{sp}^2$  coordinated fashion in the tribo-contact is highly unlikely. This statement is reinforced by Raman spectroscopy, where only bands of amorphous carbon are detected for all conditions, which do not provide for a low-friction effect. Instead, the detection of compounds containing CH bondings for the low-friction test in moist air confirms the common tenor of the DLC literature that the adsorption of water saturates dangling bonds and by that separates the two counterparts via a low-shear interlayer even for carbon containing ceramic coatings, where load and velocity variation

seem not to have a significant influence (within the studied range).

No correlation between the COF and wear can be established. The high-friction (COF  $\sim 0.8$ ) tests in inert gas (Ar) and N<sub>2</sub> result in almost no detectable wear, whereas the by factor of four lower COF for the test under moist conditions exhibits an accelerated wear, which is comparable to the high COF tests in dry air leading to the conclusion that different wear mechanisms must be active. A significant contribution of mechanical wear by, e.g., fatigue under the given conditions can be ruled out from the absence of wear for the high COF inert gas tests. The accelerated wear for the dry air tests under a similar COF confirms, on the other hand, a significant chemical wear presumably by tribo-oxidation. The same level of wear is observed for the low-friction test under moist conditions inferring besides oxidation a material consumption by water-modification related processes. Still, the precise mechanisms of the complex interplay of liberation, transfer and water-based saturation of carbon in both systems is yet not fully understood.

## Acknowledgement

Financial support by the Christian Doppler Research Association as well as Plansee GmbH (Lechbruck, Germany) is highly acknowledged.

## References

- [1] L. Karlsson, L. Hultman, M. P. Johansson, J. E. Sundgren, and H. Ljungcrantz, *Surf. Coat. Technol.*, 2000, **126**, 1–14.
- [2] A. Forn, J. A. Picas, G. G. Fuentes, and E. Elizalde, *Int. J. Refract. Met. Hard Mater.*, 2001, **19**, 507–513.
- [3] S. J. Bull, D. G. Bhat, and M. H. Staia, *Surf. Coat. Technol.*, 2003, **163–164**, 499–506.
- [4] C. Wei, J. Fin Lin, T.-H. Jiang, and C.-F. Ai, *Thin Solid Films*, 2001, **381**, 94–103.
- [5] E. Bemporad, C. Pecchio, S. De Rossi, and F. Carassiti, *Surf. Coat. Technol.*, 2001, **146–147**, 363–370.
- [6] K. Narasimhan, S. P. Boppana, and D. G. Bhat, *Wear*, 1995, **188**, 123–129.
- [7] S. J. Bull, D. G. Bhat, and M. H. Staia, *Surf. Coat. Technol.*, 2003, **163–164**, 507–514.
- [8] J. Andersson, R. A. Erck, and A. Erdemir, *Wear*, 2003, **254**, 1070–1075.
- [9] V. Derflinger, H. Brandle, and H. Zimmermann, *Surf. Coat. Technol.*, 1999, **113**, 286–292.
- [10] M. A. Gomez, J. Romero, A. Lousa, and J. Esteve, *Surf. Coat. Technol.*, 2005, **200**, 1819–1824.
- [11] J. A. Heimberg, K. J. Wahl, I. L. Singer, and A. Erdemir, *Appl. Phys. Lett.*, 2001, **78**, 2449–2451.
- [12] J. Andersson, R. A. Erck, and A. Erdemir, *Surf. Coat. Technol.*, 2003, **163–164**, 535–540.

- [13] A. Erdemir, M. Switala, R. Wei, and P. Wilbur, *Surf. Coat. Technol.*, 1991, **50**, 17–23.
- [14] H. Ronkainen, S. Varjus, J. Koskinen, and K. Holmberg, *Wear*, 2001, **249**, 260–266.
- [15] J. Takadoum, H. H. Bennani, and M. Allouard, *Surf. Coat. Technol.*, 1997, **88**, 232–238.
- [16] I. Singer and K. Wahl, MRS Workshop Series: Tribology on the 300th Anniversary of Amonton’s Law, 1999.
- [17] Y. Liu, A. Erdemir, and E. I. Meletis, *Surf. Coat. Technol.*, 1996, **82**, 48–56.
- [18] A. Erdemir and C. Donnet, *J. Phys. D: Appl. Phys.*, 2006, **39**, R311–R327.
- [19] S. W. Huang, M. W. Ng, M. Samandi, and M. Brandt, *Wear*, 2002, **252**, 566–579.
- [20] T. Polcar, R. Novak, and P. Siroky, *Wear*, 2006, **260**, 40–49.
- [21] E. Rabinowicz, *Friction and Wear of Materials*, John Wiley, New York, 1964.
- [22] *Quality assurance of PVD and CVD hard coatings*, VDI guideline 3824, 2001.
- [23] R. J. Rodriguez, J. A. Garcia, A. Medrano, M. Rico, R. Sanchez, R. Martinez, C. Labrugere, M. Lahaye, and A. Guette, *Vacuum*, 2002, **67**, 559–566.
- [24] J. Neidhardt, M. O’Sullivan, A. E. Reiter, W. Rechberger, W. Grogger, and C. Mitterer, *Surf. Coat. Technol.*, 2006, **201**, 2553–2559.
- [25] W. G. Sawyer and T. A. Blanchet, *Journal of Tribology*, 2001, **123**, 572–581.
- [26] P. L. Dickrell, W. G. Sawyer, and A. Erdemir, *Journal of Tribology*, 2004, **126**, 615–619.
- [27] P. Stoltze, *Introduction to Heterogeneous Catalysis*, tech. rep., Department of Chemistry and Applied Engineering Science, Aalborg University, Denmark, 2007.



# Publication III

## Low-Friction Mechanisms Active for Carbon Containing Coatings: Ti-C-N as a Model System

M. Rebelo de Figueiredo, J. Neidhardt, R. Franz and C. Mitterer

Berg- und Hüttenmännische Monatshefte : BHM **153(7)** 263–267 (2008)



# Low-Friction Mechanisms Active for Carbon Containing Coatings: Ti-C-N as a Model System

M. Rebelo de Figueiredo, J. Neidhardt, R. Franz, C. Mitterer

*Christian Doppler Laboratory for Advanced Hard Coatings, Department of Physical Metallurgy and Materials Testing, Montanuniversität Leoben, Franz-Josef-Straße 18, 8700 Leoben / Austria*

A detailed investigation of the tribological performance of an arc-evaporated  $\text{TiC}_{1-x}\text{N}_x$  coating in various testing atmospheres at room temperature is presented in this paper to add further understanding to the tribomechanisms behind the well-known low-friction performance of TiCN hard coatings. The low-friction behaviour is only present for environments where water vapour is present. Surprisingly, the wear rate of the coatings does not correlate with the coefficient of friction indicating the existence of different wear regimes. Raman spectroscopy points towards liberation and agglomeration of carbon by tribochemical processes and the subsequent saturation of its dangling bonds by water absorption.

*Niedrigreibungseffekte in kohlenstoffhaltigen Schichten: Ti-C-N als Modellsystem.* Der vorliegende Artikel beinhaltet eine ausführliche Untersuchung der tribologischen Eigenschaften von  $\text{TiC}_{1-x}\text{N}_x$ -Hartstoffschichten, die mittels Lichtbogenverdampfung hergestellt wurden. Durch die Variation der Atmosphäre bei den verschiedenen tribologischen Tests bei Raumtemperatur konnten neue Erkenntnisse über die Mechanismen, die zum bekannten Niedrigreibungseffekt führen, gewonnen werden. Hierbei zeigte sich, dass niedrige Reibwerte nur bei Vorhandensein von Wasserdampf in der Atmosphäre auftreten, wobei der Reibwert überraschenderweise nicht mit dem Schichtverschleiß korreliert, was auf das Auftreten unterschiedlicher Verschleißmechanismen hindeutet. Aus Untersuchungen mit Hilfe der Raman-Spektroskopie konnte die Freisetzung und Anlagerung von Kohlenstoff durch tribochemische Prozesse abgeleitet werden sowie die nachfolgende Sättigung der freien Bindungen durch die Absorption von Wassermolekülen.

## 1 Introduction

Dry machining leads to a considerable reduction in waste materials and remains a significant goal in environmentally conscious manufacturing. One of the most promising routes to achieve this objective is through self-lubrication of coated tool surfaces.  $\text{TiC}_{1-x}\text{N}_x$  coatings are well-known examples for this approach. This system has already been known for some decades and has been introduced to the market in the middle 1980's. Within the frame of highly wear-resistant coatings,  $\text{TiC}_{1-x}\text{N}_x$  has been proven as a good protective material especially due to its low friction, high hardness and high melting point, which makes it useful for a wide range of applications in the tool industry [1, 2]. The development of methods based on moderate-temperature physical vapour deposition (PVD) as well as chemical vapour deposition (CVD) processes has resulted in the production of coatings based on single-layer [3], multilayer [4, 5] or compositionally graded  $\text{TiC}_{1-x}\text{N}_x$  [3, 6]. The flexibility of the system in terms of coating architecture is due to the fact that TiC and TiN are completely miscible via substitution of C for N in the face-centered cubic (fcc) lattice. Thus, the C/N ratio can be freely optimized and the properties tailored for a given application. Here, the commonly good adhesion and toughness of TiN compensates for the brittleness of TiC, while the latter provides for beneficial tribological properties<sup>1</sup>. From literature it is already known that, similar to other carbon containing coatings [7–9],  $\text{TiC}_{1-x}\text{N}_x$  presents low-friction behaviour [10]. On the other hand, the tribochemical mechanisms active for

coatings in the Ti-C-N system are still only vaguely understood due to the complexity of the system and the active tribomechanisms. Parallels can, however, be drawn to carbon based coatings, e.g., diamond-like carbon (DLC). Several researchers already demonstrated that the low-friction behaviour is determined, besides the composition of the coating, by the ambient atmosphere, namely moisture [7, 11–13] and the material of the counterbody [14]. Fundamental tribological studies, namely by Singer et al. [15], on, e.g., pure carbon films in ambient air revealed that the observed low-friction and wear behaviour might be explained by the moisture-dependent formation of a lubricious transfer layer acting as a third body in the sliding contact. This finding is corroborated among others by Heimberg et al. [10], who related the sliding velocity and, thus, exposure time of the contact to the swiftness of the water adsorption and/or reaction. It was shown by Erdemir's group that the formation of the low-friction transfer film is caused by the complete transformation of the  $sp^3$ -rich DLC into  $sp^2$  graphitic carbon, through an annealing by thermal and strain effects from repeated friction at the asperities [16]. In addition, dangling bonds need to be saturated, e.g., by water molecules present in atmospheric moisture [17]. In order to trigger the aforementioned mechanism under dry conditions, most commercial DLC coatings are hydrogenated [7].

It is believed that similar friction-reducing mechanisms can be active for other ceramic carbon containing coatings like  $TiC_{1-x}N_x$  [14, 18, 19]. Researchers like Huang et al. [18] and Takadom et al. [14] performed tribological tests of  $TiC_{1-x}N_x$  films at room temperature in ambient atmosphere, whereas a load-independent steady-state coefficient of friction (COF) demonstrated the toughness of the presumably graphitic transfer layer.

In the present work a series of  $TiC_{1-x}N_x$  coatings was synthesized by cathodic arc-evaporation where the  $C_2H_2$  flow was kept constant at different values during deposition. The coating with optimum composition, i.e., lowest running-in period, was tribologically tested in different atmospheres in order to elucidate the friction and wear mechanisms active for  $TiC_{1-x}N_x$  (ceramic) coatings.

## 2 Experimental

The tested  $TiC_{1-x}N_x$  coatings were prepared by reactive cathodic arc-evaporation of Ti targets in an  $Ar/N_2/C_2H_2$  atmosphere in an industrial scale arc-evaporation (Oerlikon Balzers, RCS 900) plant with a base pressure of less than  $10^{-3}$  Pa. The high-speed steel (HSS, DIN 1.3343, AISI M2) coupons ( $\varnothing$  30 mm) used as substrates were ground and polished to a 3  $\mu m$  finish after quenching and tempering to a hardness of 65 HRC. Prior to deposition, the samples were cleaned in an ultrasonic bath using ethanol. The samples were heated in-situ to 450°C and Ar ion etched for approximately 20 min utilizing a secondary gas discharge. To improve the adhesion, a TiN interlayer ( $\sim 0.8$   $\mu m$ ) was deposited. For the compositionally homogeneous functional  $TiC_{1-x}N_x$  layer, the  $C_2H_2$  flow was adjusted between 20 and 130 sccm (standard cubic centimeters per minute), while the Ar flow was kept constant and  $N_2$  flow was backfilled to a total pressure of 3 Pa as controlled by a capacitive gauge. After a deposition time of 80 min, the resulting coatings had a thickness of approximately 8  $\mu m$ , as determined by ball cratering.

The composition of the coating chosen for tribological testing was investigated by elastic recoil detection analyses (ERDA). The compositional depth profile of the coating was determined by a primary beam of 350 MeV Au ions. The forward scattered coating atoms



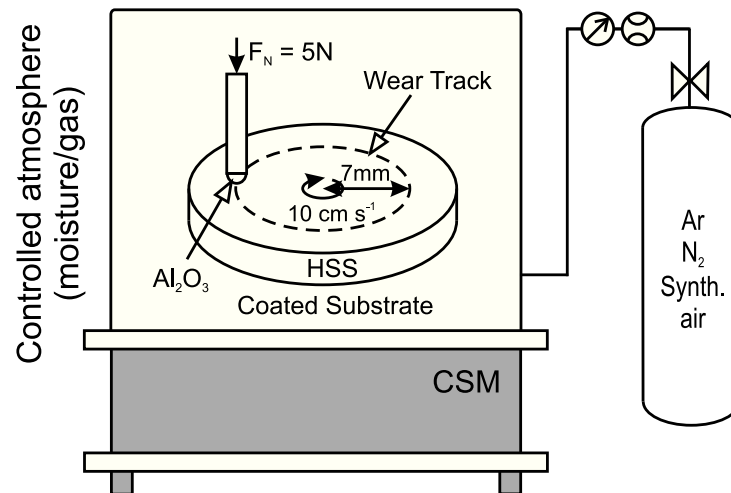


Figure 1: Experimental apparatus of the ball-on-disc tests performed in different testing atmospheres

were analysed using a detection system with a solid angle of 0.4 msr and a large detection angle of  $60^\circ$ , which enables simultaneous detection of all elements [20]. The identification of the crystal structure was done via X-ray diffraction (XRD) using a Siemens D 500 Bragg-Brentano diffractometer and  $\text{Cu-K}\alpha$  radiation. The average roughness was measured with an optical 3D white light profiling system (Wyko NT 1000) at 5 areas evenly distributed on the coating surface ( $5\times$  magnification). Hardness and Young's modulus were determined by microindentation (Fischerscope H100C) using a Vickers diamond indenter. The indents were made in constant depth mode down to 500 nm after the device was calibrated using the built-in procedures for hardness and shape correction on single crystalline sapphire (100).

The tribological tests were performed on a ball-on-disc tribometer from CSM Instruments designed for tests at room temperature with  $\text{Al}_2\text{O}_3$  (alumina) balls as counterparts (purity of 99.8 % and  $\varnothing$  6 mm). For the tests, a normal load of 5 N, a sliding speed of  $0.10 \text{ ms}^{-1}$  as well as a constant wear track radius of 7 mm were used as standard parameters. A sliding distance of 2500 m was chosen for the coating-selection test and 3000 m for the tests in different surrounding atmospheres, namely ambient air,  $\text{N}_2$ , Ar, and synthetic air. An acrylic box housing the system was filled with the respective gases and purged for approximately 2 hours (Fig. 1). The relative humidity for all tests was recorded by a hygrometer (Testo 608-H2) with an error of  $\pm 2 \%$  (absolute). For the ambient air test, the relative humidity (HR) was 33 %; for the  $\text{N}_2$ , Ar and synthetic air tests  $< 1 \%$ .

The worn-off volume of the coatings was evaluated by the same optical 3D white light profiling system (Wyko NT 1000) at 5 spots evenly distributed on the circumference of the wear track. From these measurements, the removed volume was determined and the wear coefficient of the coating,  $k_{\text{coating}}$ , calculated as the ratio between volume and applied load times sliding distance [21]. In case of the ball counterparts, the worn-off volume for the wear coefficient,  $k_{\text{ball}}$ , was calculated from the diameter of the wear scar on the counterpart.

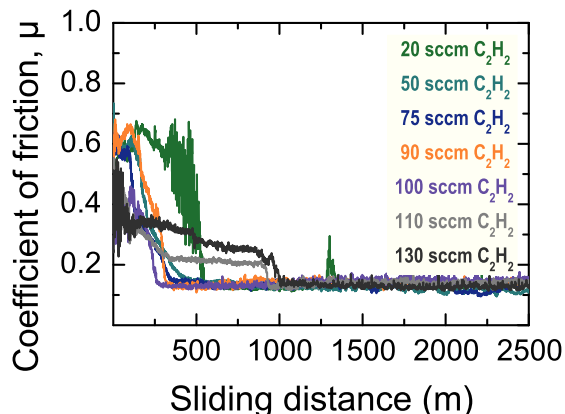


Figure 2: Results of the tribological tests conducted at RT and ambient air for all the coatings deposited; the selected homogeneous coating presents the shortest running-in period

## 3 Results

### 3.1 Coating Characterization and Selection

The coloration of the  $\text{TiC}_{1-x}\text{N}_x$  coatings goes from golden to grey, depending on the  $\text{C}_2\text{H}_2$  flow, i.e., the carbon content in the coating. All coatings deposited are well adherent to the substrates with a number of 1–2 for the Rockwell C indentation tests [22] and present a surface average roughness ranging from 15 to 30 nm.

The selection criterion of the coating to be used for the tribological tests in different atmospheres was based on the shortest running-in period before a steady-state low-friction effect was obtained. As can be seen in Fig. 2, a steady-state COF was reached after  $\sim 260$  m for the coating deposited with a  $\text{C}_2\text{H}_2$  flow of 100 sccm. This coating presents a total coating thickness of  $8.0 \pm 0.1$   $\mu\text{m}$  and a matt-greyish coloration. Further, it is essentially stoichiometric with a composition of  $\text{Ti}_{52}\text{C}_{26}\text{N}_{21}$  (at%) as determined by ERDA. According to XRD, a fcc crystalline structure (Fm-3 m space group) was obtained with a [111] texture. The measured mechanical properties microhardness and Young's modulus,  $26 \pm 1$  GPa and  $316 \pm 8$  GPa, respectively, slightly exceed the values commonly observed for TiN [23].

### 3.2 Tribological Tests in Different Atmospheres

The recorded COF with sliding distance at RT is shown in Fig. 3a alongside with the cross-sections of the resulting wear scars (Fig. 3b). When testing in ambient air, the COF swiftly reaches a low steady state of 0.14. In contrast to that, the COF increases to 0.5–0.7 for all dry atmospheres (synthetic air,  $\text{N}_2$  and Ar). Surprisingly, the fourfold increase in COF does not necessarily lead to an increase in wear. While the experiments in air (synthetic and ambient) exhibit a comparable wear ( $k_{\text{coating}} \sim 3.8 \cdot 10^{-16} \text{ m}^3\text{N}^{-1}\text{m}^{-1}$ ), a smaller wear scar is noticeable for the test in  $\text{N}_2$  ( $k_{\text{coating}} = 3.2 \cdot 10^{-17} \text{ m}^3\text{N}^{-1}\text{m}^{-1}$ ) and Ar ( $k_{\text{coating}} = 2.5 \cdot 10^{-17} \text{ m}^3\text{N}^{-1}\text{m}^{-1}$ ) (Fig. 3b). As for the counterparts, the test in ambient air resulted in the lowest wear ( $k_{\text{ball}} = 1.4 \cdot 10^{-17} \text{ m}^3\text{N}^{-1}\text{m}^{-1}$ ). These results point towards significantly different wear mechanisms active in the respective atmospheres.

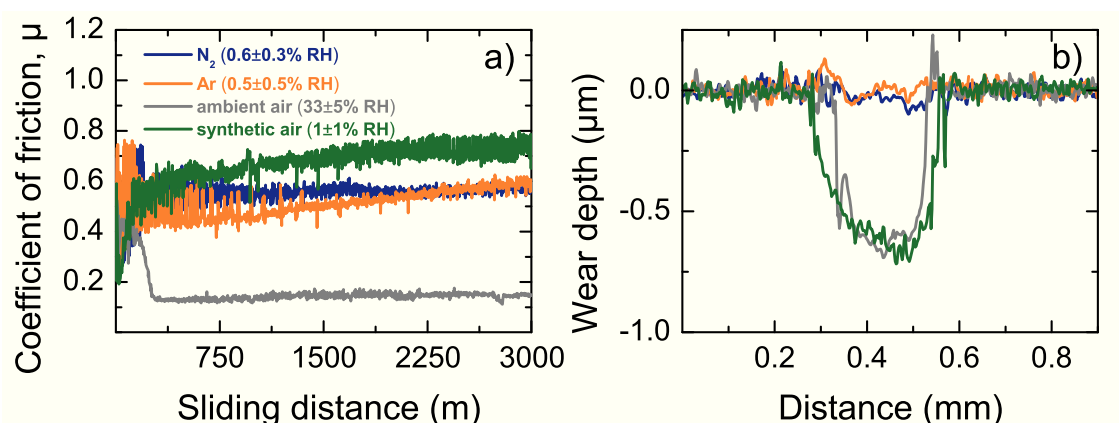


Figure 3: (a) Results of the tribological performance of the selected coating (deposited at a  $C_2H_2$  flow of 100 sccm) in dry  $N_2$ , argon, ambient air, and synthetic air. (b) cross-section of the resulting wear scars

## 4 Discussion

It is widely assumed in literature that the reduction in friction active for carbon containing materials is due to a transformation of the material under the presence of water and/or the subsequent formation of a low-friction tribolayer [16]. Similar to vapour-phase lubrication [24], such processes strongly depend on the partial pressure of the gaseous adsorbate (moisture), available areas for adsorption (active sites on the coating) as well as exposure time to the environment (passing frequency of the counterpart).

### 4.1 Role of Ambient Gas Chemistry

For the tests in Ar,  $N_2$  and synthetic air, no moisture is present inhibiting the low-friction effect. This manifests itself in a dramatically increased COF. Most interestingly, the fourfold increase in COF does not necessarily lead to an increase in wear. Even no wear was observable for the tests in inert gas leading to the conclusion that a sole mechanical wear process does not play a significant role. The comparable wear rates for ambient and synthetic air coinciding with significantly different COFs indicate different chemical wear processes which in case of synthetic air predominantly are oxidative, while under the presence of moisture the water-modified surface layers are removed and partially transferred to the ball presumably as lubricious tribolayer.

### 4.2 Formation and Constitution of the Tribolayers

The common tenor in the literature concerning the tribology of carbon based coatings links the low-friction behaviour to the formation of 3<sup>rd</sup> bodies in the contact and the subsequent formation of lubricious tribo layers. For ceramic  $TiC_{1-x}N_x$ , however, transfer layers were found for all testing atmospheres regardless the occurrence of the low-friction effect. These layers exclusively form on the counterparts as shown in Fig. 4.

This statement is reinforced by Raman spectroscopy analyses of the counterpart wear tracks as shown in Fig. 5. These results were obtained in a preceding study where a com-

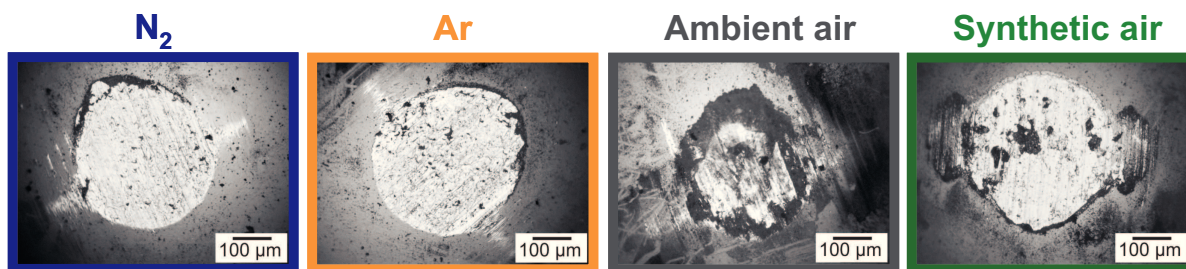


Figure 4: Light optical microscopy imaging of the wear tracks on the alumina counterparts for all the tribological tests performed on the selected coating (deposited at a  $C_2H_2$  flow of 100 sccm) in dry  $N_2$ , argon, ambient air and synthetic air

mercial TiCN coating synthesized under similar conditions but with graded composition has been studied [25]. As imaged in mapping B, bands of amorphous carbon were detected for all dry conditions. Amorphous or highly disordered carbon (i.e., characterized by high D/G intensity ratio, where D and G are disordered and graphite modes of the Raman shift [26]), can be assumed to possess no macroscopic shear system and, therefore, does not provide for a low-friction effect. Instead, the detection of significant fractions of C-H bonds for the low-friction test in ambient air confirms the already known concept in the DLC literature that the adsorption of water saturates dangling bonds. The reduction of friction might therefore be attributed to the liberation and agglomeration of carbon from the  $TiC_{1-x}N_x$  coating by tribochemical processes and the subsequent saturation of dangling bonds. By that, the two counterparts are separated by a low-shear interlayer even for the ceramic  $TiC_{1-x}N_x$  coating.

Surprisingly, the wear rate does not correlate with the recorded COF. The high-friction (COF  $\sim 0.5$ ) tests in inert gas (Ar and  $N_2$ ) result in almost no detectable wear, whereas the by a factor of four lower COF for the test under moist conditions exhibits an accelerated wear which is comparable to the high COF test in synthetic air. Hence, different wear mechanisms must be active. A significant contribution of mechanical wear by, e.g., fatigue under the given conditions can be ruled out from the absence of wear for the high COF inert gas tests. The accelerated wear for the synthetic air test under a similar COF confirms, on the other hand, a significant chemical wear presumably by tribo-oxidation. The same level of wear is observed for the low-friction test under moist conditions inferring that besides oxidation a material consumption by water-modification related processes, most likely the removal of the low-shear interlayer.

## 5 Conclusions

The present study confirms that the low-friction effect of  $TiC_{1-x}N_x$  hard coatings is tightly connected to the presence of atmospheric moisture, as indicated by its absence for ball-on-disc tests against alumina counterparts conducted in dry atmospheres, namely Ar,  $N_2$  as well as synthetic air (relative humidity, 1 %), where high coefficients of friction were observed. Although the formation of a 3<sup>rd</sup> body was observed for all atmospheres, only the formation of C-H bonds as detected by Raman spectroscopy provides for an easy shearable interlayer that is most likely responsible for the low-friction effect. At the same time, the

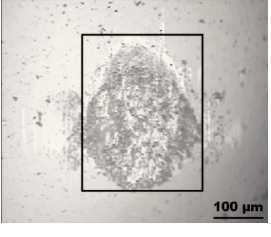



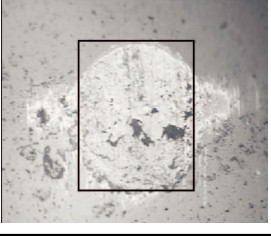
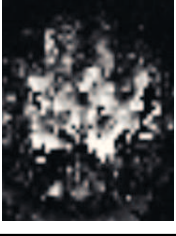


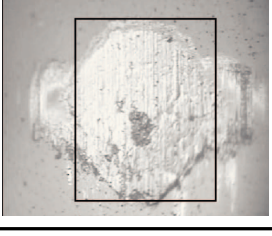

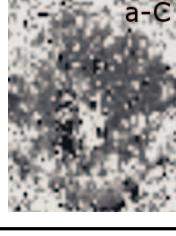

	Optical microscope image	mapping A: transfer layer	mapping B: C-H and a-C	mapping C: TiO <sub>2</sub> and TiCN
ambient air				
dry nitrogen				
synthetic air				

Figure 5: Optical micrographs and Raman mappings of the wear scars on the alumina counterparts after ball-on-disc tests in ambient air, dry nitrogen and synthetic air; Mapping A shows the existence of a transfer layer for all three atmospheres; Mapping B indicates the presence of C-H bonds exclusively for tests in ambient air as well as amorphous carbon for dry nitrogen and synthetic air; Mapping C shows the distribution of transferred unaltered as well as oxidized coating materials [25]

required tribochemical processes lead to an accelerated wear, mainly due to tribo-oxidation and water-based mechanisms. Mechanical wear can be excluded at room temperature as no wear was observed in the inert atmospheres (N<sub>2</sub> and Ar). Still, the precise mechanisms of the complex interplay of liberation, transfer and water-based saturation of carbon in the system Ti-C-N is yet not fully understood, but the established set of experiments provides for a basis for further investigations.

## Acknowledgements

The authors acknowledge Dr. E. Strub, Dr. J. Rörrich and Dr. W. Bohne from the Centre for Ion Beam Techniques of the Hahn-Meitner Institute in Berlin for the ERDA measurements. The financial support by the Christian Doppler Research Association as well as Plansee GmbH (Lechbruck, Germany) and Oerlikon Balzers AG (Balzers, Liechtenstein) is highly acknowledged.

## References

- [1] L. Karlsson, L. Hultman, M. P. Johansson, J. E. Sundgren, and H. Ljungcrantz, *Surf. Coat. Technol.*, 2000, **126**, 1–14.
- [2] A. Forn, J. A. Picas, G. G. Fuentes, and E. Elizalde, *Int. J. Refract. Met. Hard Mater.*, 2001, **19**, 507–513.
- [3] S. J. Bull, D. G. Bhat, and M. H. Staia, *Surf. Coat. Technol.*, 2003, **163-164**, 499–506.
- [4] C. Wei, J. Fin Lin, T.-H. Jiang, and C.-F. Ai, *Thin Solid Films*, 2001, **381**, 94–103.
- [5] E. Bemporad, C. Pecchio, S. De Rossi, and F. Carassiti, *Surf. Coat. Technol.*, 2001, **146-147**, 363–370.
- [6] K. Narasimhan, S. P. Boppana, and D. G. Bhat, *Wear*, 1995, **188**, 123–129.
- [7] J. Andersson, R. A. Erck, and A. Erdemir, *Wear*, 2003, **254**, 1070–1075.
- [8] V. Derflinger, H. Brandle, and H. Zimmermann, *Surf. Coat. Technol.*, 1999, **113**, 286–292.
- [9] M. A. Gomez, J. Romero, A. Lousa, and J. Esteve, *Surf. Coat. Technol.*, 2005, **200**, 1819–1824.
- [10] J. A. Heimberg, K. J. Wahl, I. L. Singer, and A. Erdemir, *Appl. Phys. Lett.*, 2001, **78**, 2449–2451.
- [11] J. Andersson, R. A. Erck, and A. Erdemir, *Surf. Coat. Technol.*, 2003, **163-164**, 535–540.
- [12] A. Erdemir, M. Switala, R. Wei, and P. Wilbur, *Surf. Coat. Technol.*, 1991, **50**, 17–23.
- [13] H. Ronkainen, S. Varjus, J. Koskinen, and K. Holmberg, *Wear*, 2001, **249**, 260–266.
- [14] J. Takadoum, H. H. Bennani, and M. Allouard, *Surf. Coat. Technol.*, 1997, **88**, 232–238.
- [15] I. Singer and K. Wahl, MRS Workshop Series: Tribology on the 300th Anniversary of Amonton’s Law, 1999.
- [16] Y. Liu, A. Erdemir, and E. I. Meletis, *Surf. Coat. Technol.*, 1996, **82**, 48–56.
- [17] A. Erdemir and C. Donnet, *J. Phys. D: Appl. Phys.*, 2006, **39**, R311–R327.
- [18] S. W. Huang, M. W. Ng, M. Samandi, and M. Brandt, *Wear*, 2002, **252**, 566–579.
- [19] T. Polcar, R. Novak, and P. Siroky, *Wear*, 2006, **260**, 40–49.
- [20] J. Neidhardt, Z. Czigány, B. Sartory, R. Tessadri, M. O’Sullivan, and C. Mitterer, *Acta Mater.*, 2006, **54**, 4193–4200.
- [21] E. Rabinowicz, *Friction and Wear of Materials*, John Wiley, New York, 1964.
- [23] J. Neidhardt, M. O’Sullivan, A. Reiter, W. Rechberger, W. Grogger, and C. Mitterer, *Surf. Coat. Technol.*, 2006, **201**, 2553–2559.
- [24] W. G. Sawyer and T. A. Blanchet, *Journal of Tribology*, 2001, **123**, 572–581.
- [25] M. Rebelo de Figueiredo, J. Neidhardt, R. Kaindl, A. Reiter, R. Tessadri, and C. Mitterer, *Wear*, 2008, **265**, 525–532.

- [26] J. Robertson, *Mater Sci Eng, R*, 2002, **37**, 129–281.





# Publication IV

In situ studies of  $\text{TiC}_{1-x}\text{N}_x$  hard coating tribology

M. Rebelo de Figueiredo, C. Muratore, R. Franz, R.R. Chromik,  
K.J. Wahl, A.A. Voevodin, M. O'Sullivan, M. Lechthaler,  
C. Mitterer

Tribology Letters **40(3)** 365–373 (2010)



# In situ studies of $\text{TiC}_{1-x}\text{N}_x$ hard coating tribology

M. Rebelo de Figueiredo<sup>a</sup>, C. Muratore<sup>b</sup>, R. Franz<sup>a</sup>, R.R. Chromik<sup>c</sup>, K.J. Wahl<sup>d</sup>, A.A. Voevodin<sup>b</sup>, M. O'Sullivan<sup>e</sup>, M. Lechthaler<sup>f</sup>, C. Mitterer<sup>a</sup>

<sup>a</sup>Christian Doppler Laboratory for Advanced Hard Coatings, Department of Physical Metallurgy and Materials Testing, University of Leoben, Franz-Josef-Strasse 18, 8700 Leoben, Austria

<sup>b</sup>Air Force Research Laboratory, Materials and Manufacturing Directorate, Wright Patterson Air Force Base, OH 45433-7750, USA

<sup>c</sup>Department of Mining and Materials Engineering, McGill University, 3610 University Street, Montreal, QC, Canada

<sup>d</sup>Chemistry Division, Molecular Interfaces and Tribology Section, Code 6176, U.S. Naval Research Laboratory, Washington, DC 20375-5342, USA

<sup>e</sup>PLANSEE Composite Materials GmbH, Siebenburgerstrasse 23, 86983 Lechbruck am See, Germany

<sup>f</sup>OC Oerlikon Balzers AG, Iramali 18, FL-9496 Balzers, Principality of Liechtenstein

Abstract  $\text{TiC}_{1-x}\text{N}_x$  hard coatings present time-dependent tribological behavior with an initial running-in period (500–2000 cycles) marked by an elevated friction coefficient, followed by >10000 cycles with low-friction and wear at room temperature (RT) in ambient air. The mechanisms behind this behavior are not completely understood. Tribological tests performed at RT and at different relative humidity (RH) levels revealed that a minimum value between 15 and 25% RH is needed to trigger the low-friction regime at a sliding speed of  $100 \text{ mm s}^{-1}$ . By in situ observations of transfer film growth, it could be observed that third body material is formed during this running-in period by plowing of the coating and shearing of the removed material. The appearance and thickening of the transfer film marks the beginning of the steady-state low-friction regime where the velocity is accommodated by interfacial sliding. At this stage in the tribological test, the recorded Raman spectra indicated the presence of C–H bonds in the wear track. Use of in situ analytical tools during wear tests provided insights with respect to tribological phenomena that were not available by conventional, post-mortem analysis methods.

**Keywords:** TiCN · Low-friction · In situ tribometry · Tribofilm

## 1 Introduction

Dry machining leads to a considerable reduction in waste materials and remains a significant goal in environmentally conscious manufacturing. One of the most promising routes to achieve this objective is through self-lubrication of tool surfaces coated with materials such as  $\text{TiC}_{1-x}\text{N}_x$  [1, 2]. From the literature it is already known that, similar to other carbon containing coatings [3–6],  $\text{TiC}_{1-x}\text{N}_x$  presents low-friction behavior [7] under typical ambient conditions (room temperature and >20% humidity). It is also known that carbon strongly determines the tribological properties in these compound thin films; however, the lubrication mechanisms are likely to differ from diamond-like carbon (DLC) coatings, which are composed primarily of carbon [8, 9]. Systems such as  $\text{TiC}_{1-x}\text{N}_x$  with less carbon incorporated in the lattice are, in comparison to DLC, poorly understood, and require further investigation.

Earlier experiments with  $\text{TiC}_{1-x}\text{N}_x$  coatings with  $x$  varied from 0.25 to 0.75 had indicated that there was a reduction of the friction coefficient from initial 0.9 to about 0.5 during initial sliding against steel at 50% humidity conditions; however, it was not until amorphous carbon was added to the coating composition that the friction coefficient was reduced to 0.2 [10]. Recent studies of  $\text{Al}_2\text{O}_3$  sliding on  $\text{TiC}_{1-x}\text{N}_x$  films revealed that the formation of a transfer layer rich in C–H bonds, as detected by Raman spectroscopy, was necessary for low-friction [7]. This result suggested the liberation and agglomeration of carbon by tribochemical processes and the subsequent saturation of dangling carbon bonds at the contact interface by

adsorption of water vapor, weakened adhesive forces at the mechanical contact and resulted in lower friction.

In this work, tribological tests on  $\text{TiC}_{1-x}\text{N}_x$  films were performed in different levels of relative humidity (RH) at room temperature (RT) in order to find the level of humidity required for the low-friction behavior. By employing *ex situ* Raman analysis on the wear scars of the coating and counterpart, the dependence of the composition and structure of the contact interface on the atmosphere was studied. Further, *in situ* optical and spectroscopic techniques [11] were used to study the running-in period of  $\text{TiC}_{1-x}\text{N}_x$  films in humid air to reveal formation mechanisms of the friction-reducing tribofilm present at sufficiently high levels of humidity, and to correlate its composition and thickness in the contact area to the measured friction coefficient values in real time.

## 2 Experimental Details

The  $\text{TiC}_{1-x}\text{N}_x$  coating was prepared by dc magnetron sputtering of a  $\text{Ti}_2\text{CN}$  compound target in an industrial-scale plant (Oerlikon Balzers Innova) with a residual pressure of less than  $10^{-3}$  Pa. The high-speed steel (HSS, AISI M2 type) coupons ( $\varnothing$  25.4 mm) used as substrates were ground and diamond polished to a 3  $\mu\text{m}$  finish after quenching and tempering to a hardness of 65 HRC. Prior to deposition the samples were cleaned in an ultrasonic bath using ethanol. The samples were heated to 500 °C and Ar ion etched for approximately 30 min utilizing a secondary gas discharge. The  $\text{TiC}_{1-x}\text{N}_x$  film was sputtered with an Ar flow of 650 sccm corresponding to a 2.1 Pa total pressure as controlled by a capacitive gauge, forming a coating with a thickness of approximately 2.8  $\mu\text{m}$ , as determined by ball-cratering. X-ray diffraction (XRD) data for analyzing the crystal structure were obtained by a Bruker AXS D8 Advance diffractometer with parallel beam geometry equipped with a Cu-ceramic tube and an energy-dispersive detector (SolX from Bruker AXS) with a grazing incidence of 2°. Hardness measurements according to Oliver and Pharr [12] were conducted using a UMIS nanoindenter equipped with a Berkovich tip applying a maximum load ranging from 3 to 20 mN. The composition of the coating was investigated by elastic recoil detection analysis (ERDA). The compositional depth profile of the coating was determined by a primary beam of 35 MeV Cl ions. The forward scattered coating atoms were analyzed using a detection system with a solid angle of 0.4 msr and a large detection angle of 60°, which enables simultaneous detection of all elements.

For the investigations of steady-state friction, a ball-on-disc tribometer housed inside a sealed chamber with computerized temperature and humidity control was used. The temperature was fixed at 22 °C, as measured by a calibrated thermocouple, and tests were conducted in four different ambient atmospheres (0, 15, 25, and 40% RH), as measured by a digital hygrometer with an error of  $\pm 2\%$  (absolute). In order to remove ambient gas, the interior of the chamber was purged with dry  $\text{N}_2$  (and  $\text{H}_2\text{O}$  vapor) and allowed to equilibrate at the selected test conditions for 30 min prior to initiation of each wear test.  $\text{Al}_2\text{O}_3$  balls were used as counterparts in all sliding tests (purity of 99.8% and  $\varnothing$  6 mm). A normal load of 2 N (with an average Hertzian contact stress of 1 GPa), a sliding speed of 100  $\text{mm s}^{-1}$  and 15,000 cycles sliding distance were set as standard parameters. An additional test at 40% RH was conducted in the presence of a Raman spectroscopy probe that allowed focusing of a 514 nm excitation laser on the wear track (Fig. 1a) during wear tests. The same probe

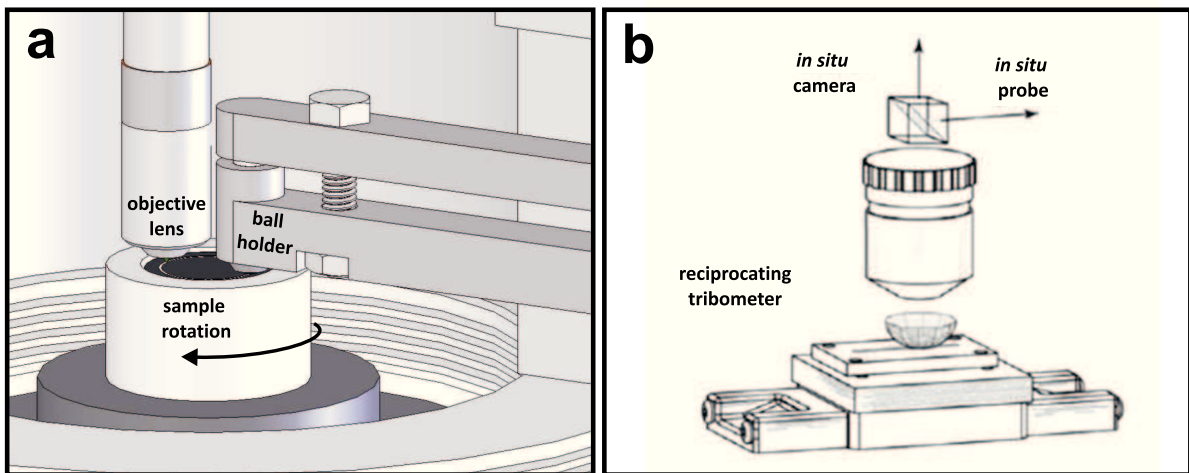


Figure 1: Experimental set-up of the in situ apparatuses for the tribological investigations: a for optical observations of the transfer film and b for Raman spectroscopic analysis (reprinted with permission from [11])

was also used to collect the scattered light for analysis by the Raman spectrometer (Fig. 1a) as it was dispersed by a holographic grating with 300 grooves/mm and then collected by a  $1024 \times 256$  open electrode CCD detector. Spectra were recorded unpolarized in the spectral range  $0\text{--}3500\text{ cm}^{-1}$  as described in detail in Ref. [13] at intervals of approximately 500 sliding cycles. The laser spot on the surface had a diameter of approximately  $1\text{ }\mu\text{m}$  and a maximum power of 0.5 mW, which was low enough to prevent sample damage due to local temperature increases during analysis. Ex situ Raman spectra of the wear scars on the coating and counterpart as well as the wear debris were recorded after the above mentioned tribological tests in different RH levels, using the same Raman spectrometer used for in situ experiments.

Additional in situ investigations of transfer film formation were performed on a custom-built tribometer (Fig. 1b) designed to perform reciprocating sliding wear tests with a hemispherical counterface ( $\varnothing 6\text{ mm}$ ). This instrument, described in detail elsewhere [14–19], allows for the direct visual observation of the sliding contact through the transparent counterface. Through analysis of the test video, velocity accommodation modes [20] may be identified and the transfer film thickness can be measured by Newton's ring technique during sliding [19]. For these experiments, the load applied to the counterface was 1.6 N. Reciprocating sliding at  $1\text{ mm s}^{-1}$  was conducted over a 4 mm track length for 1600 cycles. Tests were run at humidity conditions of 35–45% RH. Images from the video were analyzed to determine the transfer film thickness with standard photo-editing software, with the length scale determined from observation of a 0.01 mm calibration scale. For wear tracks and transfer films generated from this tribometer, post-analysis was carried out with a Renishaw inVia Raman spectrometer equipped with a 514.5 nm  $\text{Ar}^+$  laser. Spectral acquisition was carried out for Raman shifts between 200 and  $3200\text{ cm}^{-1}$ .

The wear volume of the coatings was evaluated by an optical 3D white light profiling system (Wyko NT 1000) and the wear coefficients were calculated as the ratio between the volume and applied load times sliding distance [21].

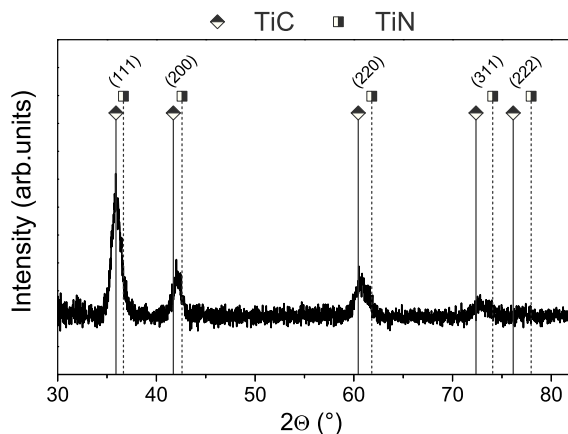


Figure 2: XRD pattern from the coating sample

## 3 Results and Discussion

### 3.1 Coating Characterization

The coatings had a thickness of  $\sim 2.8 \mu\text{m}$ , with a shiny silver-gray coloration. According to performed Rockwell C indentation tests, the coatings were well-adherent to the substrates as they show no delamination near the edge of the indent. However, the appearance of a circumferential crack to accommodate the deformation points towards a brittle nature of the deposited TiCN coatings. The chemical composition of the coating was analyzed by ERDA and revealed a stoichiometric composition of  $\text{Ti}_{50.4}\text{C}_{26.8}\text{N}_{22.8}$ , roughly mirroring the target composition. According to the XRD pattern in Fig. 2, a face-centered cubic crystalline structure ( $Fm-3m$  space group) was obtained with a [111] texture. The peak positions are located between those predicted for TiC and TiN, indicating the presence of a solid solution with an intermediate lattice parameter. This result is consistent with literature reports on a gradual  $\text{TiC}_{1-x}\text{N}_x$  crystal lattice expansion from that of TiN to that of TiC with an increase of the carbon content, which also results in lattice straining for mixed C/N compositions [22]. The hardness and Young's modulus of  $\sim 46$  and  $\sim 511$  GPa, respectively, obtained by nanoindentation were higher than the typical values in literature [23] but comparable to values by Karlsson et al. [1]. The high hardness might be due to hindering of dislocation movements by lattice strain when the carbon content increases.

### 3.2 Investigations on the Steady-State Friction

The development of the friction curves and wear depths with sliding distance in different relative humidity atmospheres (0, 15, 25, and 40% RH) is shown in Fig. 3-3. From the analyses of the friction curves, the steady-state coefficient of friction (COF) decreased with increasing relative humidity. The test at 0% RH showed a slightly increasing COF after 1500 cycles that reaches a value of 0.65 at the end of the test. This COF is lower as compared to the value obtained for an arc-evaporated TiCN (COF  $\sim 0.9$ ) tested under the same conditions [7]. The difference between both COF's might result from the higher roughness of the arced TiCN whereas the slight increase might be due to the presence of a small fraction of residual

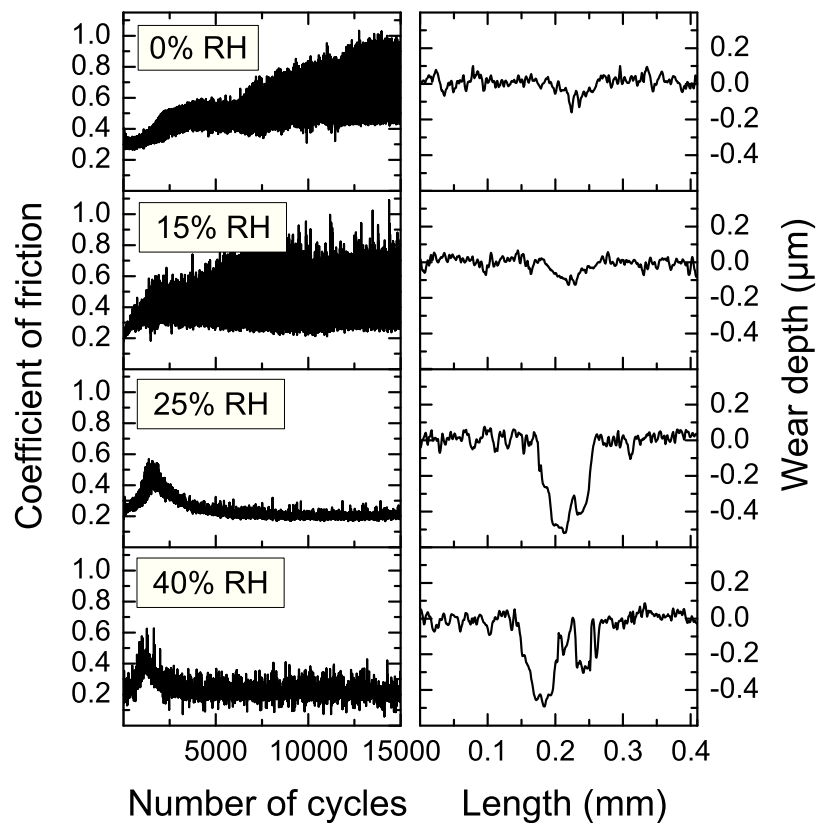


Figure 3: Friction curves and wear tracks of the tribological tests performed in atmospheres with different relative humidity levels (0, 15, 25, and 40%)

water vapor considering the error of the used hygrometer. Increasing the RH level to 15%, a similar situation is encountered as the COF was only slightly reduced to a value of 0.5. A major reduction in friction was obtained in the atmospheres with 25 and 40% RH, where the steady-state COF decreased to 0.2. At 0 and 15% RH no significant abrasive wear was observed on the coating, only a smoothening (polishing) of the surface (see Fig. 3). Thus both calculated wear rates were similar and remained approximately constant at  $\sim 3.1 \times 10^{-18} \text{ m}^3 \text{ N}^{-1} \text{ cycle}^{-1}$ . In the atmospheres with higher RH (i.e., 25 and 40%), moderate wear was measured, with an average wear rate of  $\sim 1.2 \times 10^{-17} \text{ m}^3 \text{ N}^{-1} \text{ cycle}^{-1}$ .

From the analysis described above, it is apparent that a change in the ambient atmosphere resulted in a significant change of the active friction and wear mechanisms during sliding. Previous studies on the temperature dependence of low-friction behavior for  $\text{TiC}_{1-x}\text{N}_x$  coatings suggested that humidity was essential for friction reduction [7]. The tests within the present work identify that the level of humidity necessary to trigger the low-friction effect under the specified conditions is between 15 and 25% RH. The wear rate of the coating also strongly depends on the surrounding atmosphere. Figure 3 shows that moderate wear is observed at humidity levels high enough to induce a friction reduction (25 and 40% RH), suggesting a combination of physical and chemical processes in the tribological contact generating a lubricious interface in the contact area during sliding. The increased wear rate at high humidity indicates that this lubricious interface was formed at the expense of the

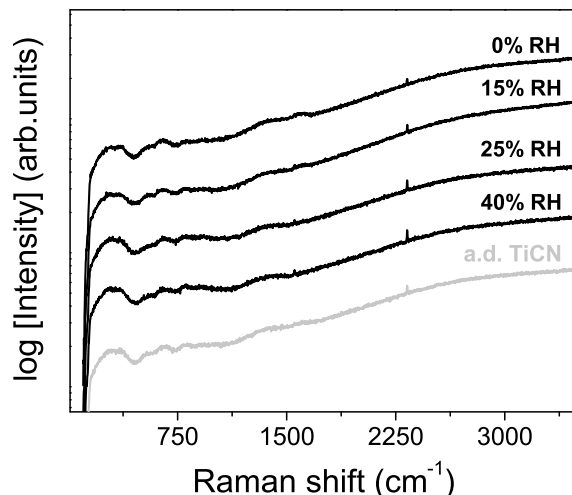


Figure 4: Raman spectra of the wear tracks on the coatings for all investigated relative humidity levels. As-deposited (a.d.) TiCN is shown as a reference

coating material in the wear track.

Subsequent to the ball-on-disc tests, *ex situ* analyses by Raman spectroscopy were performed in order to gain information regarding the chemical compounds present in the contact zone. Measurements on the wear scar and the wear debris on the coating as well as on the  $\text{Al}_2\text{O}_3$  counterparts were performed (Figs. 4, 5, and 6). The spectra taken within the coating wear track were similar to those measured for the pristine  $\text{TiC}_{1-x}\text{N}_x$  coating surface (see Fig. 4). They exhibited two broad and split bands at low wave numbers ( $\sim 300$ ,  $\sim 600$   $\text{cm}^{-1}$ ), indicating that no altered material was found on the wear tracks, regardless of the testing atmosphere. Concerning the wear debris (Fig. 5) for all the testing atmospheres, relative broad bands at around 1350 and 1580  $\text{cm}^{-1}$  were detected. These bands, which were more pronounced for the tests at lower RH, are the D- and G-band characteristic of amorphous carbon [24]. The spectra recorded on the counterpart wear scars show a similar trend as evidenced in Fig. 6, where the presence of amorphous carbon was strongest at 0% RH. In addition to the D- and G-band, a Raman band at around 420  $\text{cm}^{-1}$ , which is attributed to  $\text{Al}_2\text{O}_3$  [7], was detected. At 15% RH the amorphous carbon signal was still present, but also bands at around 200, 450, and 550  $\text{cm}^{-1}$  were detected and are associated to the presence of rutile [25]. However, for the tests performed at 25 and 40% RH the signal of the D- and G-band disappeared and a band in the region between 2800 and 3100  $\text{cm}^{-1}$  was detected, indicating the presence of C–H bonds [26].

Similar to the results observed in Ref. [7], the transfer film adhered to the counterpart for tests conducted in all atmospheres; however, the composition of the transfer films was dependent upon the relative humidity. The appearance of the Raman band between 2800 and 3100  $\text{cm}^{-1}$  indicating the presence of C–H bonds coincides with the reduction of the steady-state COF from the increase in ambient RH from 15 to 25%, identifying the necessity for sufficient water vapor to activate the low-friction behavior observed after the running-in period. On the other hand, the amorphous carbon found on the counterpart for low values of RH apparently did not provide for lubricious effects. This was not surprising, as



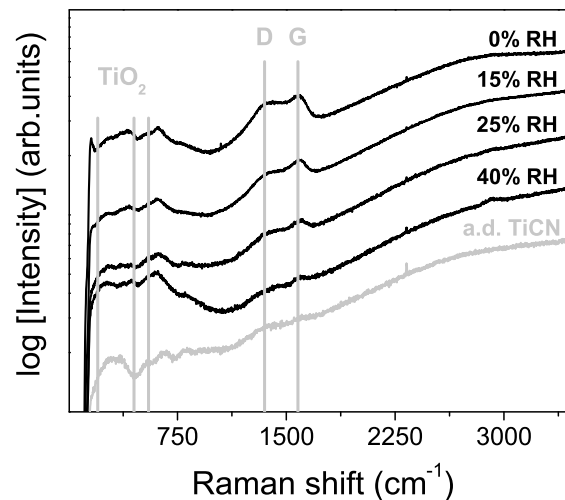


Figure 5: Raman spectra of the wear debris for all investigated relative humidity levels. As-deposited (a.d.) TiCN is shown as a reference. D- and G-band peak positions of amorphous carbon are indicated

un-terminated carbon bonds result in adhesion to contacting surfaces and relatively high-friction coefficients. While the friction was high at values of  $RH \leq 15\%$ , the wear rate was low due to the hardness of the coating material.

### 3.3 Investigations on the Running-in Period

Despite the clear relationships between wear phenomena and ambient environment demonstrated by the data in Figs. 4, 5, and 6 and explained in the accompanying discussion above, several questions remain: (i) how does this lubricious C–H transfer film form, (ii) what role does the running-in process play in its formation, and (iii) where exactly does sliding occur throughout the test? It was also not clear why the hydrogenated carbon spectra from the transfer films developed in high humidity tests did not appear in the post-test analysis of the wear debris. To explore these questions, in situ analysis of the sliding contact architecture and chemistry of the contact interface during wear testing was conducted.

#### 3.3.1 In Situ Observation of Transfer Film Formation

As shown in Fig. 7, the running-in period with higher friction as compared to the steady-state COF lasts for roughly 400 cycles. Note that in this case reciprocating sliding was used at a much lower sliding velocity ( $1 \text{ mm s}^{-1}$ ) than in the ball-on-disc tests ( $100 \text{ mm s}^{-1}$ ) in the previous section. The low-friction effect is still present, but the steady-state regime is reached quickly, perhaps because at the lower sliding velocity the individual asperity contact flash temperatures are reduced, reducing water desorption rates and the contact surface is exposed to the ambient atmosphere for a longer time period allowing for more effective interactions with water vapor on the surface between sliding cycles. Dependence of tribological phenomena on sliding speed in reactive atmospheres due to adsorption kinetics on surfaces has been shown for these [7] and other carbon-based materials [27].

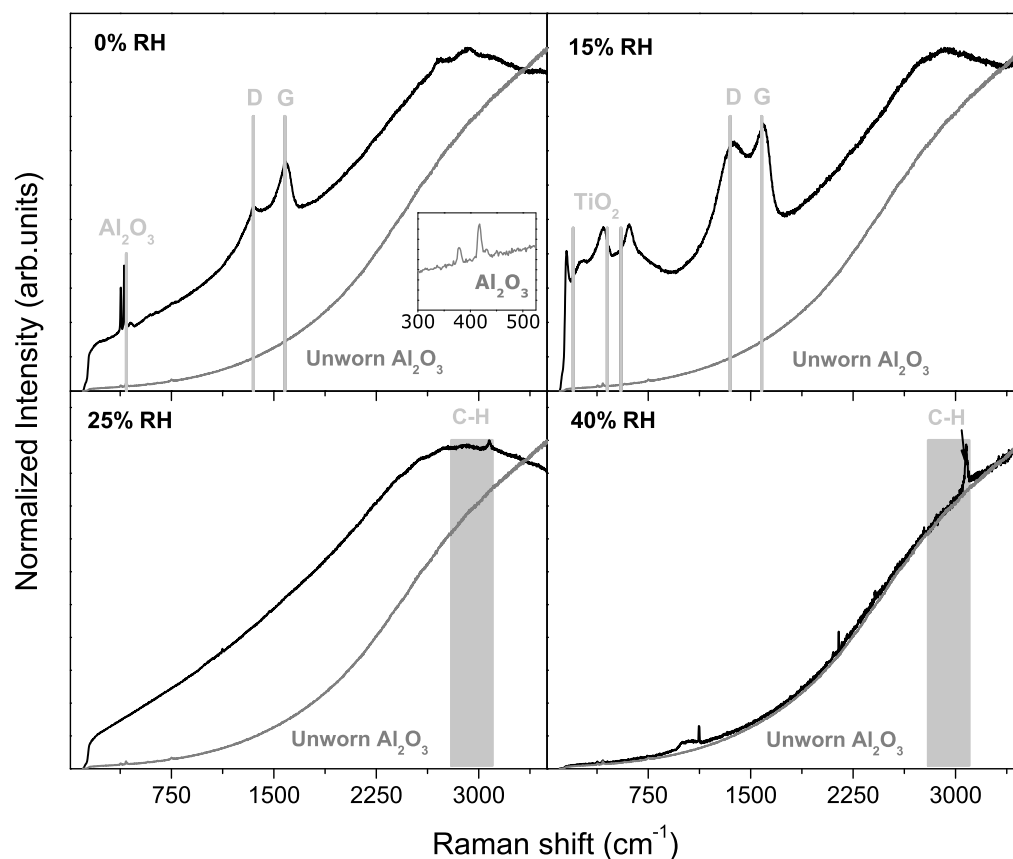


Figure 6: Raman spectra of the wear scars on the  $\text{Al}_2\text{O}_3$  counterparts for all investigated relative humidity levels. Spectra obtained from unworn  $\text{Al}_2\text{O}_3$  are shown as reference. Relevant peak positions are indicated

Comparing the COF observations with in situ measurements of transfer film thickness (Fig. 7), a correlation was found between the reduction of the COF after the initial running-in peak and the thickening of transfer film material adherent to the  $\text{Al}_2\text{O}_3$  counterface. During the running-in period, essentially no transfer film is observed. Only when the COF reaches the steady-state value, a transfer film with a thickness of 40 nm can be observed. As the tribological test proceeds, the transfer film thickness increases to 60–80 nm at the end of the test.

The generation and thickening of a transfer film is also evident in the test video still images in Fig. 8. During the running-in period, the contact region is clear of debris and transfer film material. The appearance of transfer film material occurs as the COF drops. In addition to the transfer film thickness calculation, the velocity accommodation modes can also be derived from the observation of the video, where it is evident that the process for transfer film formation appears to be a combination of plowing of the coating and shearing of the plowed material. These processes create, deform, and eventually attach third body material to the counterface. The motion within the contact largely stops when the friction becomes stable. From this point forward, the velocity accommodation mode is interfacial sliding of transfer film material against the wear track.

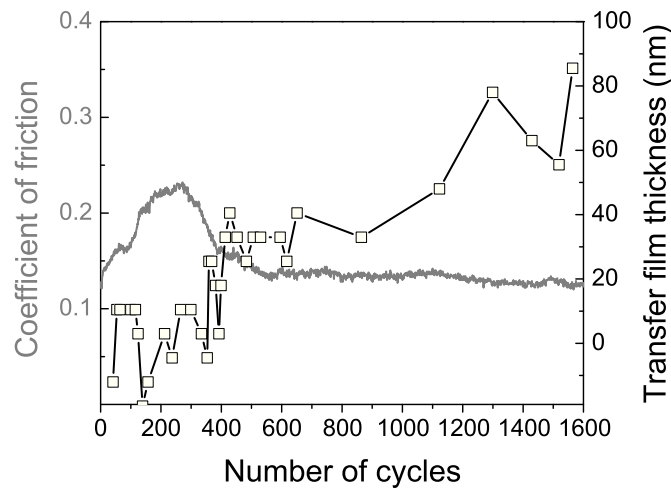


Figure 7: Coefficient of friction and transfer film thickness plotted versus the number of cycles for the reciprocating sliding test performed in an atmosphere with 35–45% RH

Post-analysis with Raman spectroscopy of wear track and wear debris on the coating and transfer layer on the ball as shown in Fig. 9 is consistent with the previously mentioned Raman analysis (see Figs. 4, 5, and 6). The spectrum recorded on the wear track revealed the presence of unaltered coating material, whereas the wear debris contains rutile and amorphous carbon. A peak in the range  $2800\text{--}3100\text{ cm}^{-1}$  evidencing the presence of C–H was only found for the transfer layer. These results in combination with the observations on the velocity accommodation mode suggest that sliding occurs between C–H compounds present in the transfer film and the TiCN coating in the wear track.

### 3.3.2 In Situ Raman Analysis on the Coating Wear Track

The in situ Raman spectra taken at selected cycles during the additional 40% RH tribological test are shown as insets in Fig. 10. The spectrum obtained at the beginning of the test (i.e., at 0 cycles) shows low intensity peaks characteristic for D- ( $1380\text{ cm}^{-1}$ ) and G-band ( $1580\text{ cm}^{-1}$ ) of carbon. These bands are still present at 515 cycles, which marks the beginning of the running-in period (COF  $\sim 0.24$ ), and later at 1000 cycles (COF  $\sim 0.33$ ). The situation changes at 2076 cycles, towards the end of the running-in period, where the COF has decreased to

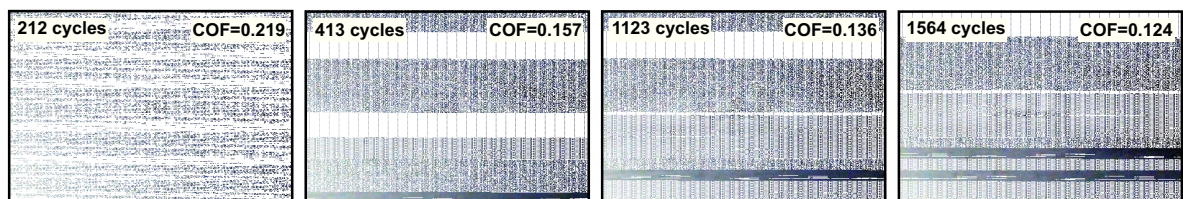


Figure 8: Still images from the in situ video made for the test performed in an atmosphere with 35–45% RH after different number of cycles

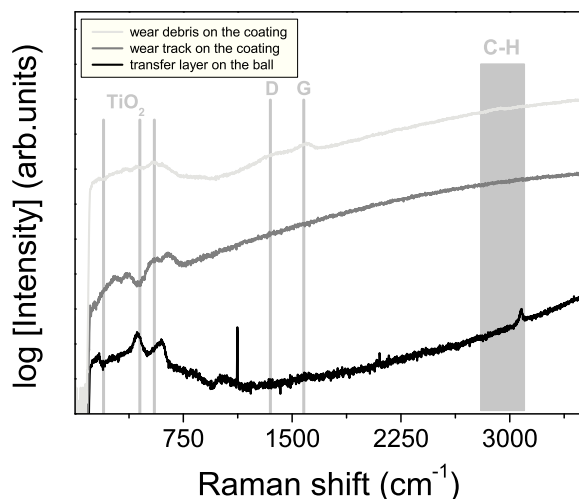


Figure 9: Raman spectra of wear track and wear debris on the coating and of wear scar on the sapphire hemisphere after reciprocating sliding test in an atmosphere with 35–45% RH

$\sim 0.25$ . In this region the signals for the D- and G-band disappear and only a band within the range between 2800 and 3100  $\text{cm}^{-1}$ , characteristic for C–H bonds [26], is measured. After 2076 cycles, friction decreases to a value of  $\sim 0.18$  and remains constant, as does the Raman signature for the C–H bonds, until the end of the test (15,000 cycles). No evidence of amorphous carbon is noticed, only the vibration in the range 2800–3100  $\text{cm}^{-1}$ , originating from C–H bonds.

In general, the intensity of the Raman bands in Fig. 10 is low, but their presence was recorded on all spectra generated over the whole test after approximately every 500 cycles from cycles 2076–15,000, and are therefore not attributed to background noise, but rather, they indicate the presence of hydrogenated carbon in the wear track. As shown in the previous section by ex situ analysis of the contacting surfaces, the transfer film formed during the tribological test (at RT and in an atmosphere with 25% RH or higher) adhered strongly to the counterpart, and no hydrogenated carbon peaks were present in the analysis of wear debris (Fig. 5). It is likely that this hydrogenated carbon peak was absent in the ex situ analysis because that analysis is confined to a single spot, whereas the in situ analysis conducted during the wear test provides a spectrum averaged over the entire wear track during the test, and likely detected particles of transfer film ejected from the mass adhered to the counterpart as the film maintained its steady-state thickness during wear. This hypothesis is supported by the appearance of the Raman peak between 2800 and 3100  $\text{cm}^{-1}$  shown in Fig. 10, which coincides with the relative position on the friction trace indicating transfer film growth in Fig. 8, where the formation of an appreciable thickness marks the beginning of the low steady-state friction coefficient. The detection of the C–H bonds during this stage of the tribological tests is therefore in agreement with the findings from ex situ analysis of the contacting surfaces in the previous section.

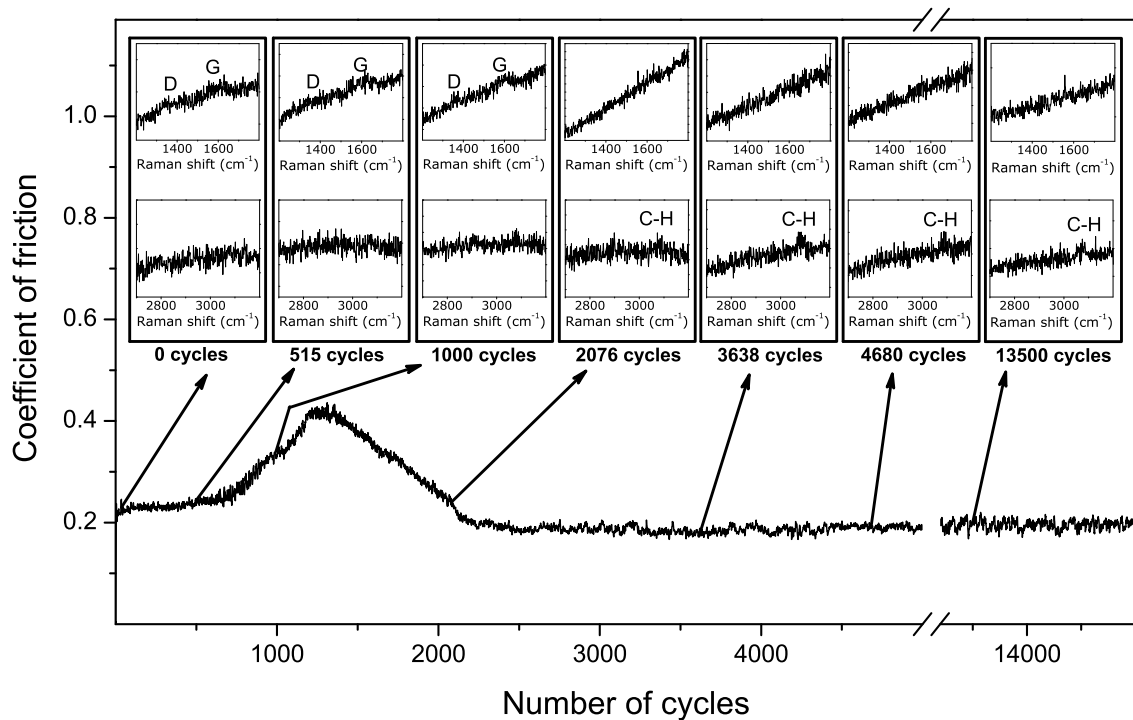


Figure 10: Coefficient of friction versus number of cycles from tribological test in an atmosphere with  $>25\%$  RH. Spectra from in situ Raman spectroscopy measurements at different stages of the test are shown as *insets*

### 3.3.3 Additional Insights Suggested by In Situ Analysis

Earlier, questions about transfer film formation were raised by ex situ analysis. In situ observation of transfer film formation answered some questions about the role of the running-in period in transfer film formation as the combination of abrasion (giving rise to high-friction) and subsequent shearing of hydrogenated carbon material identified in ex situ Raman analysis to obtain a useful volume of slippery material at the contact interface. The in situ Raman experiments revealed the transfer film composition in real time, and also suggested an answer to the question about where sliding takes place (i.e., between the C–H transfer film and  $\text{TiC}_{1-x}\text{N}_x$  surface).

Certainly, these two complementary techniques could be used simultaneously during the same test to portray this comprehensive picture of lubrication mechanisms in any study of tribological contacts in solid/solid films, although, questions with respect to the coating wear rate still remain: (i) what happens to the coating morphology during the running-in and (ii) is the wear rate linear, or does most wear occur during the running-in period? Tests such as those conducted by Wahl and colleagues [28, 29] with analysis of multiple wear tracks or those of Hamilton et al. [30] where in situ profilometry measurements of coating surfaces during wear tests were performed, will be necessary to answer this question. The current study clearly demonstrates that carbon is being released out of the  $\text{TiC}_{1-x}\text{N}_x$  lattice and forms a C–H transfer film at high humidity conditions. A possible mechanism for this phenomenon is

tribochemical oxidation at the individual asperity contacts of  $\text{TiC}_{1-x}\text{N}_x$  by forming  $\text{TiO}_2$  and release of amorphous carbon. An alternative could be decomposition of the  $\text{TiC}_{1-x}\text{N}_x$  solid solution into TiN and an amorphous carbon composite at the contact interface. Combining focused ion beam (FIB) milling with high-resolution transmission electron microscopy of worn surfaces performed by ex situ FIB milling [31] or in situ as by Hu et al. [32] may be used to study structural or compositional changes to the interface during sliding contact.

Certainly, tribological studies employing combinations of in situ analytical techniques such as these described here, will more completely reveal the interfacial phenomena at these and other solid-solid interfaces to provide unprecedented insights on mechanisms describing observations during wear testing.

## 4 Conclusions

For tribological dry sliding investigations in controlled atmospheres with different relative humidity levels, a  $\text{TiC}_{1-x}\text{N}_x$  coating was deposited from a compound target by dc magnetron sputtering. A combination of ex situ and in situ analysis methods revealed the following results:

- The onset point for the low-friction regime with coefficients of friction as low as 0.2 is at atmospheres with relative humidity levels between 15 and 25%.
- A transfer film is formed by abrasion of the coating and shearing of the removed material during the high-friction component of the running-in period. The appearance and thickening of this transfer film marks the beginning of the steady-state regime with a low coefficient of friction.
- The velocity accommodation mode present during this steady-state, low-friction regime of the friction trace is interfacial sliding between the transfer film and the coating.
- In situ Raman analyses performed on the coating wear track revealed that the appearance of C–H bonds coincides with the beginning of this steady-state low-friction regime and the build-up of transfer film.

**Acknowledgement** Financial support by the Christian Doppler Research Association is highly acknowledged. K. J. Wahl was supported by the Office of Naval Research.

## References

- [1] L. Karlsson, L. Hultman, M. P. Johansson, J. E. Sundgren, and H. Ljungcrantz, *Surf. Coat. Technol.*, 2000, **126**, 1–14.
- [2] A. Forn, J. A. Picas, G. G. Fuentes, and E. Elizalde, *Int. J. Refract. Met. Hard Mater.*, 2001, **19**, 507–513.
- [3] J. Andersson, R. A. Erck, and A. Erdemir, *Wear*, 2003, **254**, 1070–1075.
- [4] M. A. Gomez, J. Romero, A. Lousa, and J. Esteve, *Surf. Coat. Technol.*, 2005, **200**, 1819–1824.

- [5] V. Derflinger, H. Brandle, and H. Zimmermann, *Surf. Coat. Technol.*, 1999, **113**, 286–292.
- [6] J. Andersson, R. A. Erck, and A. Erdemir, *Surf. Coat. Technol.*, 2003, **163–164**, 535–540.
- [7] M. Rebelo de Figueiredo, J. Neidhardt, R. Kaindl, A. Reiter, R. Tessadri, and C. Mitterer, *Wear*, 2008, **265**, 525–532.
- [8] Y. Liu, A. Erdemir, and E. I. Meletis, *Surf. Coat. Technol.*, 1996, **82**, 48–56.
- [9] A. Grill, *Surf. Coat. Technol.*, 1997, **94–95**, 507–513.
- [10] A. A. Voevodin, C. Rebholz, J. M. Schneider, P. Stevenson, and A. Matthews, *Surf. Coat. Technol.*, 1995, **73**, 185–197.
- [11] K. J. Wahl and W. G. Sawyer, *MRS Bull*, 2008, **33**, 1159–1167.
- [12] W. C. Oliver and G. M. Pharr, *J. Mater. Res.*, 1992, **7**, 1564–1580.
- [13] C. Muratore, J. Bultman, S. A. Aouadi, and A. Voevodin, *Wear*, 2010, in press.
- [14] R. R. Chromik, C. C. Baker, A. A. Voevodin, and K. J. Wahl, *Wear*, 2007, **262**, 1239–1252.
- [15] R. R. Chromik, A. L. Winfrey, J. Lning, R. J. Nemanich, and K. J. Wahl, *Wear*, 2008, **265**, 477–489.
- [16] S. D. Dvorak, K. J. Wahl, and I. L. Singer, *Tribol. Lett.*, 2007, **28**, 263–274.
- [17] T. W. Scharf and I. L. Singer, *Tribol. Trans.*, 2002, **45**, 363–371.
- [18] I. L. Singer, S. D. Dvorak, K. J. Wahl, and T. W. Scharf, *J. Vac. Sci. Technol. A*, 2003, **21**, 232–240.
- [19] K. J. Wahl, R. R. Chromik, and G. Y. Lee, *Wear*, 2008, **264**, 731–736.
- [20] Y. Berthier, M. Godet, and M. Brendle, *Tribol. Trans.*, 1989, **32**, 490–496.
- [21] E. Rabinowicz, *Friction and Wear of Materials*, John Wiley, New York, 1964.
- [22] J. M. Schneider, A. Voevodin, C. Rebholz, A. Matthews, J. H. C. Hogg, D. B. Lewis, and M. Ives, *Surf. Coat. Technol.*, 1995, **74–75**, 312–319.
- [23] S. W. Huang, M. W. Ng, M. Samandi, and M. Brandt, *Wear*, 2002, **252**, 566–579.
- [24] J. Robertson, *Mater Sci Eng, R*, 2002, **37**, 129–281.
- [25] J. Wagner, C. Mitterer, M. Penoy, C. Michotte, W Wallgram, and M. Kathrein, Conference Proceedings of PLANSEE SEMINAR, 2005, pp. 917–931.
- [26] K. Ushizawa, M. N-Gamo, Y. Kikuchi, I. Sakaguchi, Y. Sato, and T. Ando, *Phys. Rev. B*, 1999, **60**, R5165–R5168.
- [27] P. L. Dickrell, W. G. Sawyer, and A. Erdemir, *Journal of Tribology*, 2004, **126**, 615–619.
- [28] K. J. Wahl and I. L. Singer, *Tribol. Lett.*, 1995, **1**, 59–66.
- [29] K. J. Wahl, D. N. Dunn, and I. L. Singer, *Wear*, 1999, **230**, 175–183.

- [30] M. Hamilton, L. Alvarez, N. Mauntler, N. Argibay, R. Colbert, D. Burris, C. Muratore, A. Voevodin, S. Perry, and W. Sawyer, *Tribol. Lett.*, 2008, **32**, 91–98.
- [31] J. M. Cairney, P. R. Munroe, and M. Hoffman, *Surf. Coat. Technol.*, 2005, **198**, 165–168.
- [32] J. Hu, R. Wheeler, J. Zabinski, P. Shade, A. Shiveley, and A. Voevodin, *Tribol. Lett.*, 2008, **32**, 49–57.